UNIVERSIDADE FEDERAL DO ESPÍRITO SANTO

CENTRO TECNOLÓGICO

PROGRAMA DE PÓS-GRADUAÇÃO EM ENGENHARIA MECÂNICA

RAMON SILVA MARTINS

NUMERICAL SIMULATIONS OF INSTALLATION EFFECTS CAUSED BY UPSTREAM ELBOWS ON SINGLE-PATH TRANSIT-TIME ULTRASONIC FLARE FLOW METERS

VITÓRIA

2012

RAMON SILVA MARTINS

NUMERICAL SIMULATIONS OF INSTALLATION EFFECTS CAUSED BY UPSTREAM ELBOWS ON SINGLE-PATH TRANSIT-TIME ULTRASONIC FLARE FLOW METERS

A dissertation submitted in partial fulfilment of the requirements for the degree of Master of Science in Mechanical Engineering.
Supervisor: Prof. Rogério Ramos, D.Sc.

VITÓRIA

2012

Folha reservada para Ficha Catalográfica

RAMON SILVA MARTINS

NUMERICAL SIMULATIONS OF INSTALLATION EFFECTS CAUSED BY UPSTREAM ELBOWS ON SINGLE-PATH TRANSIT-TIME ULTRASONIC FLARE FLOW METERS

A dissertation submitted in partial fulfilment of the requirements for the degree of Master of Science in Mechanical Engineering.

Approved on May 23, 2012.

EXAMINING COMMITTEE

Prof. Rogério Ramos, D.Sc. - Supervisor
Universidade Federal do Espírito Santo

Prof. Juliana Braga Rodrigues Loureiro, D.Sc.
Universidade Federal do Rio de Janeiro

Prof. Neyal Costa Reis Junior, Ph.D.
Universidade Federal do Espírito Santo

Prof. Márcio Ferreira Martins, Ph.D.
Universidade Federal do Espírito Santo

VITÓRIA

2012

To my parents, Lucila and Wildo,
and to my fiancée, Maíra.

Acknowledgements

I fill extremely grateful to my partner, Anselmo Soeiro Pereira. I owe him a lot for my achievements over the last five years. I do believe in all the work we do together and I thank him (my *parça*, my brother and dear friend) for all opportunities of growing beside him.

I thank God for providing us the opportunities for constant learning and improvement.

I express my gratitude for my parents, who have always encouraged my studies. I am eternally grateful for the education, the good examples, and everything else I could breathe around them since I was born. Today, a bit more mature, I can realize how important was all they have done for me. I considered myself a winner and I am glad they feel happy and proud about me. I know they did their best. I love you!

I am immensely thankful for my fiancée, specially for her patience and maturity necessary to understand the professional moment we live. It is time to build the foundations so that we can have a more serene life in the future. I know it has not been easy years, even so she has been great and all her family as well. We are about to live a challenging experience and, now, I am sure we will do everything for being together. Thank you *pequena* for all your love, comprehension, encouragement and support, and for giving up many things for us. You are amazing! Love you!

I feel in debit of attention to my family, but they love and support me anyway. Therefore, I wish to thank them all for understanding my absence over those last years and for hoping that I succeed.

I am grateful to my supervisor, Rogério Ramos, for the confidence above all. The opportunity to be part of his research group has changed my path inside the University. His zeal for the

laboratory and his unique humour have made this journey being profitable. Thank you for your supervision, for sharing many knowledges, and for being patient with my limitations, bringing me forward.

Several professors have contributed to my education. Hence, I wish to thank all the great professors I had. Moreover, I highlight my appreciation to the following professors: Edson Soares, who largely contributed to my formation with philosophical debates and his scientific spirit, and Márcio Martins for all his gentle actions and words, helping me so much with wonderful advices and tips, and specially for becoming a friend (as well as his wife, Fabienne) with whom I could enjoy many pleasant moments.

I am grateful to my co-workers at LFTC with whom I have spent great times. Special thanks to Marco Aurélio Zanoni, Cecília Mageski, Fabrício Sisquini and Bruno Furtado.

I thank Ufes and PPGEM for all their teaching and administrative staff.

I express my acknowledgements to ANP and its human resources program at Ufes (PRH-29) whose financial support and grant have enabled this project.

I kindly thank every employee of Escola São Domingos, where I went to elementary and high school. There, I could learn beyond the books and become a better citizen and a thinking student as well.

Fortunately, I have several friends and I am proud of all of them. People from *Banda Sabará* and from school are special to me, and I feel compelled to thank them for being always there whenever I needed, for understanding my absence and my objectives. I want them to know that it is always a pleasure to have them around. I am sure they will recognize themselves. I appreciate all your feelings for me!

Finally, I express my gratitude to any person who have (sometimes even unintentionally) contributed to my career or to my learnings in the long way of life and evolution.

Abstract

Numerical simulations of installation effects caused by upstream elbows on single-path transit-time ultrasonic flare flow meters

Oil and gas industry requires accurate flow measurements since they are stated by law. Nevertheless, curves and other obstacles are commonly found in such industry field, which may affect the quality of flow measurement due to flow disturbances, such as swirl and velocity profile asymmetries. Single-path ultrasonic flow meters are often used in flare gas installations, despite being sensitive to such disturbances. The present work use commercial CFD codes to obtain disturbed flow fields downstream from single and double elbow pipe installations, aiming to investigate both magnitude and behaviour of such effects on ultrasonic flow measurement. Numerical integration is applied for several acoustic path arrangements, simulating single-path ultrasonic flow meters in different situations in order to evaluate its correction factor deviation under disturbed conditions. Reynolds numbers from 1×10^4 to 2×10^6 are considered. Transducers mounting angles from 0° to 180° are tested and axial positions up to 80D downstream from the curve are evaluated. Results indicate that single-path ultrasonic flow meters are sensitive to installation effects. Correction factor deviations usually showed to be significantly higher than 2% for axial positions shorter than 20D, as recommended by several manufacturers or regulations. Nevertheless, deviations may reach 0.01% in some specific configurations, which suggests that ultrasonic flow measurement might be improved by rearranging flow meter device in favourable angular position and mainly by implementation of specific functions for correction factors under disturbed conditions.

Keywords: ultrasonic flow meter, installation effects, correction factor, computational fluid dynamics.

Resumo

Simulações numéricas de efeitos de acidentes de linha causados por curvas à montante de medidores de vazão por ultrassom de um canal por tempo de trânsito para gás de *flare*

A indústria de petróleo e gás requer medições de vazão de baixa incerteza, uma vez que são estabelecidas por lei. Contudo, curvas e outros obstáculos são comumente encontrados nesse cenário e podem afetar a qualidade da medição de vazão em função de perturbações no escoamento, tais como *swirl* e assimetrias no perfil de velocidades. Medidores de vazão por ultrassom de um canal são frequentemente utilizados em instalações de gás de queimadores, apesar de serem sensíveis a tais perturbações. O presente trabalho usa códigos comerciais de CFD para obter o escoamento à jusante de instalações com uma curva e duas curvas, visando a investigar a magnitude e o comportamento de tais efeitos na medição de vazão. Integração numérica é utilizada para diversos arranjos de caminho acústico, simulando medidores de vazão por ultrassom de um canal em várias condições para avaliar o desvio do fator de correção em escoamentos perturbados. Números de Reynolds de 1×10^4 a 2×10^6 são considerados. Ângulos de montagem dos transdutores de 0° a 180° são testados e posições axiais até 80D à jusante do obstáculo são avaliadas. Os resultados indicam que medidores de vazão por ultrassom são sensíveis aos efeitos de acidente de linha. O desvio do fator de correção mostra-se, em geral, consideravelmente maior que 2% em distâncias menores que 20D, conforme recomendado por alguns fabricantes e por leis. Não obstante, tais desvios podem atingir 0,01% em algumas configurações específicas, o que sugere que a medição de vazão por ultrassom pode ser melhorada pelo rearranjo do aparato em posição angular favorável e, principalmente, pela implementação de funções específicas para fatores de correção em condições perturbadas.

Palavras-chave: medidor de vazão por ultrassom, efeitos de acidentes de linha, fator de correção, dinâmica dos fluidos computacional.

Résumé

Simulations numériques des effets d'installation causés par des courbes en amont des débitmètres à ultrasons par temps de transit avec un chemin pour le gaz de torche

L'industrie pétrolière et gazière requiert des mesures de dèbit précises puisqu'elles sont évalués par des lois. Toutefois, de courbes et d'autres obstacles sont généralement trouvés dans tels domaine de l'industrie, pouvant affecter la qualité de la mesure de débit en raison de perturbations de l'écoulement comme les tourbillons (*swirl*) et les asymétries de profil de vitesse. Les débitmètres à ultrasons avec un chemin sont souvent utilisés dans les installations de gaz de torche (*flare*), bien qu'ils soient sensible à ces perturbations. Ce travail utilise la CFD pour obtenir des champs de vitesses perturbés en aval d'un courbe et de deux courbes, visant à étudier l'écart et le comportement de ces effets sur la mesure de débit à ultrasons. L'intégration numérique est appliqué pour plusieurs arrangements du chemin acoustique, simulant des débitmètres à ultrasons avec un chemin en différentes conditions. Nombres de Reynolds de 1×10^4 à 2×10^6 sont considérés. Angles de montage des transducteurs de 0° à 180° sont testés et différentes positions axiales jusqu'à 80D en aval de la courbe sont évaluées. Les résultats indiquent que les débitmètres à ultrasons avec un chemin sont sensibles aux effets d'installation. L'écart du facteur de correction généralement montre être significativement plus élevé que 2% pour les positions axiales plus courtes que 20D, tel que recommandé par plusieurs fabricants et règlements. Cependant, les écarts peuvent atteindre 0,01% dans certaines configurations spécifiques, ce qui suggère que la mesure de débit à ultrasons pourrait être améliorée en réorganisant le dispositif de débitmètre en position angulaire favorable et surtout par la mise en œuvre des fonctions spécifiques pour les facteurs de correction en conditions perturbées.

Mots-clés: débitmètre à ultrasons, effets d'installation, facteur de correction, méchanique des fluides numérique.

List of Figures

List of Tables

List of Symbols

A cross-sectional area, $[m^2]$; *or* coefficient matrix, [-]

A_{outlet} cross-sectional area at outlet plane, $[m^2]$

$\vec{A}$ vector area, $[m^2]$

a_{nb} coefficient for the neighbouring control volumes nearby P, [-]

a_P coefficient for the control volume around node P, [-]

b right-hand side vector, [-]

c velocity of the sound, $[m/s]$

C_1 constant of the standard k–ε model, dimensionless $\rightarrow 1.44$

C_2 constant of the standard k–ε model, dimensionless $\rightarrow 1.92$

C_{1RNG} constant of the k–ε RNG model, dimensionless $\rightarrow 1.42$

C_{2RNG} constant of the k–ε RNG model, dimensionless $\rightarrow 1.68$

C_{1RNG}^* function of the k–ε RNG model, dimensionless $\rightarrow C_{1RNG} - f_\eta$

C_μ constant of the standard$k$–ε model, dimensionless $\rightarrow 0.09$

$C_{\mu RNG}$ constant of the k–ε RNG model, dimensionless $\rightarrow 0.085$ (CFX) and 0.0845 (FLUENT)

D pipe internal diameter, $[m]$

e	east face relative to a general node P, dimensionless
E	east node relative to a general node P, dimensionless; *or* empirical constant of log-law, dimensionless $\rightarrow$ 9.793
$\hat{e}_i, \hat{e}_j$	unit vector in directions i and j (Einstein notation), [-]
F	general vector, [-]
f_η	function of the k–ε RNG model, dimensionless
I	turbulence intensity, dimensionless
k	ultrasonic flow meter correction factor, [m]; *or* turbulent kinetic energy, [m^2/s^2]
k_{dist}	turbulent kinetic energy at domain inlet plain, [m^2/s^2]
k_{inlet}	correction factor under disturbed condition, dimensionless
k_{num}	numerical correction factor, dimensionless
k_{ref}	reference correction factor, dimensionless
k_{spec}	specified boundary turbulent kinetic energy, [m^2/s^2]
k_P	kinetic energy at a near-wall mesh node P, [m^2/s^2]
k_t	instantaneous kinetic energy, [m^2/s^2]
$\bar{k}$	mean kinetic energy, [m^2/s^2]
Δk	correction factor error, dimensionless
I	turbulence intensity, dimensionless
L	distance between the transducers, [m]
L_{AP}	acoustic path length, [m]
$\vec{L}$	vector distance, [m]

ΔL distance between two numerical integration points, $[m]$

ΔL_{AP} space step for numerical integration, $[m] \rightarrow L_{APp} - L_{APp-1}$

$\dot{m}$ mass flow rate, $[kg/s]$

n exponent for Nikuradse turbulent fully developed velocity profile, dimensionless; *or* general normal direction, $[m]$

N number of integration points, dimensionless

$\mathbf{n}$ general normal vector, [-]

p pressure, $[N/m^2]$; *or* subscript for numerical integration point, dimensionless

P general node, dimensionless

$\mathcal{P}_k$ productions of turbulent kinetic energy, $[m^2/s^3]$

$\bar{p}$ time-averaged pressure, $[N/m^2]$

$\bar{p}_{np,outlet}$ time-averaged pressure at each nodal point (np) at outlet plane, $[N/m^2]$

$\bar{p}_{spec}$ specified boundary time-averaged pressure, $[N/m^2]$

$\bar{p}'$ time-averaged turbulent pressure fluctuation, $[N/m^2]$

p' turbulent pressure fluctuation, $[N/m^2]$

Q volumetric mean flow rate, $[m^3/s]$

Q^* volumetric instantaneous flow rate, $[m^3/s]$

R pipe radius, $[m]$

$\mathcal{R}$ function of the k–ε RNG model, $[kg/m\,s^4]$

r_ϕ raw residual value for ϕ, [-]

r_ϕ^n residual value for ϕ in the n-th iteration, [-]

r^* radial position from pipe center, $[m]$

$\tilde{r}_\phi$ normalized residual for ϕ, dimensionless

Re Reynolds number, dimensionless

$\Delta\vec{r}$ vector representing the distance between an upstream node and a nodal point, $[m]$

S_{ij} Strain rate tensor, $[1/s]$

$\bar{S}_{ij}$ Mean strain rate tensor, $[1/s]$

$\bar{S}$ Modulus of the mean strain rate tensor, $[1/s]$

$\bar{S}'_{ij}$ Time-averaged turbulent strain rate tensor, $[1/s]$

S_ϕ source term for a general property ϕ, [-]

$\bar{S}_\phi$ average value of source for a control volume, [-]

t, t^* time, $[s]$

t_{AB}, t_{BA} times of transit downstream and upstream, $[m/s]$

t_o initial time, $[s]$

u, v, w velocity components, $[m/s]$

u_i, u_j velocities in directions i and j (Einstein notation), $[m/s]$

u_m instantaneous mean flow velocity, $[m/s]$

u^* dimensionless velocity, dimensionless

$\bar{u}_{max}$ maximum time-averaged turbulent velocity over a cross-section, $[m/s]$

$\bar{u}_i, \bar{u}_j, \bar{u}_k$ time-averaged turbulent velocities in directions i, j and k (Einstein notation), $[m/s]$

$\bar{u}_m$ turbulent mean flow velocity, $[m/s]$

$\bar{u}_P$ turbulent mean velocity at a near-wall mesh node P, $[m/s]$

$\bar{u}'_i$ time-averaged turbulent velocity fluctuation in direction i (Einstein notation), $[m/s]$

u', v', w' turbulent velocity fluctuation components, $[m/s]$

u'_i, u'_j turbulent velocity fluctuations in directions i and j (Einstein notation), $[m/s]$

u'_{RMS} RMS turbulent velocity fluctuations, $[m/s]$

$\vec{u}, \mathbf{u}$ velocity vector, $[m/s]$

V volume, $[m^3]$

$\bar{V}_{AP}$ mean flow velocity, along the acoustic path, in the direction of the acoustic path, $[m/s]$

$\bar{V}_{APnum}$ numerical mean flow velocity, along the acoustic path, in the direction of the acoustic path, $[m/s]$

$\bar{V}_{UFM}$ mean flow velocity, along the acoustic path, in the direction of the flow, $[m/s]$

$\bar{V}_{UFMnum}$ numerical mean flow velocity, along the acoustic path, in the direction of the flow, $[m/s]$

ΔV volume of the control volume, $[m^3]$

w west node relative to a general node P, dimensionless

W west node relative to a general node P, dimensionless

x, y, z Cartesian coordinates, $[m]$

x_i, x_j, x_k Cartesian coordinates in directions i, j and k (Einstein notation), $[m]$

δx distances over a control volume (depending on the subscript), $[m]$

Δx control volume width, $[m]$

y_P distance between the near-wall mesh point P and the wall, $[m]$

y^*	dimensionless distance from the wall, dimensionless
y^*_{limit}	limiter, dimensionless $\rightarrow$ 11.06 (CFX) and 11 (FLUENT)
$\tilde{y}^*$	modified dimensionless distance from the wall, dimensionless $\rightarrow$ $\max(y^*, y^*_{limit})$

Greek letters

α	transducers inclination relative to pipe main axis, [°]; *or* under-relaxation factor, dimensionless
α_k	constant of the k–ε RNG model, dimensionless $\rightarrow$ 1.39
α_ε	constant of the k–ε RNG model, dimensionless $\rightarrow$ 1.39
β	blend factor, dimensionless; *or* constant of the k–ε RNG model, dimensionless $\rightarrow$ 0.012
Γ	general diffusion coefficient, [-]
δ_{ij}	Kronecker delta operator, dimensionless
ε	turbulence energy dissipation rate, $[m^2/s^3]$
ε_P	turbulence energy dissipation rate at a near-wall mesh point P, $[m^2/s^3]$
ε_{spec}	specified boundary turbulence energy dissipation rate, $[m^2/s^3]$
θ	transducers mounting angle relative to the vertical axis, [°]
κ	Von-Kármán constant for log-law, dimensionless $\rightarrow$ 0.4178
η	ratio of the turbulence to mean strain time scale, dimensionless
η_0	constant of the k–ε RNG model, dimensionless $\rightarrow$ 4.38
μ	dynamic viscosity, $[Pa\,s]$
μ_{eff}	effective viscosity, $[Pa\,s] \rightarrow \mu + \mu_T$

$\tilde{\mu}$ viscosity ratio, dimensionless $\rightarrow \mu_T/\mu$

μ_T eddy viscosity, $[Pa\,s]$

ν kinematic viscosity, $[St]$

ρ density, $[kg/m^3]$

σ_k constant of the standard k–ε model, dimensionless $\rightarrow 1.0$

σ_ε constant of the standard k–ε model, dimensionless $\rightarrow 1.3$

σ_{kRNG} constant of the standard k–ε RNG model, dimensionless $\rightarrow 0.7179$

$\sigma_{\varepsilon RNG}$ constant of the standard k–ε RNG model, dimensionless $\rightarrow 0.7179$

τ_{ij} Shear stress tensor, $[N/m^2]$

τ_w Wall shear stress, $[N/m^2]$

τ_{Tij} Reynolds stress tensor, $[N/m^2]$

ϕ general property, [-]

ϕ_f value of ϕ at a general face f, [-]

ϕ_{nb} value of ϕ at the neighbouring nodes nearby P, [-]

ϕ_{up} value of ϕ at the upstream node of a general node P, [-]

ϕ^n value of ϕ in the n-th iteration, [-]

ϕ^* old value (previous iteration) of ϕ, [-]

$\Delta\phi$ change in ϕ, [-]

List of Acronyms

ABNT	Associação Brasileira de Normas Técnicas
AGA	American Gas Association
ANP	Agência Nacional de Petróleo, Gás Natural e Biocombustíveis
CFD	Computational Fluid Dynamics
CG	Conjugate Gradient
DNS	Direct Numerical Simulation
ILU	Incomplete Lower Upper
INMETRO	Instituto Nacional de Metrologia, Qualidade e Tecnologia
LabMaqFlu	Laboratório de Máquinas de Fluxo
LDA	Laser-Doppler Anemometer (or Anemometry)
LDV	Laser-Doppler Velocimeter (or Velocimetry)
LES	Large-Eddy Simulation
LFTC	Laboratório de Fenômenos de Transporte Computacional
LU	Lower Upper
MUSCL	Monotone Upstream-Centered Schemes for Conservation Laws

PC   Personal Computer

PISO   Pressure Implicit with Splitting of Operators

PPGEM   Programa de Pós-Graduação em Engenharia Mecânica

PRH   Programa de Recursos Humanos

QUICK   Quadratic Upwind Interpolation for Convective Kinetics

RANS   Reynolds Averaged Navier-Stokes

RMS   Root Mean Square

RSM   Reynolds Stress Model

RNG   Renormalization Group

SIMPLE   Semi-Implicit Method for Pressure Linked Equations

SIMPLEC   SIMPLE-Consistent

TDV   Total Variation Diminishing

Ufes   Universidade Federal do Espírito Santo

URANS   Unsteady Reynolds Averaged Navier-Stokes

Contents

Part I

General Discussions

Chapter 1

Introduction

1.1 Motivation and Objectives

1.1.1 Motivation

Flow meters calibration represents an important issue to oil and gas industry, where accurate flow measurements are required and national regulations describe the proceedings for operational and custody metering.

In such context, flare gas installations are common in oil refineries and offshore platforms, for instance. The main goals of such systems are to act as safety devices to protect some equipments from unplanned over-pressuring and to eliminate the waste gas from production and separation processes. Typically, 90% of the gas is flared during 5% of the production time [5] which results in high flow measurement ranges.

Environmental laws creation and inspections (audits) become more frequent and are increasingly stringent, so that knowing the amount of flare gas in such processes becomes also remarkable. Flow measurements allow estimating gas emissions, such as methane and carbon dioxide. [6, 7, 8]

On the other hand, flare gases typically flow at low pressure (about 0.7 bar), presenting considerable impurity levels [5]. Such conditions usually reflect in low values associated to such

flows, which make the use of more sophisticated flow meters impracticable.

Due to being profitable, single path ultrasonic flow meters are widely used in such installations. Nevertheless, since such flow meters cannot map the velocity field properly, it is desirable that they operate under fully developed flow condition.

However, due to available space, obstacles such as valves and curves are close to the metering section in many cases. Such obstacles cause flow disturbances, which may compromise flow measurement quality.

1.1.2   Objectives

The present dissertation aims representing turbulent disturbed flows by means of commercially available CFD (Computational Fluid Dynamics) codes and evaluating the influence of upstream elbow configurations on the correction factor (factor k) of single-path ultrasonic flow meters. For this purpose, a numerical flow meter correction factor is considered as a function of hydrodynamic parameters calculated by the tested codes. The correction factor sensitivity to some meter installation effects is investigated aiming the possibility of proposing a modified correction factor to disturbed cases.

1.2   Plan of the Dissertation

This dissertation is divided in three parts. Part I contains this introductory chapter and two other chapters which provide information on flow measurement and ultrasonic flow meters (Chapter 2), and gather informations about installation effects, their causes and possible solutions (Chapter 3). All methodology is described in Part II. Chapter 4 contains mathematical and numerical approaches for modelling the flow field and the ultrasonic flow meter. Parameters considered for simulation and preliminary sensitivity studies are dealt in Chapter 5. In Chapter 6, a validation procedure is carried out by comparing simulations with experimental data from literature. Part III contains results and discussions for simulated correction factors (Chapter 7) and a closing chapter which gathers some commentaries on main contributions, difficulties faced throughout the work and proposals for future work (Chapter 8).

Chapter 2

Ultrasonic Flow Measurement

Ultrasonic flow meters have several applications, such as:

- measurement of gas through production facilities (such as flare gas installations [9]), transmission pipelines, storage facilities, and distribution and domestic [10] systems;

- measurement of liquids in nuclear power plants [11] and hydraulic power stations [12], and many other areas such as food, semiconductor and chemical industries [13];

- measurement of systolic and diastolic blood pressure as well as blood flow rate [14], in medicine;

Despite all these applications, ultrasonic flow meters are considered recent technology and the best procedures for using such technique are still in development as well as the technology itself

The first specific documents indicating appropriate procedures and minimum requirements on industrial ultrasonic flow measurements are from the end of the 20th century. The Report No. 9 first edition [15] by the American Gas Association (AGA) presents the former engineering good practices applied to natural gas measurement by ultrasonic flow meters.

In Brazil, the Portaria Conjunta ANP/INMETRO No. 1 [16] points out ultrasonic flow meters as a suitable technology for oil and gas metering, since they follow AGA 9 procedures. Recently, the ABNT (Brazilian Association for Technical Regulations - in Portuguese *Associação Brasileira de Normas Técnicas*) published the regulation for multipath ultrasonic flow measure-

ment of gas [17].

Notwithstanding, all these regulations recommend operation in fully developed flow condition, regardless of the fact that in practical situations such condition is rarely satisfied. In order to remark the necessity of having such condition as well as its consequences when not met, this chapter shows some important definitions about flow measurement and then presents the operating principle of ultrasonic flow meters.

2.1 Flow Measurement

"Among the most frequent measured variables, the flow rate is the one who requires the most diversified technologies to develop meters and transmitters."
Gérald J. Delmée [18] – author's translation from Portuguese

2.1.1 What is a Flow Rate?

It is believed that the need to measure flow appeared with the public water supply service [18, 19]. Currently, besides public services, flow measurement presents important industrial applications and is known as a control and monitoring tool.

Delmée [18] defines flow rate as the amount of fluid passing through a pipe cross-section per unit time. Such quantity is commonly expressed in terms of volume or mass, giving the following terminologies:

- *the mass flow rate*: for mass per unit time;

- *the volumetric flow rate*: for volume per unit time. In this case, especially when compressibility effects are relevant, it is usual to specify temperature and pressure conditions considered for presented measurements - operating or reference temperature and pressure.

Aiming better comprehension of the various flow measurement techniques, it is necessary to introduce some terms which may assist understanding the fundamentals of some flow meters.

- *Point or local velocity*

  The point velocity is the velocity at a specific point of the flow. Such measure might be performed by several instruments, such as hot wire anemometer, Pitot-tube and Laser-Doppler velocimeter (LDV) [19]. Since it is a local variable, the notation for the velocity at a point (x, y, z) and at a time t is: $\vec{u}(x, y, z, t)$.

- *Mean flow velocity*

  The mean flow velocity is the average of the point velocities over a cross-section area A of a pipe. At a time t, the instantaneous mean flow velocity (u_m) may be expressed by Eq. (2.1), as follows.

$$u_m(t) = \frac{1}{A} \int_A \vec{u}(x, y, z, t) \cdot \mathrm{d}\vec{A} \tag{2.1}$$

  Where

  - $\mathrm{d}\vec{A}$ is the vector associated with the infinitesimal element of the same cross-section area A.

- *Flow rate*

  The instantaneous volumetric flow rate (Q^*) is then given by Eq. (2.2).

$$Q^*(t) = u_m(t)A \tag{2.2}$$

  For the mass flow rate ($\dot{m}$) the fluid density (ρ) is required, yielding Eq. (2.3).

$$\dot{m}(t) = \rho u_m(t)A \tag{2.3}$$

  It is important to remark that, in Brazil, only *volumetric* flow measurements are authorized for oil and gas [16].

Statistical procedures (see section 4.1.1) are commonly carried out in turbulent flows in order to obtain time-averaged values of the flow. Then, it is also important to define the time averaged flow rate, which uses the turbulent mean flow velocity ($\bar{u}_m$), as given by Eq. (2.4).

$$Q = \bar{u}_m A \qquad (2.4)$$

Section 4.1.1 contains more information on the statistical treatment for turbulent properties.

It is remarkable the fact that the flow rate is proportional to the mean flow velocity for a constant cross-section area pipe. Ultrasonic flow meters measure the mean flow velocity along (and in the direction of) the acoustic path (see Sec. 2.3) and it is the need of converting such measurements that makes them sensitive to flow disturbances. Such conversion is made by a correction factor (factor k), which is the object of study in the present work.

2.2   Different Ultrasonic Flow Measurement Techniques

Ultrasonic technique is recent and still under development. Nevertheless, this technology have captured 10% of sales volume for *all* types of flow meters in 2005 [14]. Such expansion may be explained by several remarkable features, as commented in the items bellow.

1. *Reasonable accuracy/low uncertainty* – Despite their sensitivity to disturbed flows and pipe wall roughness, the uncertainty of ultrasonic flow meters is usually lower then 1% at typical industrial installations and may achieve 0,5% or less under special conditions, such as the possibility of CFD modelling [14, 18]. It is also known that multipath configurations (Subsec. 2.3.3) may reduce uncertainties and improve accuracy [1, 14, 18, 20, 21].

2. *Versatility* – Ultrasonic flow meters works well with both liquids and gases, even in corrosive or erosive environment [18]. Moreover, these meters are able to measure reverse flows, *i.e.*, flows in the opposite direction.

3. *High turndown ratio* – Modern ultrasonic flow meters can work in wide flow measure-

ment rangeability [22, 23]. Particularly, for flare gas applications, ultrasonic flow meters may achieve turndown ratios of up to 4000:1 [24, 25].

4. *Negligible intrusion installation* – Ultrasonic transducers may face or even exceed the pipe inner wall, nevertheless they generally introduce negligible pressure loss [5]. However, it is known that they affect the shape of the velocity profile [26].

5. *Non-moving parts* – Except for vibrating ceramic or piezoelectric crystals, ultrasonic flow meters have no moving partings [5, 20].

6. *Self-diagnosis* – Ultrasonic flow meters can indicate the occurrence of disturbances or relevant measurement errors. Self-diagnosis is made by modelling the normal behaviour of a flow meter and comparing on-line observed and modelled data [19, 27].

7. *Relative low installation and maintenance cost* – The items above (specially items 4, 5, and 6) usually provide low installation and maintenance costs [5, 19].

8. *Capability to determine fluid parameters* – Due to their measurement principle, ultrasonic flow meters may infer other parameters such as temperature, density and flare gas average molecular weight [14].

Lynnworth and Liu [14] present four ultrasonic flow measurement techniques existing in 2005: Doppler or reflection, transit-time (also called contrapropagation [5], counterpropagation [20] or time-of-flight [5, 20]), correlation and passive methods. The authors also present the existence of hybrid techniques which contain two or three methods to deal with different fluids, flow regimes and pipe wall thickness.

Transit-time accounts for more than half the sales volume of all ultrasonic flow meter types in 2005 and is prevalent in industrial installations [14, 19]. Hence, they are focused in this dissertation.

2.3 Transit-Time Ultrasonic Flow Measurement

According to Mylvaganam [5], Rütten's patent of 1928 is known as the first application of ultrasonics in transit-time flow measurement. However, it was still necessary some decades to

develop such technology. In the 1980s, with the advances on high-speed electronics, it resurged and ultrasonic flow meters began to be applied in industry.

2.3.1 Operating Principle

Transit-time ultrasonic flow meters have at least one pair of ultrasonic transducers which transmit and receive ultrasonic pulses through the fluid, composing an acoustic channel, the so called *acoustic path*. The pulses are, in fact, typical mechanical waves which travel through a medium. Such waves are generated by the vibration of piezoelectric or ceramic crystals which are excited by electrical current. Thus, crystals vibrate in the same frequency of excitation. In flow measurement applications, frequencies are typically hundreds of kHz for gases and at or above 1 MHz for liquids [14, 18]. Just for the sake of comparison, human ear is capable to detect wave frequencies from 10 to 10,000 Hz. Such waves are named *sound*.

In fact, transit-time ultrasonic flow meters measure the travel-times of downstream and upstream pulses between the transducers. They are "based on the fact that the speed of an acoustic pressure wave increases in the direction of the flow and decreases when directed against the flow" [20]. The difference between downstream and upstream transit-times allows inferring the mean flow velocity.

Figure 2.1 displays an schematic drawing of a typical single-path transit-time ultrasonic flow meter device. One may notice that pipe axis coincides with x-axis and D is the pipe internal diameter. Upstream and downstream transducers are identified by letters A and B, respectively. The transducers mounting angle θ is defined by the rotation angle in the x-axis from the vertical position (y-axis). The mounting angle defines the emission plane, which contains the main direction of acoustic pulses emitted by the pair of transducers. Moreover, the emission plane also contains the angle α, which represents the transducers inclination relative to the pipe axis, and the length L, representing the distance between the transducers in symmetrically opposite faces.

Regarding the angles in Fig. 2.1, α is generally 45° and Ramos [28] shows that such choice provides the lowest uncertainties for the flow rate. The mounting angle (θ) plays an important role in ultrasonic flow measurements under disturbed condition and is commented in Chapter 3.
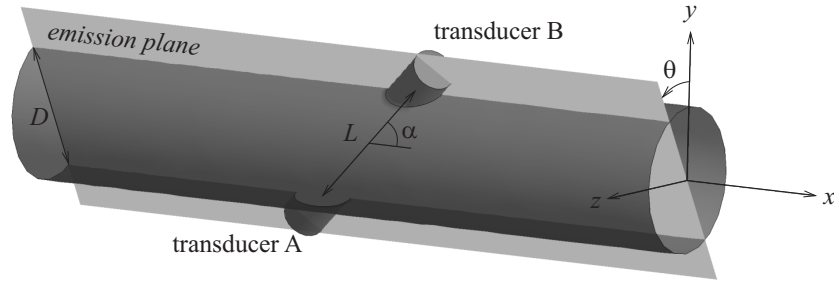
Figure 2.1. Ultrasonic flow meter basic scheme.

In the absence of flow, the sound pulses travel in the sound propagation velocity in the fluid (c). Furthermore, both upstream and downstream pulses travel over the same path, represented by a line in Fig. 2.2. Such trajectory is the acoustic path and its length (L_{AP}) coincides with L in the absence of flow. Therefore, upstream and downstream transit times (t_{AB} and t_{BA}, respectively) have the same value, as shown in Eq. (2.5).

$$t_{AB} = t_{BA} = \frac{L_{AP}}{c} \tag{2.5}$$
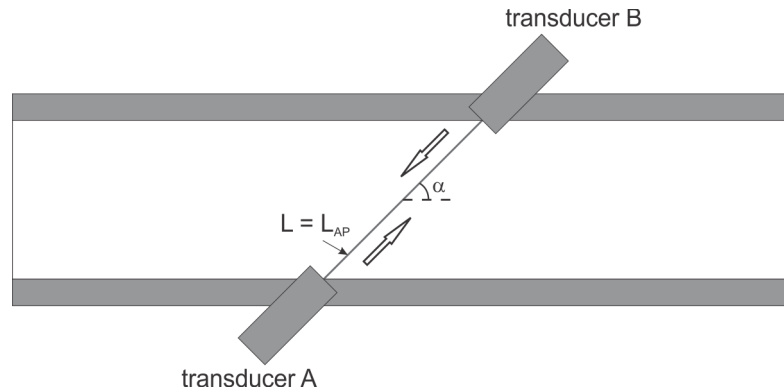
Figure 2.2. Cross view on emission plane in the absence of flow.

In the presence of flow, the acoustic signal velocity is influenced by the flow velocity projected onto the acoustic path. Upstream signal is accelerated whereas downstream signal is decelerated by the flow, yielding different transit times, as shown in Eqs. (2.6) and (2.7).

$$t_{AB} = \frac{L_{AP}}{c + \bar{V}_{AP}} \tag{2.6}$$

$$t_{BA} = \frac{L_{AP}}{c - \bar{V}_{AP}} \tag{2.7}$$

The portion $\bar{V}_{AP}$ represents the influence of the flow velocity field in the acoustic signal velocity.

It is now necessary to briefly introduce an important assumption about the length of the acoustic path (L_{AP}). It is known [29, 30] that the velocity gradient refracts sound beams so that the acoustic path is not a straight line and depends on velocity profile shape. Such behaviour is similar to the light refraction phenomenon in a change of medium. Thus, the velocity profile may affect the shape of the acoustic path, as represented in Fig. 2.3. However, the simplest approach is to consider the acoustic path as a straight line whose length is the distance between the transducers, yielding $L_{AP} = L$. Such assumption has shown to be adequate for Mach numbers smaller than 0.1 [29]. Signal deviation is better commented in Chapter 3.
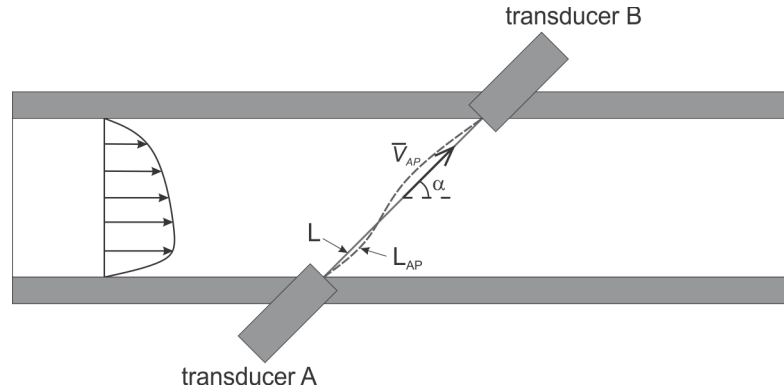
Figure 2.3. Cross view on emission plane in the presence of flow: acoustic path deviation.

Using the previous assumption ($L_{AP} = L$), it is easy to show the following geometric relation.

$$D = L_{AP} \sin \alpha \tag{2.8}$$

Mathematically, the unknowns c and $\bar{V}_{AP}$ can be found by solving the algebraic system represented by Eqs. (2.6) and (2.7), yielding Eqs. (2.9) and (2.10).

$$c = \frac{D}{2 \sin \alpha} \left(\frac{t_{AB} + t_{BA}}{t_{AB} t_{BA}} \right) \tag{2.9}$$

$$\bar{V}_{AP} = \frac{D}{2\sin\alpha}\left(\frac{t_{AB} - t_{BA}}{t_{AB}t_{BA}}\right) \tag{2.10}$$

Due to their measurement principle, transit-time ultrasonic flow meters calculate c and $\bar{V}_{AP}$. The sound propagation velocity c is a well known thermodynamic property for several fluids. On the other hand, $\bar{V}_{AP}$ is an intrinsic measurement of ultrasonic flow meters and deserves attention. At this point, it is important to formally present a general definition for $\bar{V}_{AP}$, given by Eq. (2.11).

$$\bar{V}_{AP} = \frac{1}{L_{AP}}\int_{L_{AP}} \vec{u}(x, y, z) \cdot \mathrm{d}\vec{L} \tag{2.11}$$

By regarding Eq. (2.11), one may conclude that $\bar{V}_{AP}$ is the mean value, along the acoustic path, of flow velocity projected on the acoustic path. However, a mean velocity in the main direction of the flow (perpendicular to the cross-section) is necessary to obtain the flow rate. In this sense, the variable $\bar{V}_{UFM}$, which is the velocity considered by ultrasonic flow meters, is now introduced for representing the mean flow velocity over the acoustic path in the direction of the flow. The relation between $\bar{V}_{UFM}$ and $\bar{V}_{AP}$ is given by Eq. (2.12), and Fig. 2.4 illustrates such velocities.

$$\bar{V}_{UFM} = \frac{\bar{V}_{AP}}{\cos\alpha} \tag{2.12}$$
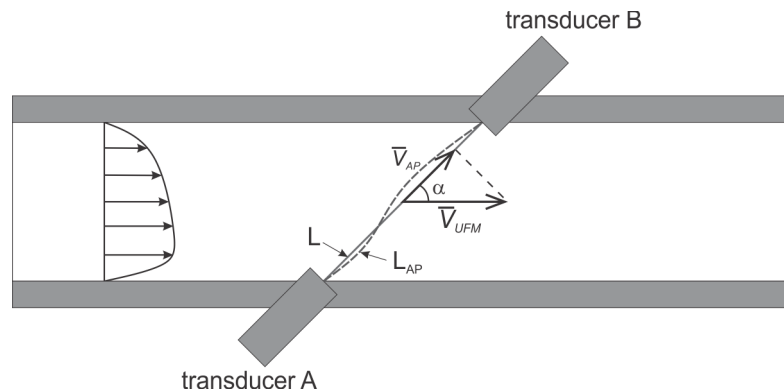
Figure 2.4. Cross view on emission plane in the presence of flow: main velocities.

Equations (2.11) and (2.12) may be considered as general formulation because firstly they calculate the mean magnitude of velocities projected on the acoustic path ($\bar{V}_{AP}$). Then, they calculate

the velocity in the main flow direction ($\bar{V}_{UFM}$) whose projection in the direction of the acoustic path is the one calculated before ($\bar{V}_{AP}$). Thus, the contribution of tangential velocity components ($\bar{v}$ and $\bar{w}$), which is the goal of the present work, may also be taken into account. This general formulation is presented because it also recovers the simplest case suggested by AGA 9 [31] and by the Brazilian regulation [17], as shown in the next subsection.

One may notice that the velocity considered by single-path ultrasonic flow meters is actually a mean velocity. It is like if ultrasonic flow meters could only detect flat (uniform) profiles whose mean value equals $\bar{V}_{UFM}$, resulting in a contribution $\bar{V}_{AP}$ in the direction of the acoustic path. Nevertheless, as shown in Eq. (2.4), the turbulent mean flow velocity over a pipe cross-section ($\bar{u}_m$) is needed to obtain the flow rate (Q) for turbulent flows. Thus, it is necessary to relate $\bar{V}_{UFM}$ and $\bar{u}_m$. This is a relation between two different means of the same variable: $\bar{V}_{UFM}$ represents the average of the flow field over the acoustic path whereas $\bar{u}_m$ represents the average of the flow field over the pipe cross-section. Therefore, ultrasonic flow meters use a factor k to relate $\bar{u}_m$ and $\bar{V}_{UFM}$, as shown in Eq. (2.13).

$$k = \frac{\bar{u}_m}{\bar{V}_{UFM}} \tag{2.13}$$

The factor k, also called correction factor, k-factor, profile factor [32], hydrodynamic factor [1] or hydraulic correction factor [33], as presented in Eq. (2.13), is defined in AGA 9 [31] and is also used in the Brazilian regulation [17]. The factor k is better discussed in the next subsection.

Since pipe cross-sectional area A may be expressed as $\pi D^2/4$, the equation for the volumetric flow rate (Q) is finally obtained by substituting Eqs. (2.10), (2.12) and (2.13) into Eq. (2.4), yielding:

$$Q = k \frac{\pi D^3}{4 \sin 2\alpha} \left(\frac{t_{AB} - t_{BA}}{t_{AB} t_{BA}} \right) \tag{2.14}$$

However, a quick analysis gives Q and k as unknowns. Since the goal is to obtain the flow rate (Q), k requires some special treatment.

2.3.2 The Factor k Issue

Precise knowledge of the factor k is necessary to obtain accurate flow measurements. Before any mathematical definition, it is necessary to make some brief comments on the difference between two distinct concepts for the factor k. The literature about ultrasonic flow meters contains both scientific and technical works, and it is necessary to distinguish formal and practical definitions aiming to avoid misunderstandings.

From the scientific point of view, *i.e.* formally, the factor k is merely a geometrical correction factor which relates mean values taken from distinct samples of a sample space. Regarding the ultrasonic flow measurement, the factor k relates the mean flow velocity over the cross-sectional area and the mean flow velocity over the acoustic path.

On the other hand, technically the factor k plays the role of a hydrodynamic correction factor, which allows obtaining the mean flow velocity from the velocity detected by the ultrasonic flow meter. Such interpretation may lead to possible corrections aiming lower uncertainties and errors associated to disturbed flow measurement.

Next, one may present a general definition for the correction factor using Eqs. (2.11), (2.12) and (2.13), yielding Eq. (2.15).

$$k = \frac{\bar{u}_m}{\overline{V}_{UFM}} = \frac{\dfrac{1}{A} \displaystyle\int_A \vec{\bar{u}}(x,y,z) \cdot \, \mathrm{d}\vec{A}}{\dfrac{1}{\cos\alpha} \dfrac{1}{L_{AP}} \displaystyle\int_{L_{AP}} \vec{\bar{u}}(x,y,z) \cdot \, \mathrm{d}\vec{L}} \tag{2.15}$$

Since the velocity field is project on the direction of unitary area vector, velocity components $\bar{v}$ and $\bar{w}$ do not cause any influence on the dividend in Eq. (2.15). On the other hand, since the flow field in the divisor is projected on the acoustic path, such value may be influenced by all velocity components, depending on the angles defining the acoustic path, *i.e.* α and θ. Using the coordinate system and angles shown in Fig. 2.1, the mean of any three dimensional velocity field projected on the acoustic path may be represented as a function of its turbulent mean components $\bar{u}$, $\bar{v}$ and $\bar{w}$, as shown in Eq. (2.16).

$$\bar{V}_{AP} = \frac{1}{L_{AP}} \left(\cos\alpha \int\limits_{L_{AP}} \bar{u}\,\mathrm{d}L + \sin\alpha\cos\theta \int\limits_{L_{AP}} \bar{v}\,\mathrm{d}L + \sin\alpha\sin\theta \int\limits_{L_{AP}} \bar{w}\,\mathrm{d}L \right) \quad (2.16)$$

It is remarkable that integral terms represent mean velocity values over the acoustic path whereas sine and cosine operations are responsible for projecting such velocities on the acoustic path.

As commented above, this general formulation is only carried out aiming to take into account the contribution of $\bar{v}$ and $\bar{w}$ for the calculation of the correction factor. Such approach is better conducted in Sec. 4.4. For now, if the contributions of $\bar{v}$ and $\bar{w}$ are not considered, Eq. (2.15) takes the form of Eq. (2.17), as suggested by AGA 9 [31] and by the Brazilian regulation [17].

$$k = \frac{\dfrac{1}{A} \displaystyle\int\limits_{A} \bar{u}\,\mathrm{d}A}{\dfrac{1}{L_{AP}} \displaystyle\int\limits_{L_{AP}} \bar{u}\,\mathrm{d}L} \quad (2.17)$$

One may notice that the velocity field is required to proceed the calculation for both dividend and divisor in Eq. (2.15). For $\bar{u}_m$ the velocity ($\bar{u}$) is integrated over the cross-section whereas for $\bar{V}_{UFM}$ it is integrated over the acoustic path. Since the velocity field is unknown, the proposition in AGA 9 [31] is to assume fully developed flow profile. With this assumption, one may already guarantee only axial and constant velocities. But what is the function that could best represent the shape of turbulent fully developed velocity profiles?

AGA 9 [31] suggests the semi-empirical profile proposed by Nikuradse [34], which is a power-law based on his smooth pipe experimental investigation, as follows.

$$\bar{u}(r^*) = \bar{u}_{max} \left[1 - \left(\frac{r^*}{R} \right) \right]^{\frac{1}{n}} \quad (2.18)$$

Where

- $\bar{u}_{max}$ is the maximum velocity (pipe center velocity) $[m/s]$;

- r^* is the radial distance from pipe center $[m]$;

- R is the pipe radius [m];

- n is the exponent of the power law [-];

It is important to remark that Nikuradse [34] profile is still widely used and the Brazilian regulation [17] considers it as well.

Since the flow field is assumed to be fully developed and the divisor in Eq. (2.17) is an integral over a line, any line may be possible, including the integral over the diameter. Hence, it is possible to calculate the factor k based on Nikuradse profile, as summarized in Equation (2.19).

$$k = \frac{\dfrac{1}{A} \displaystyle\int_A \bar{u}_{max} \left[1 - \left(\dfrac{r^*}{R}\right)\right]^{\frac{1}{n}} \mathrm{d}A}{\dfrac{1}{D} \displaystyle\int_D \bar{u}_{max} \left[1 - \left(\dfrac{r^*}{R}\right)\right]^{\frac{1}{n}} \mathrm{d}r} = \frac{\bar{u}_{max} \dfrac{2n^2}{(n+1)(2n+1)}}{\bar{u}_{max} \dfrac{n}{(n+1)}} = \frac{2n}{2n+1} \qquad (2.19)$$

The exponent n is a function of the Reynolds number (Re) and pipe roughness (or the coefficient of friction) [31]. Analysing the plots of the coefficient of friction against the Reynolds number, Prandtl proposed the so called *universal law of friction for smooth pipes* [35], as follows.

$$n = 2.0 \log\left(\frac{Re}{n}\right) - 0.8 \qquad (2.20)$$

Substituting the relations contained in Eq. (2.19) into Eq. (2.14), one may find the direct relation between Q and n, as follows.

$$Q = \frac{\pi D^3}{4 \sin 2\alpha} \left(\frac{t_{AB} - t_{BA}}{t_{AB} t_{BA}}\right) \left(\frac{2n}{2n+1}\right) \qquad (2.21)$$

Since Eq. (2.20) is implicit, it is not possible to write Q as a function of Re explicitly using Eq. (2.21). Moreover, both Q and Re are unknowns. Nevertheless, such relations might be simply solved with the aid of a computer to find the zero of function. This is exactly how ultrasonic flow meters computers infer the mean flow velocity. Some manufactures use different formulation for the factor k [28, 36] aiming, for instance, better velocity profile fitting or computational performance on the calculation of the zero of the function.

At this point, it is important to remark the importance of knowing the velocity profile behaviour. Equation (2.21) shows that factor k (represented by the last term in parentheses as a function of n) interfere directly in the flow rate value. Such equation is a consequence of fully developed flow condition assumption. However, it is known that such condition may not occur in many practical situations. But how sensitive to non-ideal conditions is this measuring system?

In fact, the answer to this question would be "it depends". Next, the sensitivity of ultrasonic flow meters is better commented and the basic concept of multipath ultrasonic flow meters is briefly shown.

2.3.3 Multipath Ultrasonic Flow Meters

Figure 2.1 represents the most simple transit-time ultrasonic flow meter device. Actually, multipath ultrasonic flow meters provide better accuracy than single-path configurations. They are able to detect and compensate swirl and asymmetries [37, 38, 39, 40], to achieve higher accuracies [38, 41], to be used as a reference meter [42], and even to provide velocity profiles in some occasions [43].

Such improvements are possible due to extra pairs of ultrasonic transducers, which may be arranged in several configurations. Some of these arrangements are exemplified in Fig. 2.5 representing the acoustic paths of typical multipath ultrasonic flow meters.
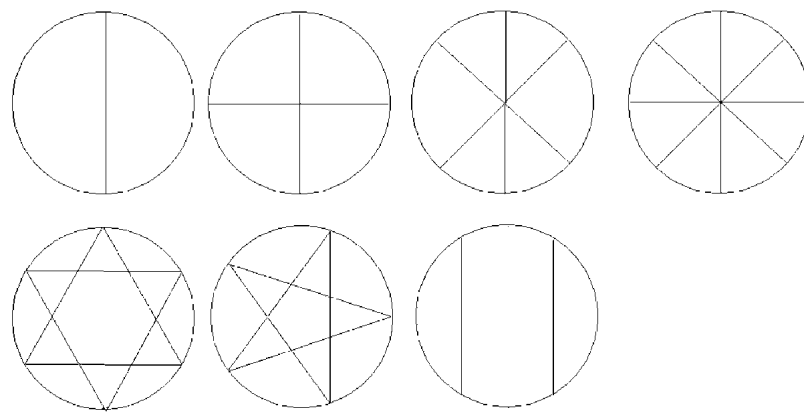
Figure 2.5. Schematic illustration of typical multipath configurations for ultrasonic flow meters. Adapted from [1].

The presence of other acoustic paths provides comparison between measured transit times and,

consequently, it is possible to analyse the flow field, detect patterns and swirl presence, and sometimes correct measurements. Obviously, multipath flow meters tend to provide better performances as the number of paths increases, but the configuration of transducers is crucial, as shown in [1, 21, 39, 40].

Despite all advantages mentioned above, multipath ultrasonic flow meters are reasonably more expensive than single-path devices. Hence, their use for flare gas installations is not profitable due to low values associated to flare gas flows. Although there is an available (but infeasible) improvement, single-path ultrasonic flow meters are commonly used in flare gas installations and the sensitivity of such device is still a relevant issue.

2.3.4 Uncertainty and Error Sources

Ultrasonic flow measurement is strongly dependent on the metering environment, electronics and flow behaviour. One may believe then that accurate measurements depend on several variables. In fact, AGA 9 [31] presents some influence factors of ultrasonic flow meters accuracy, such as:

- the precision on meter body and transducers locations measured dimensions;

- the velocity integration technique;

- the shape of the velocity profile at the metering section;

- the pulsation that may occur in the flow [44, 45, 46];

- the stability and accuracy of transit-time electronic sensors [47, 48, 49];

- flow calibrations [50, 51, 52].

Each factor above may be decomposed in various issues. As dimensional factors, for instance, one may consider pipe wall roughness [53], tolerances of manufacturing [54] and air intake in the recesses to mount the transducers [26, 55]. Since AGA 9 [31] brought these factors forward the scientific community tries to better understand how they affect the quality of flow rate measurements.

Some questions related to the sound interaction with the flow and the meter body are also object of study. Ultrasound propagation [56], acoustic deviation due to flow profile [30] and ray rescue (or recovery) angle [5, 30] are some examples of important factors still under investigation.

The influence of non-ideal velocity profiles is aimed in this dissertation and is better discussed in the next chapter. For complementary information on uncertainty and errors generation the reader is referred to the following texts [31, 54].

Chapter 3

Installation Effects

Usual operational conditions required for flow meters accuracy statements are steady flow of a single-phase, homogeneous Newtonian fluid. Furthermore, calibration procedures are carried out under laboratory conditions and the flow meter is usually placed in the middle of a sufficiently long straight pipe aiming fully developed flow condition. Any distinct situation is considered an influence and its consequences are often called *installation effects*.

Berrebi [19] proposes the classification of dynamic and static installation effects. Dynamic effects are generally caused by pulsating flow, whereas static effects may be "all permanent installation that differs from the long straight pipe placed upstream from the flow meter during its calibration" [19].

In practical situations, cavitation, pulsating flow, non-homogeneous flow and velocity profile deviation are pointed out as the most influential variables on flow measurement accuracy [20]. For instance, pulsating flows are considered in references [44, 45, 46] and non-Newtonian fluids measurements are conducted in references [57, 58]. Moreover, Miller [20] states that "velocity profile is probably the most important and least understood influence quantity".

In ultrasonic flow metering field, the velocity profile may be affected by different sources, such as disturbed flows [29, 59], non-Newtonian properties [57], transducers recesses and position [26, 55], pipe wall roughness [53], and flow regime (Re).

Because pipe elbows are commonly found in industrial pipeline configurations [19], their influ-

ence is widely investigated by both scientific and technological communities [4, 12, 21, 29, 52, 59, 60, 61, 62, 63]. There are certainly other relevant static installations, such as pipe reducers and expanders [58], valves and injectors, and pumps.

Pipe curves generate asymmetries on flow profile as well as swirl and secondary flow effects. Such disturbances caused by non-ideal flow conditions are characterized by tangential velocities. This chapter gathers experimental, analytical and numerical analysis of installations effects available in the literature. Patterns of disturbed flows and some known improvements on disturbed flow measurements are also commented.

3.1 Disturbed Flow Profiles and Ultrasonic Flow Measurement

Investigations on swirl decay in pipe flow carried out by Kreith and Sonju [64] and on secondary flow patterns by Dean [65, 66] are pioneering and remarkable works. Mattingly and Yeh [67] also have important contributions on swirl decay in pipe flow, particularly on its effects on flow measurements. Since then, installation effects have been investigated, even for other flow meters than ultrasonics. The approaches are usually experimental or numerical, but there are analytical contributions as well.

It is known that the flow field after pipe curves is complex. Pipe elbow configurations cause secondary and swirl flows, which may cause velocity profile disturbances (asymmetries). Furthermore, such disturbances may compromise the quality of flow measurement.

Because they are commonly found in industrial pipe installations, two usual upstream pipe configurations are widely tested in the literature: the single elbow (Fig. 3.1) and the double elbow out-of-plane (Fig. 3.2).

It is important to remark that Figs. 3.1, 3.2 and 3.3 are results of the present work. Since it is believed that they are illuminating figures, they have been anticipated in this chapter.

Figures 3.1 and 3.2 represent typical disturbances at 1.5D and 6D after each curve configuration. Three-dimensional profiles and the streamlines associated to them are shown. In Fig. 3.2 there

is also the stream line at an intermediary plane between the two curves.
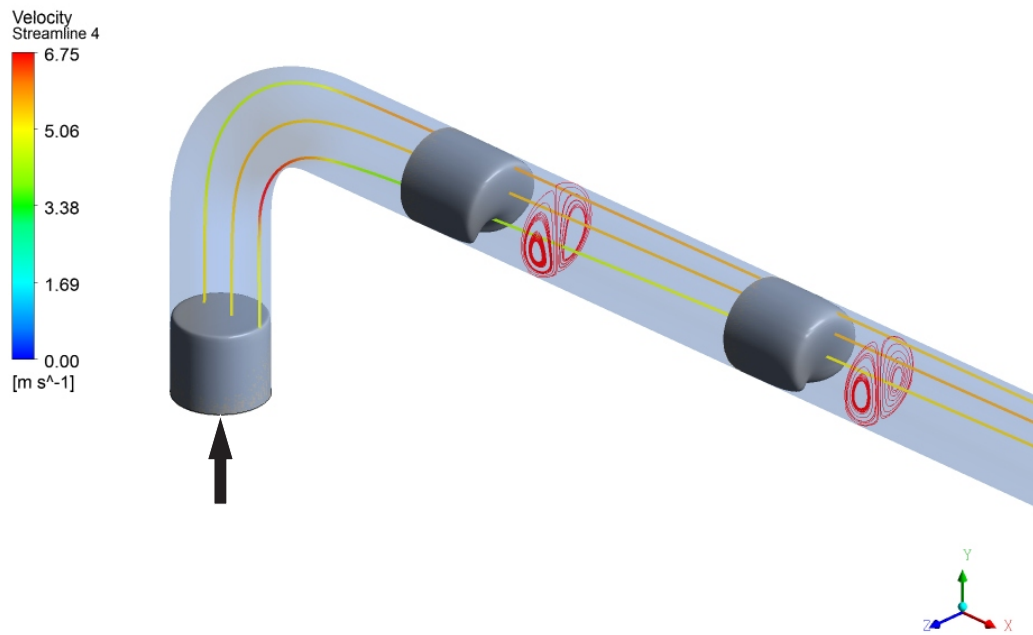
Figure 3.1. Profile disturbances for single elbow configuration: velocity surfaces and contours at inlet, 1.5D and 6D, and streamlines. ($Re = 1 \times 10^5$)
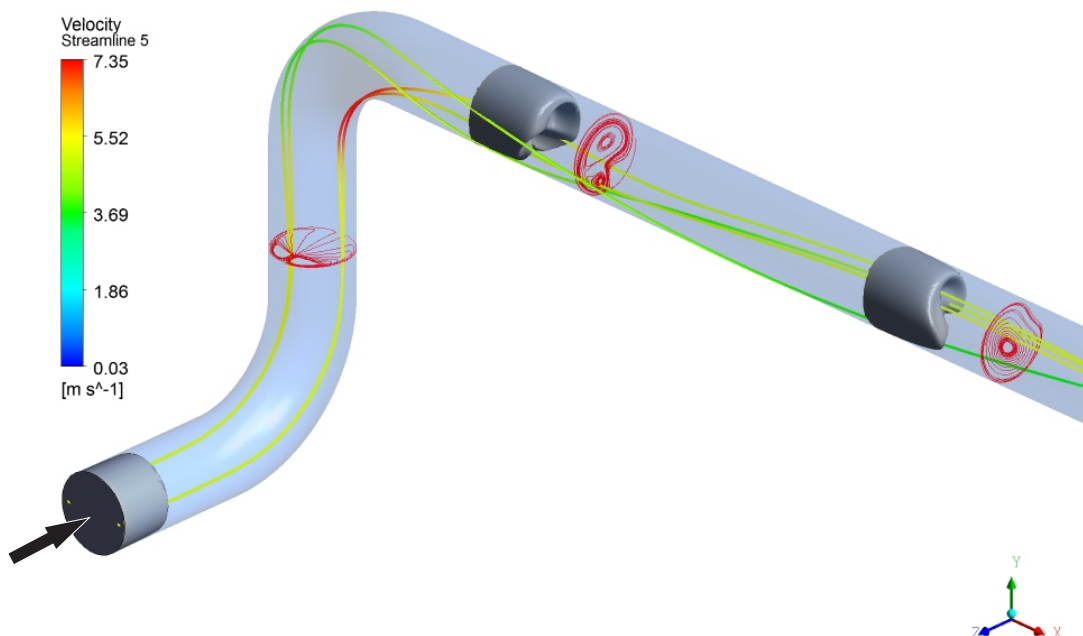
Figure 3.2. Profile disturbances for double elbow configuration: velocity surfaces and contours at inlet, 1.5D and 6D, and streamlines. ($Re = 1 \times 10^5$)

Single elbow installations typically generate cross-flows, which are secondary flows that usually produce two counter rotating vortices (Figs. 3.1 and 3.3a). Such behaviour is already observed by means of experiments [13, 60, 62, 65, 66, 68, 69] and CFD simulations [4]. The two vortices appears immediately after the end of the curve and their effect usually vanishes after 50D of straight pipe [63, 68, 69].

(a) $6D$ downstream from single elbow

(b) $1.5D$ downstream from double elbow

(c) $20D$ downstream from double elbow
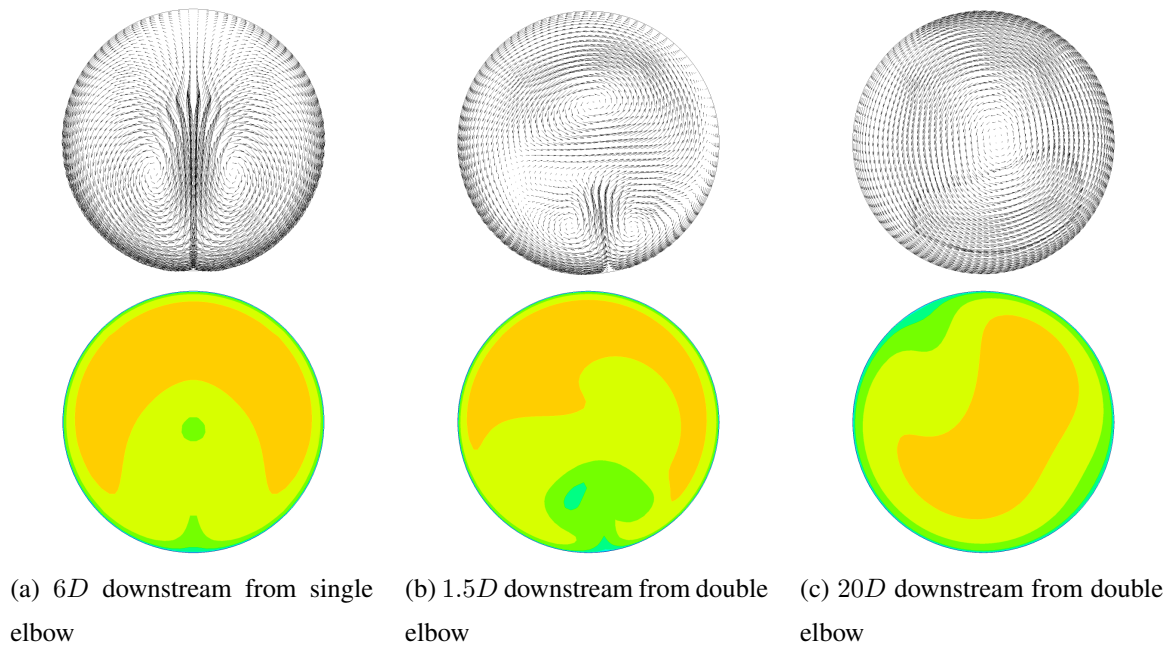
Figure 3.3. Tangential velocity vector and velocity contour representing typical disturbed profiles downstream of pipe elbows. ($Re = 1 \times 10^5$)

Double elbow out-of-plane installations usually reproduce similar cross-flow behaviour downstream from the first elbow (see Fig. 3.2). There is a superposition of cross-flow and swirl effects just after the second elbow (see Fig. 3.3b). Such summation of effects is characterized by two eccentric vortices: a main vortex which is bigger and stronger, and a smaller one which is mainly dominated by remaining cross-flow effects. It is remarkable that the smaller vortex vanishes rapidly and the main vortex, which is swirl-dominated, still rotates even after 100D [68, 69] (refer to Figs. 3.2 and 3.3). The eccentric feature of the main vortex is also lost along the straight pipe and swirl tend to become concentric. Such behaviour may be seen by comparing the streamlines at 1.5D and 6D in Fig. 3.2, and the velocity vectors in Fig. 3.3c.

As commented in Chapter 2, velocity profile deviates the acoustic path. It is analogous to rays refraction on geometrical optics. The velocity is deviated each time it encounters a velocity

gradient, as if it had reached a different medium. Figure 3.4 shows exaggerated acoustic paths for several flow profiles.
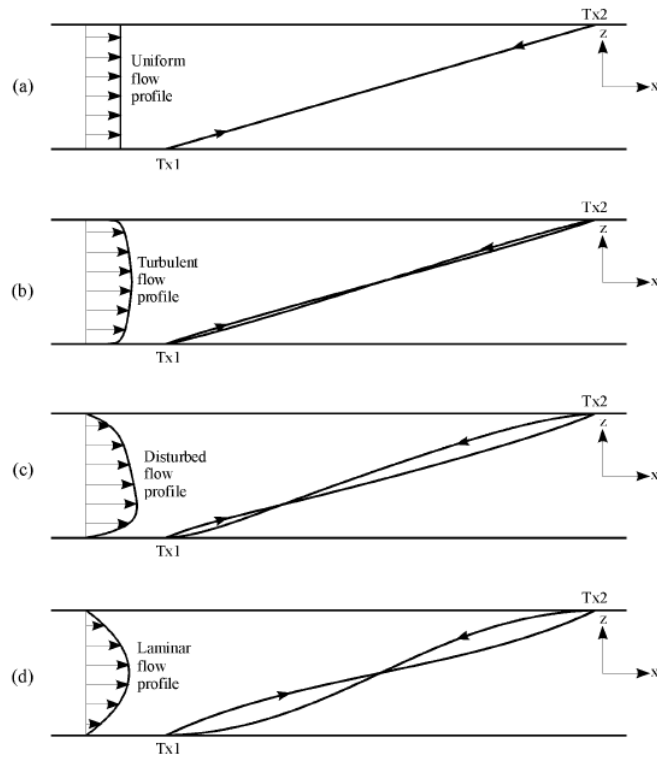
Figure 3.4. Exaggerated acoustic path deviation due to several flow profiles. [2]

One may note that, since the influence quantity is the velocity gradient, the flatter the velocity profile is, the less the acoustic path is deviated. Swirl and cross-flows are usually associated with profile asymmetries, as can be observed in the contour plots in Fig. 3.3. The deviation of acoustic paths is one of the mechanisms for installation effects due to disturbed profiles and is investigated in references [29, 30]. However, as already observed in Sec. 2.3.1, the acoustic path is assumed to be linear and non-deformable in this dissertation.

Despite the fact that the acoustic path is assumed to be a straight line, velocity profile asymmetries themselves also influence ultrasonic flow measurement. If the profile velocity is fully developed, any diametrical path (*i.e.*, any acoustic path passing by pipe center axis) may give the same flow rate measurement, since the term $\bar{V}_{UFM}$ is the integration of the same function (refer to Subsec. 2.3.1). Nevertheless, in the presence of asymmetries, the integrand function may vary with transducers mounting angle, represented here by θ (see Fig. 2.1), leading to different values for $\bar{V}_{UFM}$ and, therefore, for k and finally Q. Thus, transducers mounting angle has also been investigated in the presence of different disturbed profiles, as reported in references

[4, 12, 21, 29, 51, 63]. The influence of θ on the correction factor is carried out in Chapter 7.

Notwithstanding, asymmetries are not the only influencing mechanism and tangential velocity components also plays an important role in such context. Section 2.3.1 contains the derivation of the correction factor, which is based in fully developed flow condition. In fact, fully developed flow leads to constant axial velocity only, *i.e.* null tangential velocity components. On the other hand, swirl and cross-flow are dominated by tangential velocities which may compromise the quality of ultrasonic flow measurements. This subject is better commented in Chapter 7. For now, it is important to know that tangential velocity components may affect flow rate measurements.

3.2   Some Known Solutions and Restrictions – Why CFD?

The sensitivity of the flow meter to disturbed profiles depends on its measurement principle. Generally speaking, positive displacement flow meters (such as diaphragm and gear) are not sensitive to it. However, they introduce pulsations in the flow as well as significant pressure drop [19].

Regarding rotating flow and profile asymmetries, the use of flow conditioners is a well known tool and their results are mostly satisfactory [68, 69]. Nevertheless, there are restrictions for their usage in pipes with small diameter [19]. Furthermore, as commented in Chapter 1, flare gas installations are susceptible to over-pressures in which very high flow rates are achieved. Such occurrences may result in pressure and velocity values so high that the presence of flow conditioners in the pipeline would affect safety conditions. Thus, flow conditioners are not a suitable option for flare gas installations.

Multipath ultrasonic flow meters are also an option leading to diminish meter's sensitivity to disturbances. In fact, depending on the number and the arrangement of acoustic paths, they may provide very low uncertainties and be almost insensitive to flow disturbances [1, 37, 38, 41]. Also, several paths allow detecting disturbances and proposing corrections [39, 40]. However, as mentioned in Subsec. 2.3.3, multipath ultrasonic flow meters are rather expensive when compared to single-path devices and the low costs associated to flare gas flows make it impracticable.

Since the use of flow conditioners and multipath flow meters is not feasible, it is necessary to find reliable alternatives for *single-path* measurements. The first step is to investigate how disturbances affect flow rate measurements of single-path ultrasonic flow meters. In this sense, both experimental [13, 52, 63] and analytical [1] work have been conducted, but CFD simulations have shown to be an important tool [4].

Holm *et al.* [59] model the ultrasonic flow meter and present simulated correction factors under disturbed conditions. Hilgenstock and Ernst [4] compare simulated and measured profiles, and present the error on the correction factor as a function of disturbances and path configurations. Yeh and co-workers model acoustic paths under ideal and non-ideal flow conditions by means of wave functions interacting with the flow field [29] and use these results to propose improvements for flow measurement and calibration [51]. Iooss *et al.* [33] simulate the sensitivity of the flow rate due to flow profile and turbulence fluctuations.

The present work follows such tendency of CFD simulations, exploring the influence of Reynolds number, transducers mounting angle and axial position downstream from single and double elbow configurations. Next chapter presents the mathematical equations and the numerical methods considered by the CFD codes used in this dissertation.

Part II

Methodology

Chapter 4

Mathematical Modelling and Numerical Methods

Numerical simulation is an increasingly important tool, since it is cheap and fast compared to experiments. Moreover, it may provide reasonable results for a wide range of engineering problems when properly modelled. This chapter presents the equations considered for flow modelling (including turbulence treatment), the numerical methods and the mathematical treatment of boundary conditions used for solutions. Also the calculation of the numerical correction factor for simulating a ultrasonic flow meter is presented and short considerations on numerical errors and uncertainties are given as well.

4.1   Mathematical Modelling

4.1.1   Conservation Equations

Considering fluid incompressibility condition, the flow field of any Newtonian fluid may be represented by the mass (continuity) and the momentum (Naiver-Stokes) conservation equations (Eqs. (4.1) and (4.2), respectively).

$$\frac{\partial \rho}{\partial t} + \rho \frac{\partial u_i}{\partial x_i} = 0 \tag{4.1}$$

$$\rho \left[\frac{\partial u_i}{\partial t} + \frac{\partial \left(u_i u_j \right)}{\partial x_i} \right] = -\frac{\partial p}{\partial x_j} + \frac{\partial}{\partial x_i} \left[\mu \left(\frac{\partial u_i}{\partial x_j} + \frac{\partial u_j}{\partial x_i} \right) \right] \tag{4.2}$$

Where

- ρ is the fluid density [kg/m^3];

- t is the time [s];

- u_i is the velocity component in the direction i [m/s];

- x_i is the Cartesian coordinate in the direction i [m];

- p is the fluid static pressure [N/m^2];

- μ is the fluid dynamic viscosity [Pas].

Equations (4.1) and (4.2) represent a system of four equations (the continuity plus the momentum equation in the three Cartesian directions - x, y, z) and four unknowns (the pressure p and the three velocity components - u, v, w). Thus, they provide a single possible analytical solution and may provide adequate numerical solution if reasonable initial and boundary conditions are imposed. Analytical solutions are restricted to simple laminar cases (see chapter 5 of [35]). However, the direct numerical solution of this system is possible by means of the so called DNS (Direct Numerical Simulation) [70]. Since DNS provides the solution of Navier-Stokes equations (Eq. (4.2)), no model is used even for turbulent flows. Thus, when properly implemented, it gives laminar and turbulent results with experimental reliability. On the other hand, very fine discretization on space and time is necessary for capturing a wide range of turbulent scales, from the Kolmogorov scale to the largest possible according to the domain. Thus, DNS results have been widely used in turbulent phenomena investigation, although the huge computational effort to obtain such solution still limits its application to low Reynolds and simple geometry cases.

Because DNS is computationally expensive, practical alternatives aiming approximated solutions for complex cases have been studied. Turbulence models allow faster results for more complex cases by simplifications and approximations, for which coarser meshes might be considered. In this sense, large-eddy simulations (LES) [70, 71] model only the effect of the small-

est scales in larger scales and RANS (Reynolds Averaged Navier-Stokes) models use a statistical approach proposed by Osborne Reynolds [72] to model the effect of turbulent fluctuations in the mean flow. In this dissertation two RANS models have been considered: k–ε and k–ε RNG. Therefore, Eqs. (4.1) and (4.2) must be statistically manipulated. Next, Reynolds statistical treatment and the resulting RANS equations are briefly shown. For further information about other turbulence treatments the reader may consider the reference [73].

4.1.2   RANS-Equations

Since turbulence is a chaotic phenomenon, a simple approach is to decompose all turbulent quantities in mean values and zero-mean instantaneous fluctuations, as proposed by Reynolds [72]. Equation (4.3) presents such proposition.

$$u_i = \bar{u}_i + u_i' \tag{4.3}$$

Where

- $\bar{u}_i$ is the fluid mean turbulent velocity $[m/s]$;

- u_i' is the fluid turbulent velocity fluctuation $[m/s]$.

So that

$$\bar{u}_i = \lim_{t \to \infty} \frac{1}{t} \int_{t_o}^{t_o+t} u_i \, \mathrm{d}t^* \tag{4.4}$$

$$\bar{u'}_i = \lim_{t \to \infty} \frac{1}{t} \int_{t_o}^{t_o+t} \left(u_i - \bar{u}_i \right) \, \mathrm{d}t^* \equiv 0 \tag{4.5}$$

Where

- t^* is equivalent to the variable t and the superscript symbol is only used to differ the variable of integration $[s]$.

- $\bar{u'}_i$ is the average of the fluid turbulent velocity fluctuations $[m/s]$.

For the time average to make sense, the integrals above have to be independent of t_o. Therefore, the mean flow has to be steady ($\partial \bar{u}_i / \partial t = 0$).

It is necessary to remark that the formulation above, the way it is developed, is not valid for transient approach. In such cases, URANS (Unsteady Reynolds Average Navier-Stokes) development may be considered if a RANS-type approach is desired.

The pressure p is also decomposed in a mean value ($\bar{p}$) plus fluctuations (p'). The average of pressures fluctuations ($\bar{p'}$) is also null.

$$p = \bar{p} + p', \quad \bar{p'} \equiv 0 \tag{4.6}$$

By substituting Eqs. (4.3) and (4.6) into Eqs. (4.1) and (4.2), alternative forms for continuity and Navier-Stokes are obtained, yet without losses.

$$\frac{\partial \rho}{\partial t} + \frac{\partial \rho \left(\bar{u}_i + u'_i \right)}{\partial x_i} = 0 \tag{4.7}$$

$$\rho \left\{ \frac{\partial \left(\bar{u}_i + u'_i \right)}{\partial t} + \frac{\partial \left[\left(\bar{u}_i + u'_i \right) \left(\bar{u}_j + u'_j \right) \right]}{\partial x_i} \right\} = \\ -\frac{\partial \left(\bar{p} + p' \right)}{\partial x_j} + \frac{\partial}{\partial x_i} \left\{ \mu \left[\frac{\partial \left(\bar{u}_i + u'_i \right)}{\partial x_j} + \frac{\partial \left(\bar{u}_j + u'_j \right)}{\partial x_i} \right] \right\} \tag{4.8}$$

However, the proposition of RANS models is to obtain the mean flow. Thus, the next step is to take the time average of Eqs. (4.7) and (4.8), yielding the basic equations of all RANS models. Some mathematical assumptions and manipulations [74] are carried out in order to obtain Eqs. (4.9) and (4.10) as follows.

$$\frac{\partial \bar{u}_i}{\partial x_i} = 0 \tag{4.9}$$

$$\rho \bar{u}_i \frac{\partial \bar{u}_j}{\partial x_i} = -\frac{\partial \bar{p}}{\partial x_j} + \frac{\partial}{\partial x_i} \left[\mu \left(\frac{\partial \bar{u}_i}{\partial x_j} + \frac{\partial \bar{u}_j}{\partial x_i} \right) - \rho \overline{u'_i u'_j} \right] \tag{4.10}$$

The term $-\rho\overline{u'_i u'_j}$ which appears in Eq. (4.10) is a symmetric stress tensor. Such stress tensor represents the contribution of turbulent fluctuations to the mean flow. Since it comes from Reynolds treatment, it is specially known as *Reynolds stress tensor*. The Reynolds stress tensor is represented in the following way.

$$\tau_{Tij} = -\rho\overline{u'_i u'_j} = -\rho \begin{bmatrix} \overline{u'u'} & \overline{u'v'} & \overline{u'w'} \\ \overline{v'u'} & \overline{v'v'} & \overline{v'w'} \\ \overline{w'u'} & \overline{w'v'} & \overline{w'w'} \end{bmatrix} \tag{4.11}$$

Now, Eqs. (4.9) and (4.10) give a four equation and ten unknown system. The unknowns are: the three mean flow velocity components ($\bar{u}_i$), the mean flow pressure ($\bar{p}$) and the six (because of symmetry) components of the Reynolds stress tensor (τ_{Tij}). The different ways of treating the Reynolds stress tensor characterize each RANS turbulence model.

4.1.3 Turbulence Modelling

In this dissertation, two commercially available CFD codes, ANSYS CFX [75] and ANSYS FLUENT [76], have been used in order to achieve numerical solution for the system represented by Eqs. (4.9) and (4.10). In addition to such equations, turbulence modelling requires extra equations. In the present work, two turbulence models have been carried out: standard k–ε and k–ε RNG. In the following subsections, some preliminary concepts are introduced and the standard k–ε model is briefly presented. At last, some considerations concerning the k–ε RNG model are added.

4.1.3.1 Boussinesq Hypothesis

Boussinesq [77] made the first attempt to treat the Reynolds stress tensor by analogy to the constitutive equation for isotropic Newtonian fluid [35] (or Newton's Law [3]), which is given by Eq. (4.12).

$$\tau_{ij} = 2\mu S_{ij} = \mu \left(\frac{\partial u_i}{\partial x_j} + \frac{\partial u_j}{\partial x_i} \right) \tag{4.12}$$

Where

- τ_{ij} is the shear stress tensor;

- S_{ij} is the strain rate tensor.

Boussinesq proposed introducing a turbulent coefficient in order to relate the turbulent stress with the mean flow strain rate. Such assumption became well known as the *Boussinesq hypothesis* and is represented by Eq. (4.13). The turbulent coefficient (μ_T) "corresponds to the viscosity in laminar flow and is, therefore, called *apparent* or *virtual* (also *eddy*) *viscosity*" [35] or *turbulent coefficient exchange for momentum* [74].

$$\tau_{Tij} = -\rho\overline{u'_i u'_j} = 2\mu_T\bar{S}_{ij} - \frac{2}{3}\rho k\delta_{ij} = \mu_T\left(\frac{\partial\bar{u}_i}{\partial x_j} + \frac{\partial\bar{u}_j}{\partial x_i}\right) - \frac{2}{3}\rho k\delta_{ij} \tag{4.13}$$

Where

- $\bar{S}_{ij}$ is the strain rate of the mean flow, given by $\frac{1}{2}\left(\dfrac{\partial\bar{u}_i}{\partial x_j} + \dfrac{\partial\bar{u}_j}{\partial x_i}\right)$;

- k is the turbulent kinetic energy [74, 73, 3], defined as $k \equiv \dfrac{\overline{u'^2_i}}{2}$ $[m^2/s^2]$;

- δ_{ij} is the Kronecker delta.

The last term is added in order to maintain a non-zero value ($= -\rho\overline{u'_i u'_i}$) to the Reynolds stress tensor trace (*i.e.*, τ_{Tii}).

Both CFX and FLUENT model the Reynolds stress as follows.

$$\tau_{Tij} = \mu_T\left(\frac{\partial\bar{u}_i}{\partial x_j} + \frac{\partial\bar{u}_j}{\partial x_i}\right) - \frac{2}{3}\left(\rho k + \mu_T\frac{\partial\bar{u}_k}{\partial x_k}\right)\delta_{ij} \tag{4.14}$$

Although, according to their documentation [78, 79], the term $\partial\bar{u}_k/\partial x_k$ is very small for incompressible flows.

With such assumption, Eqs. (4.9) and (4.10) give now six unknowns: the three velocity components and the pressure of the mean flow, the eddy viscosity and the turbulent kinetic energy. The equations of RANS models that use Boussinesq hypothesis present solutions by modelling these

new unknowns (μ_T and k). On the other hand, RANS models that are not based on Boussinesq hypothesis use different approach to the Reynolds stress treatment. Generally, such different approach eliminates the need of modelling the turbulent kinetic energy (k).

4.2 Boundary Conditions

Equations (4.9) and (4.10) plus turbulence equations (which depends on the chosen model) allow obtaining results for the flow field. However, since all modelling is based on differential equations, boundary conditions for each equation are necessary for the solution.

All simulations in the present work have been performed for pipe installations, which means that main boundary conditions are: inlet plane, pipe internal wall and outlet plane. The mathematical treatment for each of these boundaries are commented in the following.

4.2.1 Inlet Conditions

Inlet conditions for momentum equations are usually constrained by velocity or pressure. Because both uniform and fully developed velocity profiles have been desired for the simulations in the present work, all inlet conditions have been constrained by velocity. Pressure values appear as a consequence of the numerical procedure in order to provide the specified velocity profile.

The velocity profile at entrance has been assumed to be always normal to the inlet plane. Uniform velocity profile has been considered, except for some validation cases (Chapter 6) in which fully developed flow profile has been tested. Inlet velocity boundary conditions may be mathematically expressed as follows.

$$\bar{u}_i\big|_{inlet} = \begin{cases} V_{spec}, & \text{if} \quad i = \text{normal direction} \\ 0, & \text{otherwise} \end{cases} \tag{4.15}$$

Where

- V_{spec} is the specified velocity magnitude.

For uniform velocity profiles V_{spec} is unique, but for fully developed profile V_{spec} is given by the Nikuradse profile, as in Eq. (2.18). In both uniform and fully developed cases the mean velocity is obtained by the desired Reynolds number, as shown in Eq. (4.16).

$$\bar{u}_m = \frac{\mu Re}{\rho D} \tag{4.16}$$

Equation (2.18) requires knowing $\bar{u}_{max}$ and it is easy to show [35] that the relation between $\bar{u}_{max}$ and $\bar{u}_m$ for Nikuradse profile is given by Eq. (4.17).

$$\frac{\bar{u}_m}{\bar{u}_{max}} = \frac{2n^2}{(n+1)(2n+1)} \tag{4.17}$$

Inlet conditions for k and ε are also necessary and two different approaches have been tested. It is possible to set the values for k and ε directly, yielding Eqs. (4.18) and (4.19).

$$k\Big|_{inlet} = k_{spec} \tag{4.18}$$

And

$$\varepsilon\Big|_{inlet} = \varepsilon_{spec} \tag{4.19}$$

Notwithstanding, the values for k and ε may also be calculated by other parameters, such as turbulence intensity (I) and viscosity ratio ($\tilde{\mu}$). The turbulence intensity is defined as the RMS velocity fluctuations (u'_{RMS}) divided by the mean flow velocity ($\bar{u}_m$), as shown in Eq. (4.20).

$$I \equiv \frac{u'_{RMS}}{\bar{u}_m} \tag{4.20}$$

The viscosity ratio is given by Eq. (4.21), as follows.

$$\tilde{\mu} \equiv \frac{\mu_T}{\mu} \tag{4.21}$$

Inlet values for k and ε are finally obtained by Eqs. (4.22) and (4.23), respectively.

$$k\big|_{inlet} = \frac{3}{2}\bar{u}_m^2 I^2 \tag{4.22}$$

$$\varepsilon\big|_{inlet} = \rho C_\mu \frac{k_{inlet}^2}{\mu\tilde{\mu}} = \rho C_\mu \frac{k_{inlet}^2}{\mu_T} \tag{4.23}$$

4.2.2 Wall Conditions

Stationary wall with no-slip condition has been considered. Thus, all velocity components at the wall are null.

$$\bar{u}\big|_{wall} = \bar{v}\big|_{wall} = \bar{w}\big|_{wall} = 0 \tag{4.24}$$

It is known that successful predictions of wall-bounded turbulent flows depend on good representation of near-wall flow. In this sense, *wall functions* are common in CFD approach, so that solved variables might be constrained by semi-empirical relations in near-wall regions. It is shown that turbulent near-wall region may be divided into layers (refer to [35, 74] for details). Region adjacent to the wall is dominated by viscous effects whereas in the outer layer, named *inertial layer* by Tennekes and Lumley [74], the major role is played by turbulence. In such region, the so called *log-law* given by Eq. (4.25) is valid and is applied by both CFX and FLUENT.

$$u^* = \frac{1}{\kappa}\ln(Ey^*) \tag{4.25}$$

Where

- u^* is a dimensionless velocity calculated by Eq. (4.26);

- y^* is a dimensionless distance from the wall computed by Eq. (4.27);

- κ is the Von-Kármán constant ($= 0.4178$);

- E is a empirical constant ($= 9.793$ for smooth pipes).

$$u^* \equiv \frac{\bar{u}_P C_\mu^{1/4} k_P^{1/2}}{\tau_w \rho} \tag{4.26}$$

$$y^* \equiv \frac{\rho y_P C_\mu^{1/4} k_P^{1/2}}{\mu} \tag{4.27}$$

Where

- $\bar{u}_P$ is the turbulent mean velocity at a near-wall mesh node P;

- k_P is the turbulent kinetic energy at a near-wall mesh node P;

- τ_w is the wall shear stress;

- y_P is the distance between the near-wall mesh point P and the wall.

Regarding Eqs. (4.26) and (4.27), on may noticed that wall functions depend on distances between the wall and the first mesh node adjacent to it (see Sec. 4.3). In fact, mesh refinement could cause the presence of mesh nodes in the viscous layers, which may results in poor predictions, since log-law would be imposed anyway. In order to overcome this issue, both CFX and FLUENT propose the so called *scalable wall function*. Such function limits the variable y^*, replacing it by the relation in Eq. (4.28).

$$\tilde{y^*} = max(y^*, y_{limit}^*) \tag{4.28}$$

Where

- $\tilde{y^*}$ is the modified dimensionless distance from the wall;

- y_{limit}^* is the limiter for guaranteeing that $\tilde{y^*}$ is always in the inertial layer, regardless of mesh refinement. This limiter equals 11.06 in CFX and 11 in FLUENT.

With such approach, log-law is applied to inertial layer and viscous layer (*i.e.*, $\tilde{y^*} < y_{limit}^*$) receives the following laminar assumption given by Eq. (4.29).

$$u^* = y^* \tag{4.29}$$

For the turbulent kinetic energy, zero-gradient has been considered at the wall.

$$\left.\frac{\partial k}{\partial n}\right|_{wall} = 0 \tag{4.30}$$

Turbulence energy dissipation (ε) has a special treatment at the wall. Local equilibrium hypothesis [73, 74] is assumed in wall-adjacent control volumes, yielding Eq. (4.31).

$$\mathcal{P}_k = \varepsilon \tag{4.31}$$

The production term in the vicinity of the wall may be given by the relation in Eq. (4.32).

$$\mathcal{P}_k \approx \tau_w \frac{\partial \bar{u}}{\partial y} = \frac{\tau_w^2}{\kappa k_P^{1/2} y_P} \tag{4.32}$$

Finally, ε is calculated at a near-wall point P as follows.

$$\varepsilon_P = \frac{C_\mu^{3/4} k_P^{1/2}}{\kappa y_P} \tag{4.33}$$

Wall functions play an important role in turbulent flow predictions. However, from the perspective of the present work, they are merely helpful tools and their influence have not been tested. Such investigation is left as a suggestion for future work.

4.2.3 Outlet Conditions

Outlet constraints for momentum equation are given by pressure conditions. In such condition, static pressure is taken to be constant over the outlet plane, yielding Eq. (4.34).

$$\left.\bar{p}\right|_{outlet} = \bar{p}_{spec} \tag{4.34}$$

CFX also present the average static pressure over outlet, which accept pressure variations but guarantees that the mean value over the outlet plane equals the specified value by Eq. (4.35).

$$\bar{p}\big|_{outlet} = \bar{p}_{spec} = \frac{1}{A_{outlet}} \int\limits_{A_{outlet}} \bar{p}_{np,outlet} \, \mathrm{d}A \tag{4.35}$$

Where

- A_{outlet} is the area of the outlet plane;

- $\bar{p}_{np,outlet}$ is the pressure value at each nodal point (np) at the outlet plane.

Generally speaking, fully developed flow condition is desirable at outlet boundaries so that the gradients of all variables (except pressure) may be zero in the direction of the flow. Zero-gradient assumption is quite common in CFD codes. It imposes variable values for velocity and turbulence quantities to be extrapolated from the interior to outside the domain.

Such classical conditions may be described by the set of Eqs. (4.36) to (4.38).

$$\frac{\partial \bar{u}}{\partial n}\bigg|_{outlet} = \frac{\partial \bar{v}}{\partial n}\bigg|_{outlet} = \frac{\partial \bar{w}}{\partial n}\bigg|_{outlet} = 0 \tag{4.36}$$

$$\frac{\partial k}{\partial n}\bigg|_{outlet} = 0 \tag{4.37}$$

$$\frac{\partial \varepsilon}{\partial n}\bigg|_{outlet} = 0 \tag{4.38}$$

Since zero-gradient constraints expect fully developed flow conditions the location of the outlet boundary is a crucial point aiming to avoid unrealistic results. It is possible that the velocity profile still changes in the flow direction and thus a sensitivity study is desirable in order to demonstrate that the solution is not affected by the location of the outlet [3]. Such sensitivity test is shown in Chapter 5.

4.2.3.1 Brief Considerations on Flow Kinetic Energy

The instantaneous kinetic energy of the flow may be also decomposed in mean and turbulent (fluctuations) values, as shown in Eq. (4.39).

$$k_t = \bar{k} + k \tag{4.39}$$

Where

- k_t is the kinetic energy of the flow, defined as $k_t \equiv \dfrac{u_i{}^2}{2}$;

- $\bar{k}$ is the kinetic energy of the mean flow, defined as $\bar{k} \equiv \dfrac{\bar{u}_i^2}{2}$;

- k is the turbulent kinetic energy associated to velocity fluctuations.

The equation for the mean flow kinetic energy may be obtained by multiplying Eq. (4.10) (mean flow momentum equation) by $\bar{u}_i$. Some algebraic manipulation [74] may lead to Eq. (4.40).

$$\rho \bar{u}_j \frac{\partial \bar{k}}{\partial x_j} = \frac{\partial}{\partial x_j} \left(-\overline{pu_j} + 2\mu \overline{u_i S_{ij}} - \rho \bar{u}_i \overline{u_i' u_j'} \right) - 2\mu \bar{S}_{ij} \bar{S}_{ij} + \rho \overline{u_i' u_j'} \bar{S}_{ij} \tag{4.40}$$

From left to right, these terms represent: transport of $\bar{k}$ by convection, transport of $\bar{k}$ by pressure, transport of $\bar{k}$ by viscous stresses, transport of $\bar{k}$ by Reynolds stress, rate of viscous dissipation of $\bar{k}$ and rate of destruction of $\bar{k}$ due to turbulence production [3].

A similar equation may be obtained for the turbulent kinetic energy, by multiplying the Naiver-Stokes equation (4.2) by u_i, applying Reynolds decomposition, as in Eqs. (4.3) and (4.6), and subtracting Eq. (4.40) from the resulting equation. In other words, obtain the turbulent kinetic energy (k) by subtracting the mean flow kinetic energy ($\bar{k}$) contribution from the total kinetic energy (k_t). After some rearrangements, Eq. (4.41) is obtained.

$$\rho \bar{u}_j \frac{\partial k}{\partial x_j} = \frac{\partial}{\partial x_j} \left(-\overline{p' u_j'} + 2\mu \overline{u_i' S_{ij}'} - \rho \frac{1}{2} \bar{u}_i \overline{u_i' u_j'} \right) - 2\mu \overline{S_{ij}' S_{ij}'} - \rho \overline{u_i' u_j'} \bar{S}_{ij} \tag{4.41}$$

Where

- $\bar{S}'_{ij}$ is the time-averaged turbulent strain rate, given by $\dfrac{1}{2}\left(\dfrac{\partial \bar{u}'_i}{\partial x_j} + \dfrac{\partial \bar{u}'_j}{\partial x_i}\right)$.

From left to right, these terms represent: transport of k by convection, transport of k by pressure, transport of k by viscous stresses, transport of k by Reynolds stress, rate of dissipation of k and rate of production of k [3].

It is remarkable the important role played by the last terms in Eqs. (4.40) and (4.41). They are the same term with opposite sign. It is possible to show [3, 73] that the last term in Eq. (4.41) contributes positively, hence representing the production of k. When divided by ρ, such term gives the so called production of turbulent kinetic energy ($\mathcal{P}_k$), or simply production [3, 74].

$$\mathcal{P}_k \equiv -\overline{u'_i u'_j}\,\bar{S}_{ij} \tag{4.42}$$

However, in Eq. (4.40), the last term gives a negative contribution. This relation expresses the maintenance of turbulence by capturing mean flow kinetic energy and converting into turbulent kinetic energy [3, 73, 74].

The term $2\mu\overline{S'_{ij}S'_{ij}}$ in Eq. (4.41) is also very important, since it represents viscous dissipation by fluctuation motions. When divided by ρ, such term represents the rate of dissipation of turbulent kinetic energy per unit mass, ε, as given by Eq. (4.43) [3, 73, 74].

$$\varepsilon \equiv 2\nu\overline{S'_{ij}S'_{ij}} \tag{4.43}$$

Where

- ν is the kinematic viscosity given by μ/ρ.

The quantity ε is essential for the study of turbulence, since it represents the dissipation of turbulent kinetic energy.

4.2.3.2 The Standard k–ε Model

The standard k–ε model [80, 81, 82] calculates the eddy viscosity as given by Eq. (4.44).

$$\mu_T = \rho C_\mu \frac{k^2}{\varepsilon} \tag{4.44}$$

Where

- C_μ is a constant of the model [80] whose value is presented in Tab. 4.1.

In order to obtain the solution of the set of Eqs. (4.9), (4.10), (4.13) and (4.44), the solutions for k and ε are still needed. Jones and Launder [81] proposed two extra transport equations to these unknowns. The transport equations for k and ε are, respectively, Eqs. (4.45) and (4.46).

$$\rho \bar{u}_j \frac{\partial k}{\partial x_j} = \frac{\partial}{\partial x_i} \left[\left(\mu + \frac{\mu_T}{\sigma_k} \right) \frac{\partial k}{\partial x_i} \right] + \rho \mathcal{P}_k - \rho \varepsilon \tag{4.45}$$

$$\rho \bar{u}_j \frac{\partial \varepsilon}{\partial x_j} = \frac{\partial}{\partial x_i} \left[\left(\mu + \frac{\mu_T}{\sigma_\varepsilon} \right) \frac{\partial \varepsilon}{\partial x_i} \right] + C_1 \rho \frac{\varepsilon}{k} \mathcal{P}_k - C_2 \rho \frac{\varepsilon^2}{k} \tag{4.46}$$

Where

- σ_k, σ_ε, C_1 e C_2 are constants of the model [80] and their values are presented in Tab. 4.1.

Table 4.1. Constants of the standard k–ε model.

C_μ	σ_k	σ_ε	C_1	C_2
0.09	1.0	1.3	1.44	1.92

One may notice that the last two terms in k-equation (4.45) are obtained by using Eqs. (4.42) and (4.43) in the last two terms in Eq. (4.41). Moreover, all turbulent transport terms in Eq. (4.41) (terms in parentheses) are modelled with a gradient-diffusion hypothesis [73], yielding the term in brackets in Eq. (4.45).

It is now important to present the distinct approaches by CFX and FLUENT regarding the production term. Both follow the common procedure of using Boussinseq hypothesis for the Reynolds stress contribution. However, CFX presents the production term as shown in Eq. (4.47) and FLUENT defines it as given by Eq. (4.48).

$$\rho\mathcal{P}_k = \mu_T \left(\frac{\partial \bar{u}_i}{\partial x_j} + \frac{\partial \bar{u}_j}{\partial x_i} \right) \frac{\partial \bar{u}_i}{\partial x_j} - \frac{2}{3} \frac{\partial \bar{u}_k}{\partial x_k} \left(3\mu_T \frac{\partial \bar{u}_k}{\partial x_k} + \rho k \right) \quad (4.47)$$

$$\rho\mathcal{P}_k = \mu_T \bar{S}^2 \quad (4.48)$$

Where

- $\bar{S}$ is the modulus of the mean strain rate, defined as $\bar{S} \equiv \sqrt{2S_{ij}S_{ij}}$

For further information on the standard k–ε model the reader is referred to the references [81, 80, 82, 73, 3].

4.2.3.3 The k–ε RNG Model

The k–ε RNG model is based on the statistical mechanics approach [83, 84] by the renormalization group (RNG). The procedure involves quite abstruse mathematics [3] (which is summarized in reference [84] and detailed in the references therein) and provides the following advantage: a strain-based additional production term in its ε equation that is the main responsible for the different (usualy better) performance of RNG compared to standard model. Such difference is usually more remarkable in flows under high strain rates.

RNG equations are similar to the standard k–ε model, but CFX and FLUENT use different equations. CFX equations for k and ε are Eqs. (4.49) and (4.50).

$$\rho \bar{u}_j \frac{\partial k}{\partial x_j} = \frac{\partial}{\partial x_i} \left[\left(\mu + \frac{\mu_T}{\sigma_{kRNG}} \right) \frac{\partial k}{\partial x_i} \right] + \rho\mathcal{P}_k - \rho\varepsilon \quad (4.49)$$

$$\rho \bar{u}_j \frac{\partial \varepsilon}{\partial x_j} = \frac{\partial}{\partial x_i} \left[\left(\mu + \frac{\mu_T}{\sigma_{\varepsilon RNG}} \right) \frac{\partial \varepsilon}{\partial x_i} \right] + C^*_{1RNG}\rho\frac{\varepsilon}{k}\mathcal{P}_k - C_{2RNG}\rho\frac{\varepsilon^2}{k} \quad (4.50)$$

Where

- σ_{kRNG} , $\sigma_{\varepsilon RNG}$ e C_{2RNG} are constants of the model [78, 84] whose values are presented in Tab. 4.2.

The term C^*_{1RNG} in Eq. (4.50) is the additional one mentioned above and is given by Eq. (4.51).

$$C^*_{1RNG} = C_{1RNG} - f_\eta \tag{4.51}$$

Where

- C_{1RNG} is a constant of the model [84] whose value is presented in Tab. 4.2;

- f_η is commented below.

When multiplied by the neighbouring terms in Eq. (4.50), the first term in the right-hand side of Eq. (4.51) recovers the production term of the standard model, whereas the second term contributes to additional turbulent strain information and is given by Eq. (4.52).

$$f_\eta = \frac{\eta \left(1 - \dfrac{\eta}{\eta_0} \right)}{1 + \beta \eta^3} \tag{4.52}$$

Where

- η is the ratio of the turbulence to mean strain time scale [84] given in CFX by Eq. (4.53);

- η_0 and β are constants of the model [84] whose values are presented in Tab. 4.2.

In CFX, η is given by Eq. (4.53).

$$\eta = \sqrt{\frac{\mathcal{P}_k}{C_{\mu RNG} \varepsilon}} \tag{4.53}$$

Where

- $C_{\mu RNG}$ is a constant of the model [84] whose value is presented in Tab. 4.2.

On the other hand, FLUENT equations for k and ε are Eqs. (4.54) and (4.55).

$$\rho \bar{u}_j \frac{\partial k}{\partial x_j} = \frac{\partial}{\partial x_i} \left(\alpha_k \mu_{eff} \frac{\partial k}{\partial x_i} \right) + \rho \mathcal{P}_k - \rho \varepsilon \tag{4.54}$$

Table 4.2. Constants of the k–ε RNG model – CFX.

$C_{\mu RNG}$	σ_{kRNG}	$\sigma_{\varepsilon RNG}$	C_{1RNG}	C_{2RNG}	η_0	β
0.085	0.7179	0.7179	1.42	1.68	4.38	0.012

$$\rho \bar{u}_j \frac{\partial \varepsilon}{\partial x_j} = \frac{\partial}{\partial x_i} \left(\alpha_\varepsilon \mu_{eff} \frac{\partial \varepsilon}{\partial x_i} \right) + C_{1RNG} \rho \frac{\varepsilon}{k} \mathcal{P}_k - C_{2RNG} \rho \frac{\varepsilon^2}{k} - \mathcal{R} \tag{4.55}$$

Where

- α_k , α_ε are constants of the model [84], both equal to 1.39;

- μ_{eff} is the so called effective viscosity [3], defined as $\mu + \mu_T$.

The term $\mathcal{R}$ in Eq. (4.55) plays the role of the additional strain term and is given by Eq. (4.56).

$$\mathcal{R} = \frac{C_{\mu RNG} \rho \eta^3 \left(1 - \dfrac{\eta}{\eta_0} \right)}{1 + \beta \eta^3} \frac{\varepsilon^2}{k} \tag{4.56}$$

Where $C_{\mu RNG}$ is equal to 0.0845 and η is calculated in FLUENT as follows.

$$\eta = \frac{\bar{S} k}{\varepsilon} \tag{4.57}$$

All other constants presented in Eqs. (4.55) and (4.56) are the same of those in Tab. 4.2.

4.3 Numerical Methods

Both software considered in the present work use the Finite Volume (or Control Volume) Method [3] for obtaining discrete governing equations algebraic system. This section presents basic notions of the Finite Volume Method as well as some schemes and criteria necessary for the solution.

4.3.1 The Finite Volume Method

The Finite Volume Method consists in integrating the conservation equations presented in the last section over control volumes.

At first, one may consider the steady convection-diffusion of a property ϕ. Such process may be represented by the following transport equation [3].

$$div\left(\rho\mathbf{u}\phi\right) = div\left(\Gamma\,grad\,\phi\right) + S_\phi \tag{4.58}$$

Where

- div is the divergence operator, defined for a vector ϕ_i as $div\,\phi_i = \dfrac{\partial\phi_i}{\partial x_i}$;

- $grad$ is the gradient operator, defined for a scalar ϕ as $grad\,\phi = \dfrac{\partial\phi}{\partial x_i}\hat{e}_i$, and for a vector ϕ_i as $grad\,\phi_i = \dfrac{\partial\phi_i}{\partial x_j}\hat{e}_i\hat{e}_j$, where $\hat{e}_i$ and $\hat{e}_j$ are the unit vectors in the directions i and j, respectively;

- $\mathbf{u}$ is the velocity vector $[m/s]$;

- ϕ is the property being transported whose units may vary;

- Γ is the diffusion coefficient whose units depend on ϕ;

- S_ϕ is the term for ϕ source whose units depend on ϕ.

The control volume integration of Eq. (4.58) yields Eq. (4.59).

$$\int\limits_{CV} div\left(\rho\mathbf{u}\phi\right)\,\mathrm{d}V = \int\limits_{CV} div\left(\Gamma\,grad\,\phi\right)\,\mathrm{d}V + \int\limits_{CV} S_\phi\,\mathrm{d}V \tag{4.59}$$

Where

- CV represents the control volume;

- $\mathrm{d}V$ is the infinitesimal volume element $[m^3]$.

The Divergence Theorem [85] is now presented, in order to rewrite the volume integrals as surface integrals over the control volume bounding surfaces. For a vector $\mathbf{F}$ the theorem states the following.

$$\int_{CV} div\,\mathbf{F}\,\mathrm{d}V = \int_A \mathbf{F} \cdot \mathbf{n}\,\mathrm{d}A \tag{4.60}$$

Where

- $\mathrm{d}A$ is the infinitesimal surface element $[m^2]$;

- $\mathbf{n}$ is the vector normal to surface element $\mathrm{d}A$.

Applying the Divergence Theorem, Eq. (4.59) may be now rewritten.

$$\int_A (\rho\mathbf{u}\phi) \cdot \mathbf{n}\,\mathrm{d}A = \int_A (\Gamma\,grad\,\phi) \cdot \mathbf{n}\,\mathrm{d}A + \int_{CV} S_\phi\,\mathrm{d}V \tag{4.61}$$

It is now necessary to divide the domain into control volumes where Eq. (4.61) might be solved. Such division is usually called *discretization* and is briefly presented in the following subsection.

4.3.2 Discretized Equations

Discretization of conservation equations leads to linearized equations for each control volume. For instance, one may consider the transport of a property ϕ over a one-dimensional domain where the values for ϕ at boundaries A and B are known, as shown in Fig. 4.1.
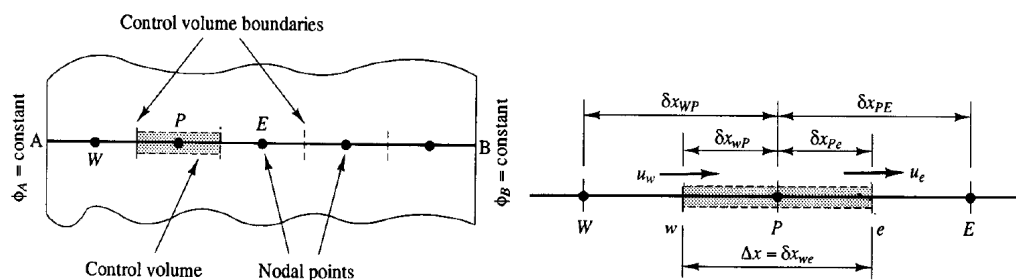
Figure 4.1. One-dimensional discretization and control volume details. Adapted from [3].

The domain presented in Fig. 4.1 has five nodal points, which are the center of each control volume. Control volume faces are positioned mid-way between neighbouring nodes.

Upper cases indicate nodal points to the west (W) and east (E) of a general nodal point P. Lower cases indicates the west (w) and east (e) faces around the same point P. The distances between W and P, and between P and E, are δx_{WP} and δx_{PE}, respectively. For the faces, δx_{wP} indicates the distance between the face w and the point P, and δx_{Pe} indicates the distance between the point P and the face e. The control volume width is $\Delta x = \delta x_{we}$.

The discretized equation at the nodal point P is obtained by applying Eq. (4.61) to the control volume around it, as follows.

$$(\rho u A \phi)_e - (\rho u A \phi)_w = \left(\Gamma A \frac{\mathrm{d}\phi}{\mathrm{d}x} \right)_e - \left(\Gamma A \frac{\mathrm{d}\phi}{\mathrm{d}x} \right)_w + \bar{S}_\phi \Delta V \tag{4.62}$$

Where

- the subscripts denote the face where the properties are evaluated;

- u is the velocity in the direction x $[m/s]$;

- A is a cross-section area of the control volume surface $[m^2]$;

- $\bar{S}_\phi$ is the average value of source over the control volume;

- ΔV is the volume $[m^3]$.

One may call the terms on left-hand side *advection* or *convection terms* and the terms on right-hand side (except for the source term) *diffusion terms*.

Applying steady state condition and the same integration procedures to continuity equation (4.1), the discretized continuity equation takes the form in Eq. (4.63).

$$(\rho u A)_e - (\rho u A)_w = 0 \tag{4.63}$$

One may assume that dynamic viscosity (μ, which plays the role of the diffusion coefficient Γ), density (ρ) and cross-section area (A) are constant and prescribed, which applies for the present

work. However, it is still necessary to determine the values of u, ϕ and $\dfrac{\mathrm{d}\phi}{\mathrm{d}x}$ at west (w) and east (e) faces. Therefore, different interpolation schemes are used for diffusive, advection, gradient and pressure terms.

Furthermore, when the property ϕ in Eq. (4.58) is replaced by velocity components (u, v and w), steady-state momentum equations are obtained. The pressure term in Eq. (4.2) appears in Eq. (4.58) as part of the source term. In fact, pressure gradient term "forms the main momentum source term in most flows of engineering importance" [3]. In the algebraic system formed by Eqs. (4.62) and (4.63), each velocity component has a transport equation associated to it and is also present in continuity equation terms. On the other hand, the pressure plays a complex role in such system of equations due to the absence of an equation for it.

In the following subsections the different approaches used by CFX and FLUENT for both interpolation and pressure-solving schemes are briefly commented.

4.3.3 CFX Discretization Schemes

For less robust turbulence models CFX provides three schemes for the interpolation of advection terms around nodal points. Upwind, high resolution and specified blend factor are available. Generally, CFX interpolates the properties as shown in Eq. (4.64) [78].

$$\phi_f = \phi_{up} + \beta\, grad\,\phi \cdot \Delta\vec{r} \tag{4.64}$$

Where

- ϕ_f is the value of property ϕ at a face;

- ϕ_{up} is the value of property ϕ at the upstream nodal point;

- β is a blend factor;

- $grad\,\phi$ is the gradient of property ϕ whose treatment depends on chosen scheme;

- $\vec{r}$ is the vector from the upstream (up) to the nodal point (np).

So, setting upwind scheme is equivalent to set $\beta = 0$ in Eq. (4.64). It means "the convected value of ϕ at a control volume face is taken to be equal to the value at the upstream node" [3]. Upwind is then a first-order accuracy scheme and, although simple and thus widely used, it typically causes numerical false diffusion [78, 3, 86].

The discretization errors associated with the first-order upwind scheme may be reduced by choosing values for β between 0 and 1. For $\beta = 1$ the accuracy reaches the second-order. Usually, increasing β implies improving accuracy. On the other hand, it also generates non-realistic solutions (local oscillations) due to being non-dissipative [78].

The high resolution method is similar to TVD (Total Variation Diminishing) schemes [3]. The main difference between high resolution and the other two options is that high resolution scheme tries to find the best blend factor β for each node, based on boundedness and accuracy principles [78]. For further information about these schemes and their peculiarities the reader is forwarded to references [3, 78, 86].

It is remarkable that turbulence equations in CFX are always interpolated with the first-order upwind advection scheme, irrespective of the advection scheme set for momentum equations. Also, diffusion, gradient and pressure terms use shape functions (finite-element-based) in order to interpolate properties [78].

In this dissertation, the influence of the advection scheme on CFX results has been briefly tested and is presented in Chapter 5.

4.3.4   FLUENT Discretization Schemes

FLUENT affords several options for each term that needs interpolation. Advection terms in any transport equation may be discretized with first- and second-order upwind, power law, QUICK, or third-order MUSCL schemes. Nevertheless, FLUENT does not offer a generalized formulation for its advection interpolations.

First- and second-order upwind are respectively identical to $\beta = 0$ and $\beta = 1$ cases on CFX discretization schemes.

Power law scheme uses the exact solution of the one-dimensional convection-diffusion equation

(Eq. (4.58) without the source term). It is generally more accurate for one-dimensional problems [3].

QUICK (Quadratic Upstream Interpolation for Convective Kinetics)-type schemes blend second-order upwind and second-order central schemes, and is available for structured (quadrilateral and hexahedral) meshes only. Such scheme is typically more accurate when mesh is aligned with the flow direction [79].

Third-order MUSCL (Monotone Upstream-Centerd Schemes for Conservation Laws) scheme blends central and second-order upwind schemes. This scheme usually reduces numerical diffusion, mainly in complex three-dimensional flows, presenting better results when compared to the second-order upwind scheme [79].

Power law, QUICK and third-order MUSCL schemes have not been considered in this dissertation. There are other discretization options in FLUENT, but depending on other choices, such as the turbulence model. The reader is forwarded to the reading of references [3, 79, 86] for more information on discretization schemes available in FLUENT.

Gradient terms may receive three different evaluations: Green-Gauss (cell- and node-based) and least squares cell-based. In FLUENT solver, least squares cell-based method is the default gradient method because it is less expensive [79]. The other options have not been checked in this work and their influence is left as a further work suggestion.

Standard pressure interpolation for pressure terms is the default. Although, other schemes are available: PRESTO!, linear, second-order and body force weighted. Standard scheme interpolates the pressure values at elements faces using balanced pressures of neighbouring nodes. FLUENT user's guide [87] does not recommend this scheme for flows generating high pressure gradient at the cell face. For swirl flows, for instance, PRESTO! scheme is suggested. However, in this dissertation the default (standard) scheme has been utilised for all tested cases. The sensitiveness test for pressure interpolation schemes is suggest as future work as well.

4.3.5 Pressure-Velocity Algorithms

As commented in the end of subsection 4.3.2, because pressure and velocity fields must satisfy both momentum and continuity equation, the absence of an equation for the pressure is considered a problem.

One of the propositions to overcome such issue is the SIMPLE (Semi-Implicit Method for Pressure Linked Equations) algorithm [88]. This method essentially starts by guessing a pressure field and solving discretized momentum equation. Then, a pressure correction is calculated aided by a manipulated continuity equation. Pressure and velocities are adjusted, and discretized transport equations are solved again. If convergence is achieved, the algorithm stops, if not, it restarts with adjusted values instead of guessed values.

FLUENT offers SIMPLE, SIMPLEC, PISO and coupled algorithms for pressure-velocity coupling. SIMPLEC and PISO may be considered SIMPLE variations. Briefly, both SIMPLEC and PISO follow the operations of SIMPLE algorithm, but the manipulation of the momentum equations is different for SIMPLEC and a further corrector step is added for PISO. [3]

In coupled scheme, momentum and pressure-based continuity equations are solved simultaneously. Different discretization techniques for pressure gradient and mass flux are necessary, and the resulting discretized system may be put together into a single matrix equation. [79]

In this work, all FLUENT runs have been performed preferably with SIMPLE algorithm. Although, in some cases (see Chapter 5), coupled scheme have been necessary in order to reach the established convergence criteria (see section 4.3.6.2). On the other hand, CFX is restricted to coupled algorithm. Once again the influence of distinct pressure-velocity coupling algorithm is left as a suggestion for future work.

Variables storage location is an important issue in CFD simulations. Usually, the available options are co-located or staggered grid. Co-located grid stores properties values at control volumes center, *i.e.*, at nodal points. On the other hand, staggered grid stores part of the variables (mostly pressure) at element center (nodes) and the other part at element faces (mostly velocities) [3, 86]. Both CFX and FLUENT use the co-located grid arrangement.

4.3.6 Algebraic System Solution

The equations used for the solution of flow field, turbulence and pressure field are initially differential equations. The finite volume method proposes the linearization of such equations in order to obtain a linear algebraic system.

Regardless of chosen schemes, the transport equation of a variable ϕ (Eq. (4.62), for instance) may be written in terms of the variable value at each node and a numerical coefficient associated to it, as show in Eq. (4.65).

$$a_P \phi_P = \Sigma_{nb} a_{nb} \phi_{nb} + b \tag{4.65}$$

Where

- a_P is the coefficient for a node P;

- ϕ_P is the value of ϕ at node P;

- $\Sigma_{nb} a_{nb} \phi_{nb}$ represents the influence of all neighbouring (subscript nb) nodes;

- b is the contribution of source term and boundary conditions.

Thus, since the complete algebraic system of equations representing all nodes is linear, it may be expressed in general matrix form, as show in Eq. (4.66). Detailed manipulation steps can be found in references [3, 86, 89].

$$[A] [\phi] = [b] \tag{4.66}$$

Where

- $[A]$ represents the coefficient matrix;

- $[\phi]$ represents the unknowns or solution vector;

- $[b]$ represents the right-hand side vector, which usually contains terms related to boundary conditions and source terms as well.

There are two available approaches in order to solve the linear algebraic equations: direct methods and indirect, implicit or iterative methods [3]. Direct matrix inversion is impractical due to core memory limitations when storing necessary coefficients for usual CFD problems. Since iterative methods are generally more economic for fine meshes, they are widely used in CFD codes [3].

Iterative methods usually start from a guessed solution for each unknown and tends to a better solution by several iterations until a desired convergence criteria is achieved. Jacobi, Gauss-Seidel, Conjugate Gradient (CG), Lower Upper (LU) and Incomplete Lower Upper (ILU) are some examples of iterative methods [3, 90].

Generally speaking, the convergence rate of iterative methods reduces as the mesh is refined [3]. On the other hand, finer meshes are usually desired aiming better results. It is now important to present the idea of wavelengths associated with error propagation throughout the domain. It is believed that "the solution error has components with a range of wavelengths that are multiples of the mesh size" [3]. Thus, the longest possible wavelengths are of the order of the domain size and the shortest are of the order of the mesh size. Iterative methods rapidly reduce short-wavelength error components. Nevertheless, long-wavelength error components tend to decay slowly causing inherent slow convergence rates. Because coarser meshes provide narrower ranges of wavelengths, their convergence is faster [3]. Maliska [86] proposes an interesting exercise (ex. 3.18 - chapter 3) aiming better comprehension and observation of convergence rate sensitivity due to mesh sizing.

In order to reach higher convergence rates even in finer meshes, modern CFD codes usually work with an acceleration technique called *Multigrid*. This technique allows combining fine meshes and faster convergence rates of coarser meshes by cycling iterations on different mesh sizes, as illustrated in Fig. 4.2. With Multigrid acceleration, short-wavelengths are reduced on fine meshes, whereas coarse meshes are responsible for improving convergence rate for long-wavelengths. References [3, 86] contain further information about the Multigrid technique.

CFX uses Multigrid accelerated ILU factorization technique for solving the discrete system of algebraic equations. On the other hand, FLUENT provides Gauss-Seidel and ILU methods, both aided by Multigrid technique as well. Gauss-Seidel is the default for SIMPLE algorithm and, for coupled scheme, ILU is the default method for coupled parameters ($\bar{u}$, $\bar{v}$, $\bar{w}$ and $\bar{p}$) and Gauss-Seidel is kept for scalar parameters (k and ε). Regarding solution methods, all runs have
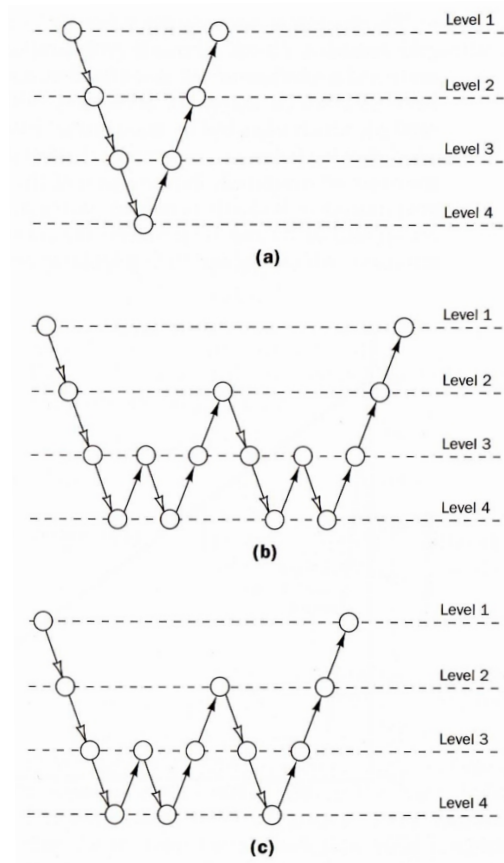
Figure 4.2. Illustration of usual multigrid cycles: (a) V-cycle; (b)W-cycle; (c) F-cycle. [3]

been performed in default conditions in the present work and the main control parameters are presented in the following subsections.

4.3.6.1   Control Parameters

Some solution control parameters are necessary for better and smoother convergence. Under-relaxation factors are commonly used in order to avoid divergence [3]. They control the change in a variable ϕ, as shown in Eq. (4.67).

$$\phi = \phi^* + \alpha\Delta\phi \qquad (4.67)$$

Where

- ϕ^* is the old value of ϕ;

- α is the under-relaxation factor;

- $\Delta\phi$ is the computed change in ϕ;

Under-relaxation factors (α) usually assume values between 0 and 1, playing an important role in controlling convergence. CFX default under-relaxation factor is 0.9 for every flow-related ($\bar{u}$, $\bar{v}$, $\bar{w}$ and $\bar{p}$) or extra (k and ε) variable. FLUENT have different default under-relaxation factors for pressure, momentum and turbulence variables. Respectively, their values are 0.3, 0.7 and 0.8 for SIMPLE scheme, and 0.75, 0.75 and 0.8 for Coupled scheme.

Multigrid technique also involves several choices and parameters with respect to its cycles. CFX documentation does not provide explicit information about the cycles. It is presented that the default option for algebraic Multigrid consists in "anisotropic coarsening [which] is designed to give robust convergence for the widest possible range of flow conditions" [91]. FLUENT, on the other hand, offers several types of cycle and its respective parameters, such as maximum number of cycles and coarsening factor. For SIMPLE scheme, V-cycle for pressure and flexible cycle for momentum and turbulence are the default parameters. For coupled scheme, F-cycle for coupled velocity and pressure, and flexible cycle for turbulence is the default condition.

With regard to under-relaxation factors and Multigrid technique, all parameters have been kept in default option [87, 91] in this dissertation.

4.3.6.2   Convergence Criteria

For both CFX and FLUENT, the solution may terminate normally when one of the following situations is achieved: maximum iteration number or convergence criteria. Generally, the last one is desired and thus, it is now briefly discussed.

Convergence is monitored by residual values of each equation, which are observed at the end of every iteration. Both solvers used in the present work define residual similarly and their peculiarity are commented in the following.

CFX defines residual in the n-th iteration as given by Eq. (4.68):

$$r_\phi^n = b - A\phi^n \tag{4.68}$$

Where

- r_ϕ^n is the residual value in the n-th iteration;

- ϕ^n is the solution vector in the n-th iteration.

It is remarkable that Eq. (4.68) is the imbalance in Eq. (4.66). However, because residual are usually normalized for solution monitoring, r_ϕ is called *raw residual*. In CFX, *normalized residual* ($\tilde{r}_\phi$) is given by the following relation:

$$\tilde{r}_\phi = \frac{r_\phi}{a_P \Delta \phi} \tag{4.69}$$

Where

- r_ϕ is the raw residual value obtained by Eq. (4.68);

- a_P represents the control volume coefficient;

- $\Delta \phi$ represents the range of the variable in the domain.

Unfortunately, CFX documentation omits the calculation of a_P and $\Delta \phi$ claiming it is a complex procedure. Notwithstanding, there are two possible normalization procedures: *maximum residuals*, which are based in the maximum residual value over the entire domain, and *RMS residuals*, which is the RMS (Root Mean Square) of all residual values over the domain.

In all CFX simulations in this dissertation, the RMS residuals of discrete equations for coupled variables (*i.e.*, $\bar{u}$, $\bar{v}$, $\bar{w}$ and $\bar{p}$) have been controlled to be smaller than 1×10^{-8} with double precision.

Regarding residual treatment, FLUENT presents similar approach. Although, instead of defining residuals as the imbalance in Eq. (4.66), FLUENT makes use of Eq. (4.65), as follows.

$$r_\phi = \Sigma_{cellsP} |\Sigma_{nb} a_{nb} \phi_{nb} + b - a_P \phi_P| \tag{4.70}$$

Where the subscript $cellsP$ indicates the summation over all cells P.

Once again a normalization procedure is carried out and FLUENT provides two possibilities:

globally scaled residuals, which considers the average value over the domain, and *locally scaled residuals*, which is the RMS residual associated to maximum and minimum values of the variable ϕ over the domain. Since global normalization is the default and the one used in the present work, it is now presented in Eq. (4.71).

$$\tilde{r}_\phi = \frac{r_\phi}{\Sigma_{cellsP}|a_P\phi_P|} \tag{4.71}$$

In this dissertation, all FLUENT simulations have been controlled to give globally scaled residuals smaller than 1×10^{-8} for all variables with double precision.

4.4 Simulating an Ultrasonic Flow Meter: Calculation of the Correction Factor

It is commented in Chapter 2 that the proposition given by AGA 9 [31], which is also used by the Brazilian regulation [17], leads to neglecting the contribution of $\bar{v}$ and $\bar{w}$. Such approach is able to account profile asymmetries, but swirl effects may not affect the calculation of the correction factor. Since installation effects are defined and the presence of tangential velocities are presented as their main feature in Chapter 3, it is important to evaluate the behaviour of correction factors under disturbed flow condition, taking into account the influence of tangential velocities.

Before any mathematical treatment, it is important to remark the assumptions to the approach carried out in this dissertation. In fact, acoustic path is complex, since it depends on acoustics and its interaction with the flow field, as already commented in Chapter 3. However, linear and non-deformable acoustic path has been considered, and such assumption is reasonable according to Yeh and Mattingly [29]. Moreover, velocity fluctuations due to turbulence occur in real flows which also influence the acoustic path and therefore the flow rate [33]. Nevertheless, due to the choice of RANS turbulence models, the present work only considers the time-averaged flow. Reasonable treatment for the relations between the acoustic path and the flow field is suggested for future work (refer to Sec. 8.3).

In the following, it is presented a numerical procedure to calculate the factor k aiming to esti-

mate deviations on ultrasonic flow measurements under disturbed conditions. This numerical approach for simulating ultrasonic flow meters is used by different authors [4, 12, 21, 59]. Such technique considers tangential velocities on the flow field over the acoustic path and proceed with numerical integration to obtain $\bar{V}_{UFM}$.

Back to the general formulation for the correction factor given by Eq. (2.15), it is necessary to estimate a disturbed correction factor by means of CFD results. The mean flow velocity ($\bar{u}_m$) is obtained by means of the desired Reynolds number, as shown in Eq. (4.16).

Regarding $\bar{V}_{UFM}$, contribution of $\bar{V}_{AP}$ has been calculated by applying the Trapeze Rule [90] in order to solve the integrals in Eq. (2.16). General formulation for numerical integration of $\bar{V}_{UFM}$ gets the form represented in Eq. (4.72).

$$\bar{V}_{UFMnum} = \frac{\bar{V}_{APnum}}{\cos \alpha} = \frac{1}{L_{AP}} \sum_{p=2}^{N+1} \left[\frac{(\bar{u}_p + \bar{u}_{p-1})}{2} \right.$$
$$+ \frac{(\bar{v}_p + \bar{v}_{p-1})}{2} \tan \alpha \cos \theta \tag{4.72}$$
$$\left. + \frac{(\bar{w}_p + \bar{w}_{p-1})}{2} \tan \alpha \sin \theta \right] \Delta L_{AP}$$

Where

- N is the number of integration points;

- the subscript p indicates the value of a velocity component at the p-th integration point;

- ΔL_{AP} is given by $L_{APp} - L_{APp-1}$.

It is known that the number of integration points (N) influences the results and a sensitivity test is presented in Chapter 5.

The numerical factor k is finally obtained by substituting Eqs. (4.16) and (4.72) in Eq. (2.13), yielding Eq. (4.73).

$$k_{num} = \frac{L_{AP} \mu Re}{\rho D \sum_{p=2}^{N+1} \left[\frac{(\bar{u}_p + \bar{u}_{p-1})}{2} + \frac{(\bar{v}_p + \bar{v}_{p-1})}{2} \tan \alpha \cos \theta + \frac{(\bar{w}_p + \bar{w}_{p-1})}{2} \tan \alpha \sin \theta \right] \Delta L_{AP}} \tag{4.73}$$

4.4.1 Defining Factor k Deviation

Since the factor k is directly related to the flow rate calculation, it is important to quantify its deviation due to disturbances. Many authors [4, 63, 92] have evaluated this deviation (Δk) as follows in Eq. (4.74).

$$\Delta k = 100\% \frac{k_{dist} - k_{ref}}{k_{ref}} \tag{4.74}$$

Where

- Δk is the factor k deviation (%);

- k_{dist} is the numerical factor k calculated for a disturbed profile;

- k_{ref} is the reference factor k.

In this dissertation two references have been considered. First one is given by Eq. (2.19), which represents the results considering the semi-empirical profile of [34]. This relation is suggested by both editions of AGA 9 [15, 31] and by the Brazilian regulation [17] as the fully developed turbulent profile. The other reference is obtained with the present results by numerical integration of Eq. (4.73) for a straight pipe. Numerical factor k at a fully developed section, *i.e.* $80D$ downstream from the entrance, has been calculated for several Reynolds numbers. The results are shown in Chapter 7.

4.5 Brief Remarks on Numerical Error and Uncertainty

Versteeg and Malalasekera [3] report the importance of recognising and quantifying errors and uncertainties on CFD modelling. In this context, the authors suggest two steps: *verification* and *validation*. Verification involves errors whereas validation involves uncertainties. According to them, main aspects of verification are *round-off error*, *iterative convergence error* and *discretization error*. Section 4.3 provides information on round-off and iterative convergence errors. Round-off error is imposed by machine accuracy which has been set to *double precision* in all simulated cases. Iterative convergence error is given by the convergence criteria which

has been set to 10^{-8} in all simulations. Discretization errors are consequence of interpolation schemes (Sec. 4.3) and are better commented in Chapter 5. Validation procedures are conducted in Chapter 6.

4.6   Computational Facility

All runs have been performed by the 8 machines cluster at *Laboratório de Fenômenos de Transporte Computacional* (LFTC) of *Universidade Federal do Espírito Santo* (Ufes). Each PC is equipped with Quad Core processor 2.4 GHz, 4.0 GB memory and 8 MB cache, totalling 32 processing cores running on Linux platform.

Chapter 5

Simulation Parameters and Sensitivity Tests

Chapter 4 shows the need of performing certain tests in order to investigate the influence of some mathematical and numerical parameters. This chapter present simulated geometries and meshes as well as sensitivity tests for some parameters such as outlet location and boundary conditions.

5.1   Presentation of Simulated Cases

In the present work four cases have been considered, from which one is the validation of the model by comparing simulations with measured profiles from Hilgenstock and Ernst work [4]. The other three cases are related to the investigation on the influence of disturbed profiles on the simulated correction factor of ultrasonic flow meters. In this sense, a straight pipe flow has been simulated as a reference for fully developed condition. Single and double elbow out-of-plane have also been considered.

A double elbow out-of-plane as proposed by Hilgenstock and Ernst [4] has been considered for validation. Hilgenstock and Ernst's experimental apparatus contains in fact a 2D long pipe inlet, but LDA flow data taken at 1.2D is used as inlet conditions for simulations. Thus, geometry consists of a 1.2D long straight inlet pipe upstream from the first elbow, two coupled elbows

(*i.e.*, no straight pipe section between them) with mean curvature radius of 1.5D, and a 10D long straight exit pipe downstream from the second elbow. The analysed section is placed 5D downstream from the second elbow. Internal diameter is 200 mm and Fig. 5.1 shows the configuration.
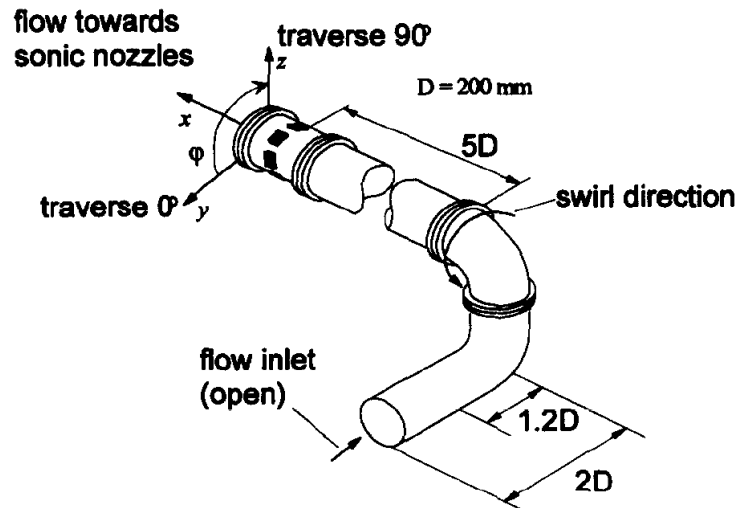
Figure 5.1. Geometry configuration for validation case. [4]

For the cases simulating the correction factor, pipe diameter is 300 mm and curvature radius is 1.5D. A 100D long straight pipe is considered for fully developed reference, as shown in Fig. 5.2. Then, single and double elbow configurations are arranged upstream from such straight pipe section. For both single and double elbow a 2D long straight inlet pipe is considered, and particularly for double elbow case a 2D long straight pipe section is placed between the two curves. Figures 5.3 and 5.4 show single and double elbow configurations, respectively.
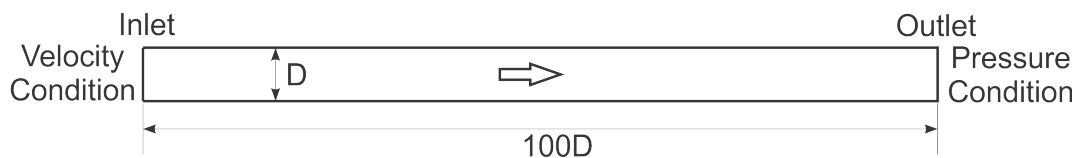
Figure 5.2. Straight pipe configuration.

5.2   Mesh Generation and Sensitivity Test

The previous chapter shows the Finite Volume Method approach, which involves dividing the domain into several control volumes where linearized equations are solved. In fact, interpo-
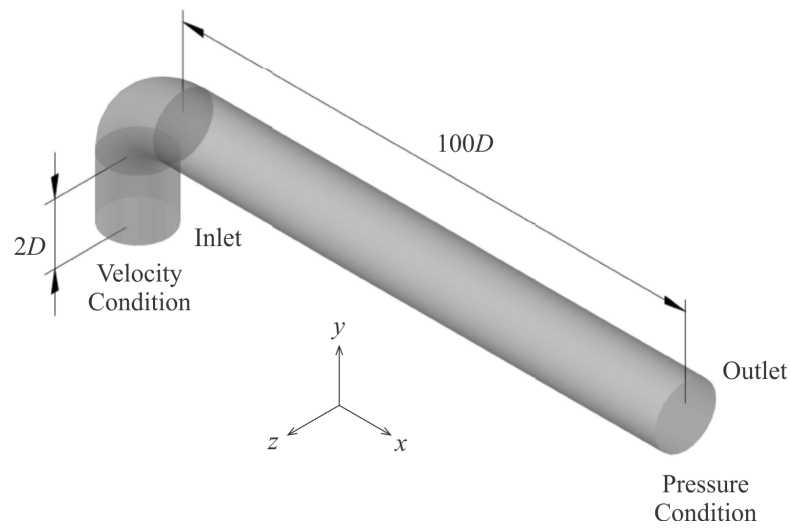
Figure 5.3. Single elbow configuration.
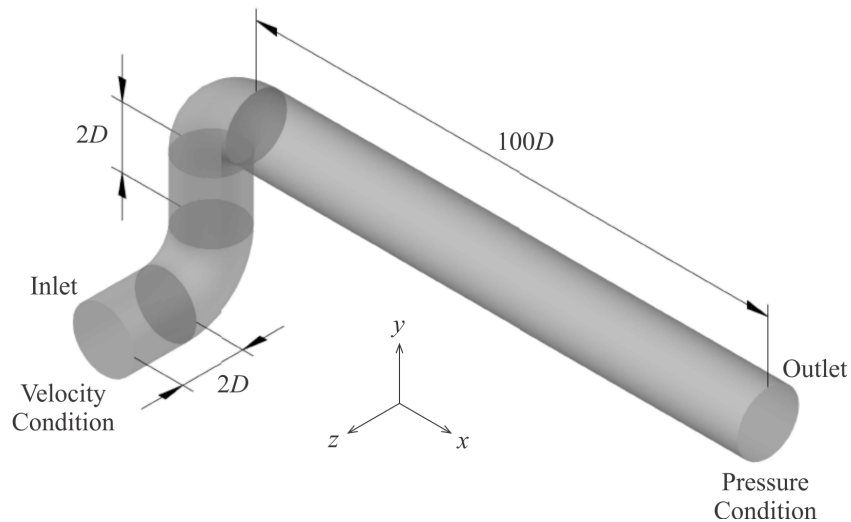
Figure 5.4. Double elbow configuration.

lations are used to transform differential equation in linear equation. Generally speaking, the smaller the control volumes, the fairer the interpolations are. Since control volumes sizes are dictated by the mesh, it is important to know how it influences the results. Such influence is the so called discretization error, introduced in Sec. 4.5. The analysis of discretization errors is made by means of mesh sensitivity tests.

The goal of mesh sensitivity tests is to demonstrate the reduction of discretization errors for quantities of interest by comparing the results for different levels of mesh refinement. In this dissertation, mesh refinements have been controlled by the number of nodes (nodal points).

Successive meshes have been generated aiming to duplicate the amount of nodes. Because velocity profiles are crucial in the calculation of the correction factor, they have been chosen to be the analysed parameter.

It is now important to describe the technique used to mesh generation. All meshes used in this dissertation are structured and hexahedral. Meshes have been generated in ANSYS ICEM CFD [93] with multi-block technique [3]. Such technique generally provides flexibility and better mesh accommodation for curved boundaries [3]. Since double elbow is the most complex geometry considered in the present work, its mesh generation procedure and mesh sensitivity test are briefly presented as an example. Complete mesh sensitivity test results for all cases are available in Appendix A.

Figure 5.5 shows blocks arrangement for a double elbow geometry. The basic concept is to create a core with squared cross-section in which it is possible to control the number of divisions in its vertical and horizontal edges (black lines at inlet plane in the bottom of Fig. 5.5a). This square core is associated with an offset inscribed square in pipe diameter (green lines at inlet plane in the bottom of Fig. 5.5a). Core and inscribed squares are associated by diagonal edges, in which is also possible to control the number of divisions. As can be seen in Fig. 5.5b, every cross-sectional plane is organized by five blocks. A resulting mesh is shown in Fig. 5.6.

(a) Block edges. (b) Block faces.
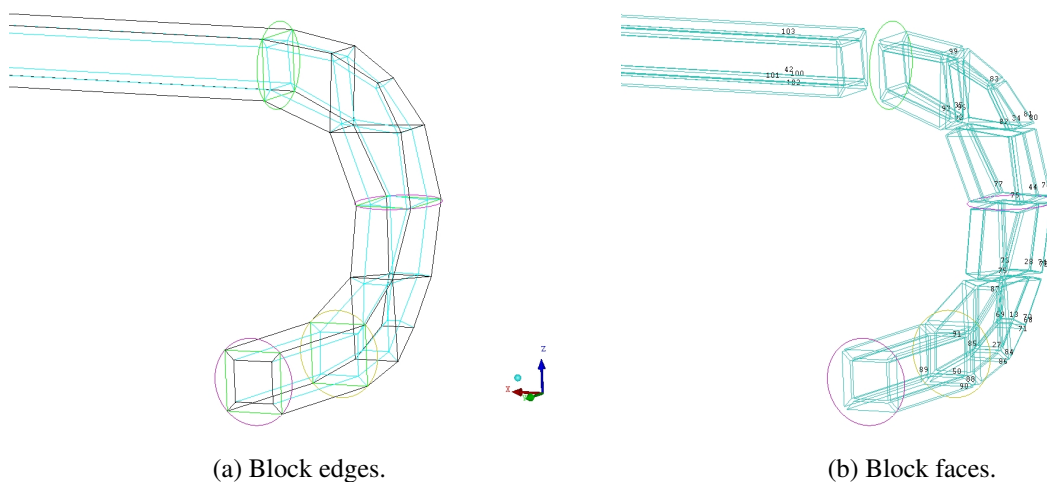
Figure 5.5. Block structures for double elbow mesh generation.

Although it is possible to control the number of edge division, maximum element size and the height of the first element normal to surfaces or curves have been controlled to generate finer meshes. These two parameters have been modified (decreased) aiming to produce successive
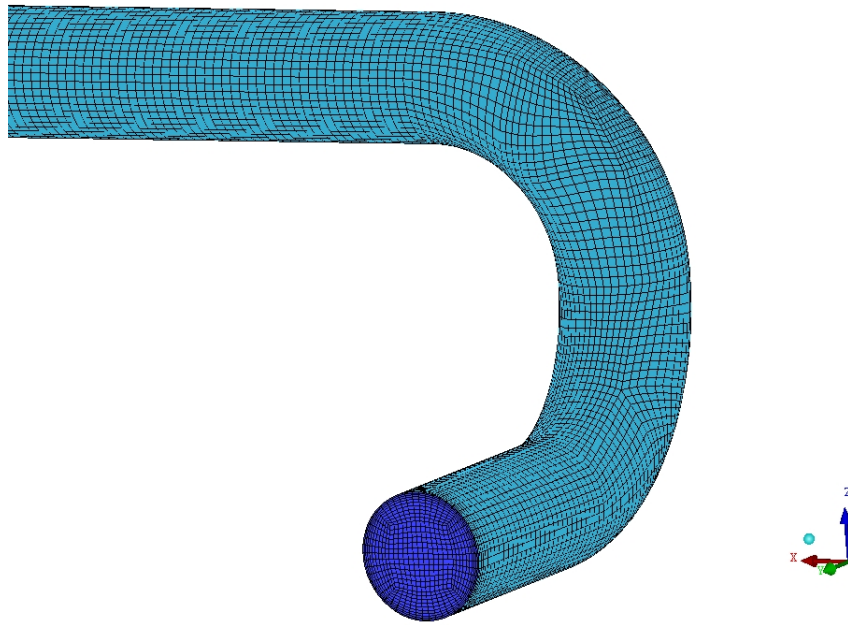
Figure 5.6. Example of mesh generated with multi-block technique.

meshes with double nodes number. Also, since wall refinement is desirable in order to capture wall effects, an expansion ratio is used for controlling the growth rate of elements from the surface to pipe center. Such expansion factor has been set to 1.2 for all generated meshes.

Table 5.1 summarizes the main parameters for the single elbow case and Fig. 5.7 shows the resulting meshes, represented at the inlet plane.

Table 5.1. Mesh parameters for single elbow case.

Mesh	Nodes	Maximum Size [mm]	Height [mm]
1	7×10^4	60	20
2	1.4×10^5	43	16
3	2.9×10^5	32	12
4	6.2×10^5	24.5	9
5	1.27×10^6	19	5
6	2.42×10^6	15.6	2
7	4.76×10^6	12.9	0.8
8	9.47×10^6	10.3	0.4

Figure 5.8 displays mesh test results for FLUENT single elbow runs. During the mesh sensitiv-
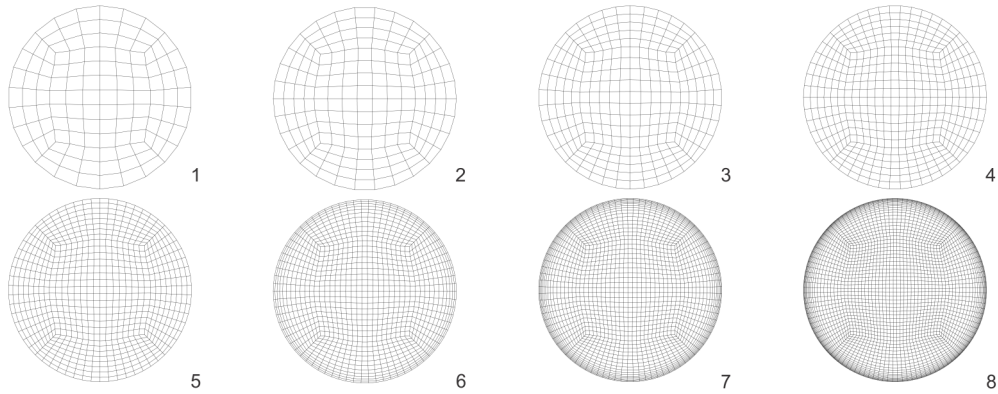
Figure 5.7. Meshes at inlet plane for single elbow case.

ity test of single elbow case Reynolds number has been kept in 2×10^6, since it is the highest Re considered in the present work and thus it tends to be more difficult to achieve convergence. Figure 5.8a shows $\bar{u}$ velocity at pipe center along the straight section downstream from the elbow for all tested meshes. Figures 5.8b to 5.8d present velocity components ($\bar{u}$, $\bar{v}$ and $\bar{w}$) along y-axis at $x = 20D$ (downstream from the elbow) under disturbed conditions. The choice for such axis and position has been motivated by the possibility of evaluating a disturbed section.

Overall results show an asymptotic trend. Figures 5.8a and 5.8b suggest that results for mesh 7 already reproduce results for mesh 8. It is important to remark that $\bar{u}$-velocity component (Fig. 5.8b) represents the greatest contribution on factor k calculation, so it is the most influencing quantity. Figure 5.8c also shows good agreement between the results for meshes 7 and 8. The magnitude of velocities in Fig. 5.8d is significantly smaller, but results seem to tend to zero. Regarding the analysis of Fig. 5.8 above, mesh 7 has been chosen to run all single elbow cases in this work.

Same methodology has been applied to validation case, straight pipe and double elbow cases. Tables and graphics related to mesh test results for other simulated cases are gathered in Appendix A.

5.3   Boundary Conditions Sensitivity

Since it has been found a mesh which does not influence the results, it is necessary to investigate other influencing parameters. It is reported in Chapter 4 that boundary conditions for momen-

(a) Non-dimensional $\bar{u}$ velocity along pipe center

(b) Non-dimensional $\bar{u}$ velocity at $20D$ for $\theta = 0°$.

(c) Non-dimensional $\bar{v}$ velocity at $20D$ for $\theta = 0°$.

(d) Non-dimensional $\bar{w}$ velocity at $20D$ for $\theta = 0°$.
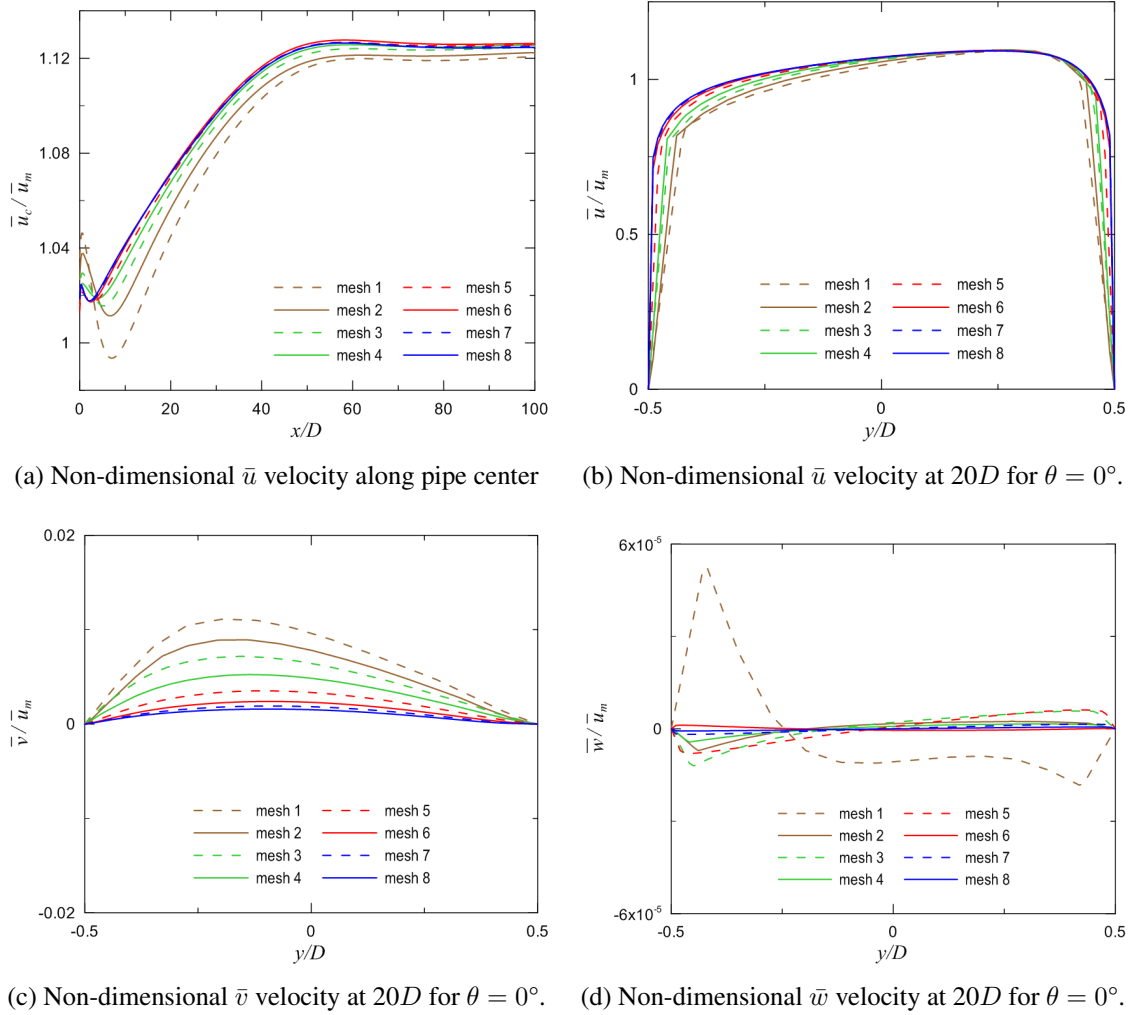
Figure 5.8. Mesh test results for single elbow.

tum and turbulent transport equations are needed. Some of them are imposed by the code and other are input parameters.

Inlet boundary conditions are defined by velocity and turbulence specifications. Except for validation case, uniform velocity profile is assumed. On the other hand, turbulence quantities have to be defined. When adequate experimental facilities are available, it is possible to measure or at least infer such quantities. However, since no measured data is available for the particular case of flare gas flows, some assumptions have been made. Such assumptions are better justified in Chapter 7 and for now it is important to show the influence of different choices.

It is shown in Sec. 4.2 that boundary values for turbulence quantities (k and ε) are usually estimated as a function of other turbulence parameters, such as turbulence intensity (I). Figure 5.9

depicts a preliminary test for the influence of different predefined turbulence intensities at inlet for double elbow case on CFX with $Re = 1 \times 10^5$. Predefined turbulence intensities considered are: 1% (low), 5% (medium) and 10% (high).

(a) Non-dimensional $\bar{u}$ velocity along pipe center.

(b) Non-dimensional $\bar{u}$ velocity at 20D for $\theta = 0°$.

(c) Non-dimensional $\bar{v}$ velocity at 20D for $\theta = 0°$.

(d) Non-dimensional $\bar{w}$ velocity at 20D for $\theta = 0°$.
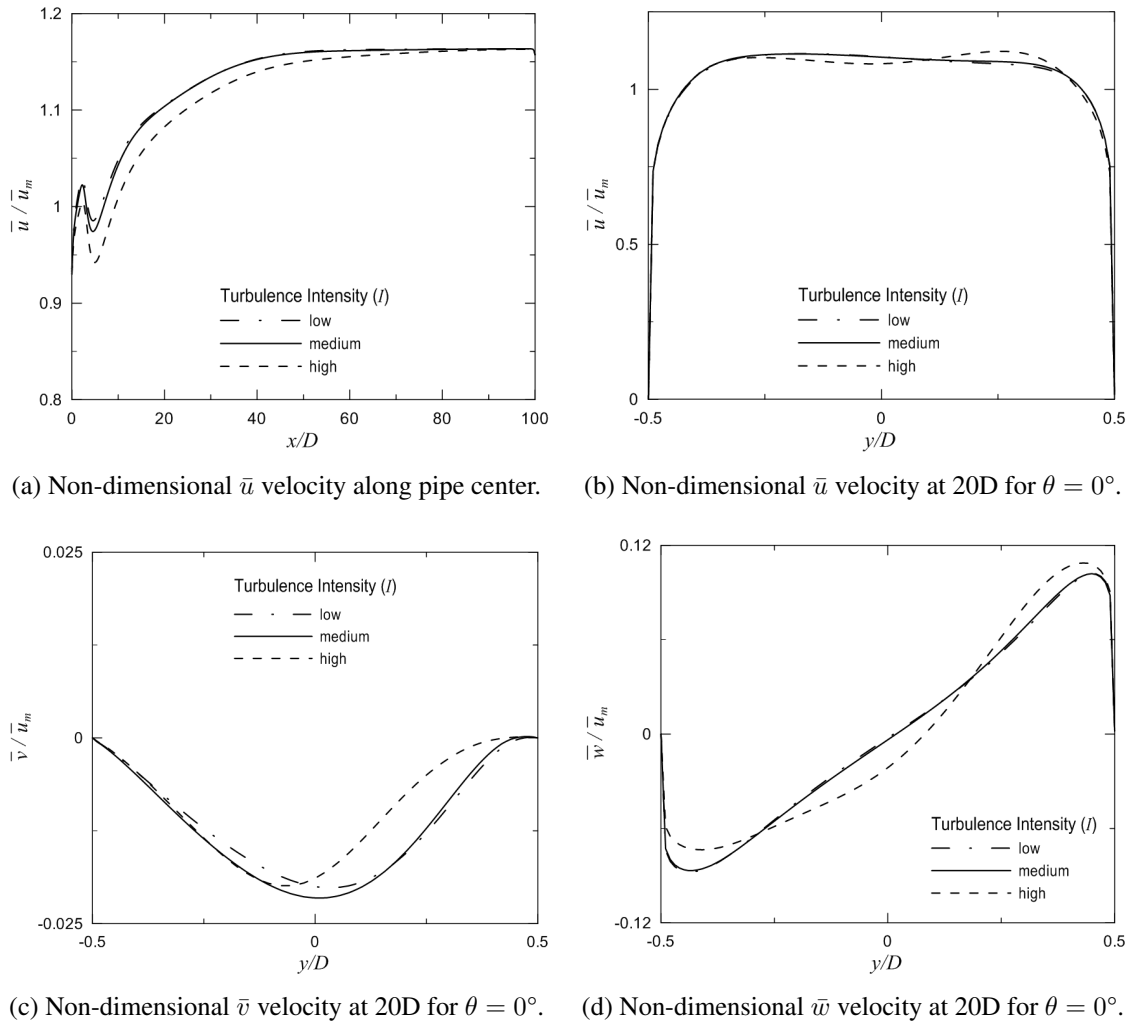
Figure 5.9. Influence of inlet turbulence intensity (I) on CFX results for double elbow case: low (1%), medium (5%) and high (10%) turbulence intensity. ($Re = 1 \times 10^5$)

It is remarkable that low and medium turbulence intensities achieve very similar results for all velocity components and, on the other hand, high turbulence intensity (10%) results stand out by some differences. Although being relevant or not depends on the context, such differences are relatively small given that typical values for inlet turbulence intensity are usually between 1% and 6% [3].

5.4   Advection Scheme Sensitivity

Several advection interpolation schemes are commented in Sec. 4.3. CFX's high resolution and first-order upwind schemes have been compared for the double elbow case with $Re = 1 \times 10^5$ and the results are shown in Fig. 5.10.

(a) Non-dimensional $\bar{u}$ velocity at pipe center.

(b) Non-dimensional $\bar{u}$ velocity at 20D for $\theta = 0°$.

(c) Non-dimensional $\bar{v}$ velocity at 20D for $\theta = 0°$.

(d) Non-dimensional $\bar{w}$ velocity at 20D for $\theta = 0°$.
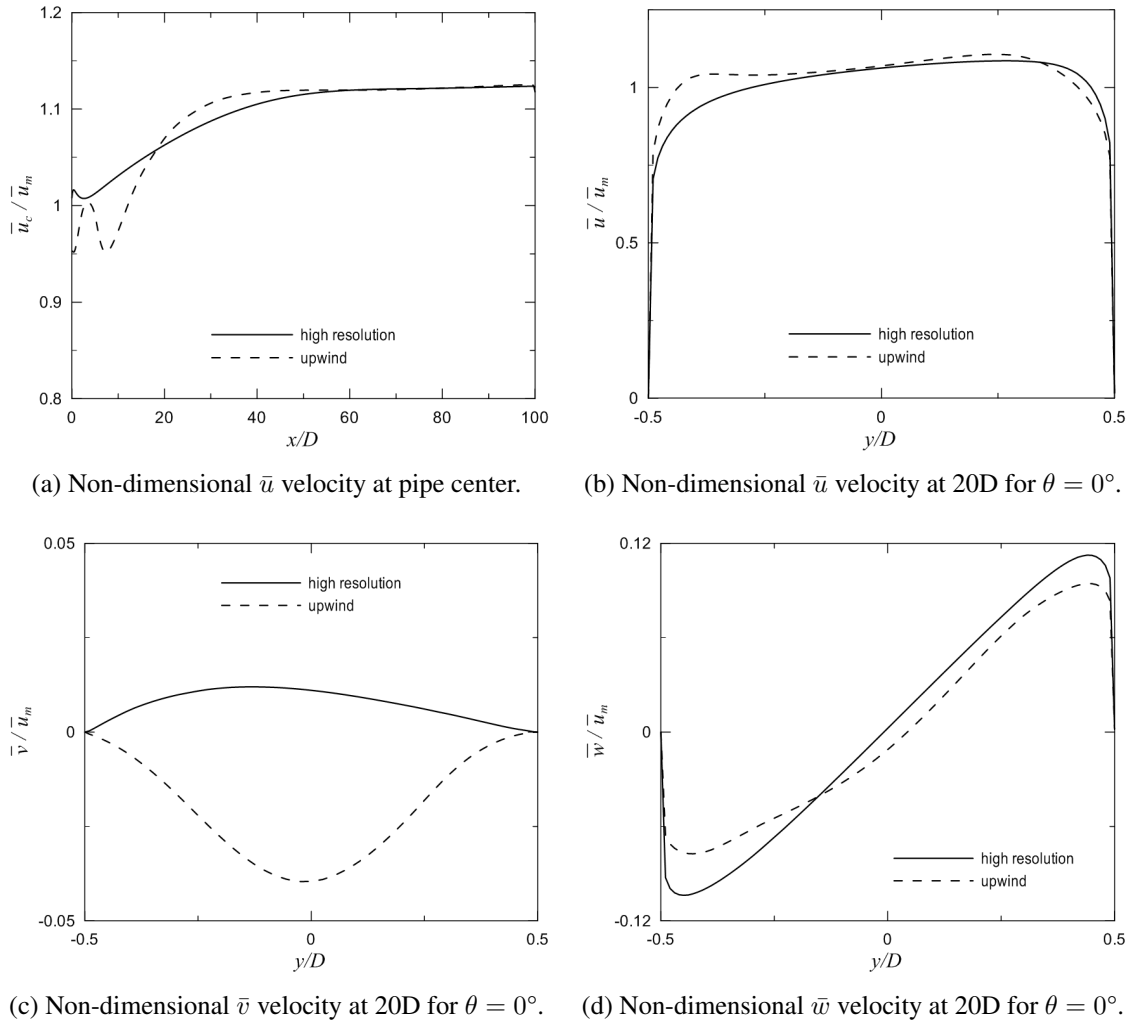
Figure 5.10. Influence of the advection scheme on CFX results for double elbow case. ($Re = 2 \times 10^6$)

Results seem to be reasonably sensitive to advection schemes. Figure 5.10a suggests that flow field is quite distinct and such behaviour may be confirmed by analysing Fig. 5.10c which shows opposite tendencies in vertical (y-axis) direction. Swirl direction, which is given by $\bar{w}$ at this angular position ($\theta = 0°$), is the same for both schemes. Nevertheless, high resolution scheme leads to a bit more intense swirl, as noticed in Fig. 5.10d.

In fact, this advection scheme test does not aim to conclude which one is the best, but to show the relative magnitude of such differences. Default advection schemes for CFX and FLUENT (high resolution and first-order upwind, respectively) have been set to all simulations. More detailed investigation on the influence of advection schemes are suggest for future work.

5.5   Geometrical Sensitivity

The importance of performing a sensitivity study for the location of the outlet section is commented in the end of Sec. 4.2. In this particular case, the 100D long straight section downstream from the curves have been tested against a 200D long straight pipe section. Since the mesh for the 200D case has achieved more than 10 million nodes and preliminary tests (with coarser meshes) suggest that swirl effects are still relevant even 200D after the curves for $Re = 2 \times 10^6$, laminar flow have been considered for $Re = 6 \times 10^2$.

Figure 5.11 depicts velocity components and pressure gradient along the center of straight pipe sections of 100 and 200D placed downstream from the curves. Results suggest that differences between both velocity and pressure fields calculated for the two cases (100 and 200D) are negligible, graphically speaking. Such similarity is probably related to small gradients for velocity components in the flow direction.

It is important to remark that the same velocity profiles have been found at 100D, as shown in Fig. 5.12. In Figure 5.12c, one may noticed that swirl effects still occur even after 100D, although such effects vanishes after 200D (Fig. 5.13), since non-dimensional radial and tangential velocities (Figs. 5.13b and 5.13c) reach the same magnitude of convergence criteria.

5.6   Sampling Sensitivity on Numerical Integration

According to Ferreira [92], sampling errors for the calculation of $\bar{V}_{AP}$ lower than 0.02% are reasonable and should not compromise the quality of numerical integration. A sampling sensitivity study have been carried out in order to ensure adequate number of integration points.

The test consists in calculate the numerical factor using different number of integration points

(a) Non-dimensional u velocity along pipe center.

(b) Non-dimensional v velocity along pipe center.

(c) Non-dimensional w velocity along pipe center.

(d) Pressure gradient along pipe center.
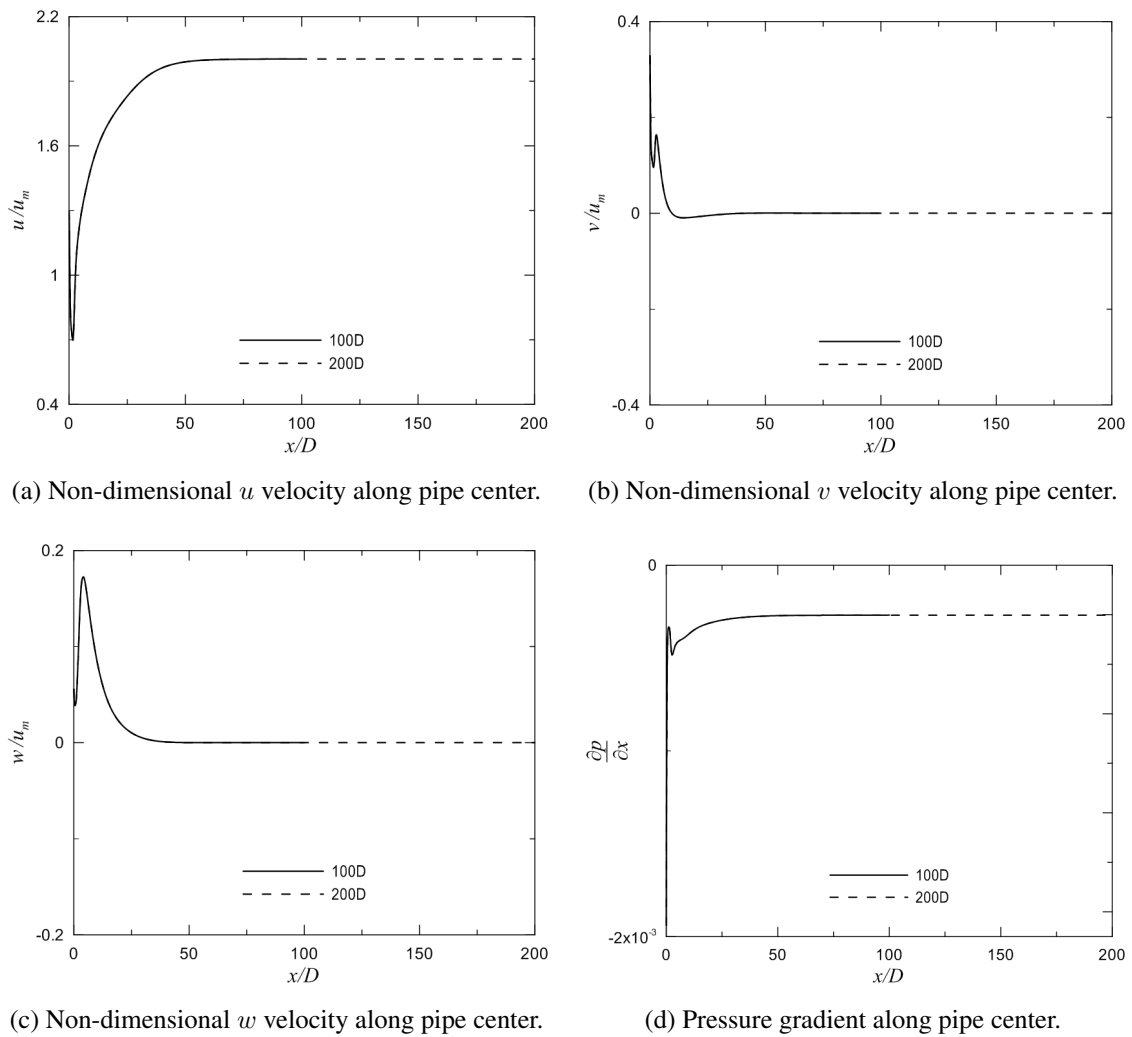
Figure 5.11. Influence of outlet location on CFX results along pipe center for double elbow case. ($Re = 6 \times 10^2$)

and analyse the deviation associated to it compared to a reference. In this case, the reference value is the analytical solution of Eq. (2.19) for given Reynolds number (for Eq. (2.20) to be solved). This equation is derived with Nikuradse [34] profile, which is given by Eq. (2.18). The numerical factor k is calculated applying Eq. (4.73) to the same Nikuradse profile. It is important to remark that fully developed flow condition is assumed, so that the integral over the acoustic path (L_{AP}) in Eq. (2.19) may be replaced by an integral over D. The number of integration points is represented by N in Eq. (4.73).

Extreme lower and upper values for Reynolds number have been tested, *i.e.* 1×10^4 and 2×10^6. Four different samples have been considered: 251, 501, 1001 and 2001 integration points (N).
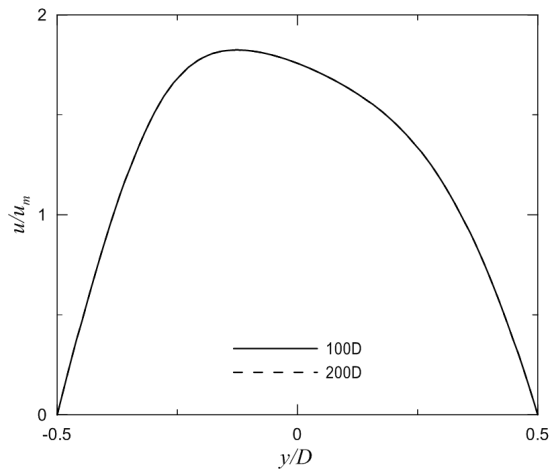
(a) Non-dimensional u velocity at pipe center.
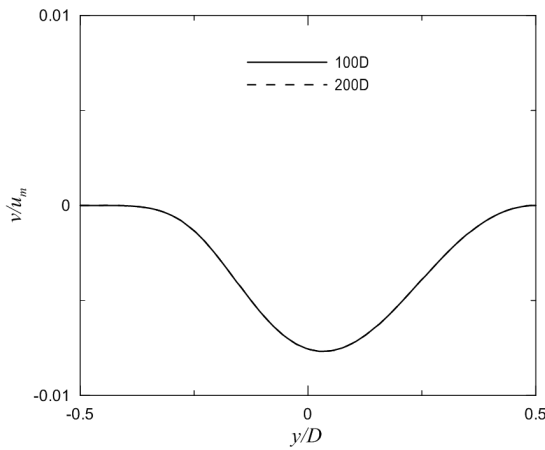
(b) Non-dimensional v velocity at pipe center.
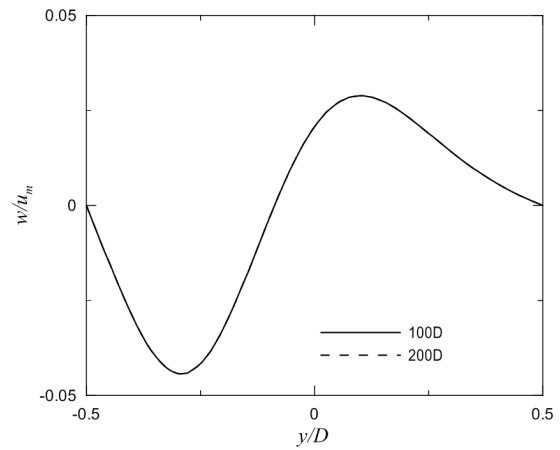
(c) Non-dimensional w velocity at pipe center.

Figure 5.12. Influence of outlet location on CFX results for velocity profiles at $20D$ for $\theta = 0°$. Double elbow case for $Re = 6 \times 10^2$.

Tables 5.2 and 5.3 show the results for Reynolds 1×10^4 and 2×10^6, respectively.

The results in Tabs. 5.2 and 5.3 show that the last sample, which is eight times larger, provides the desired magnitude for the deviation. All correction factors for straight pipe, single and double elbow presented in Chapter 7 have been performed with 2001 integrations points. Thus, the errors associated to them are expected to be 0.02% or better.

(a) Non-dimensional u velocity.

(b) Non-dimensional v velocity.

(c) Non-dimensional w velocity.
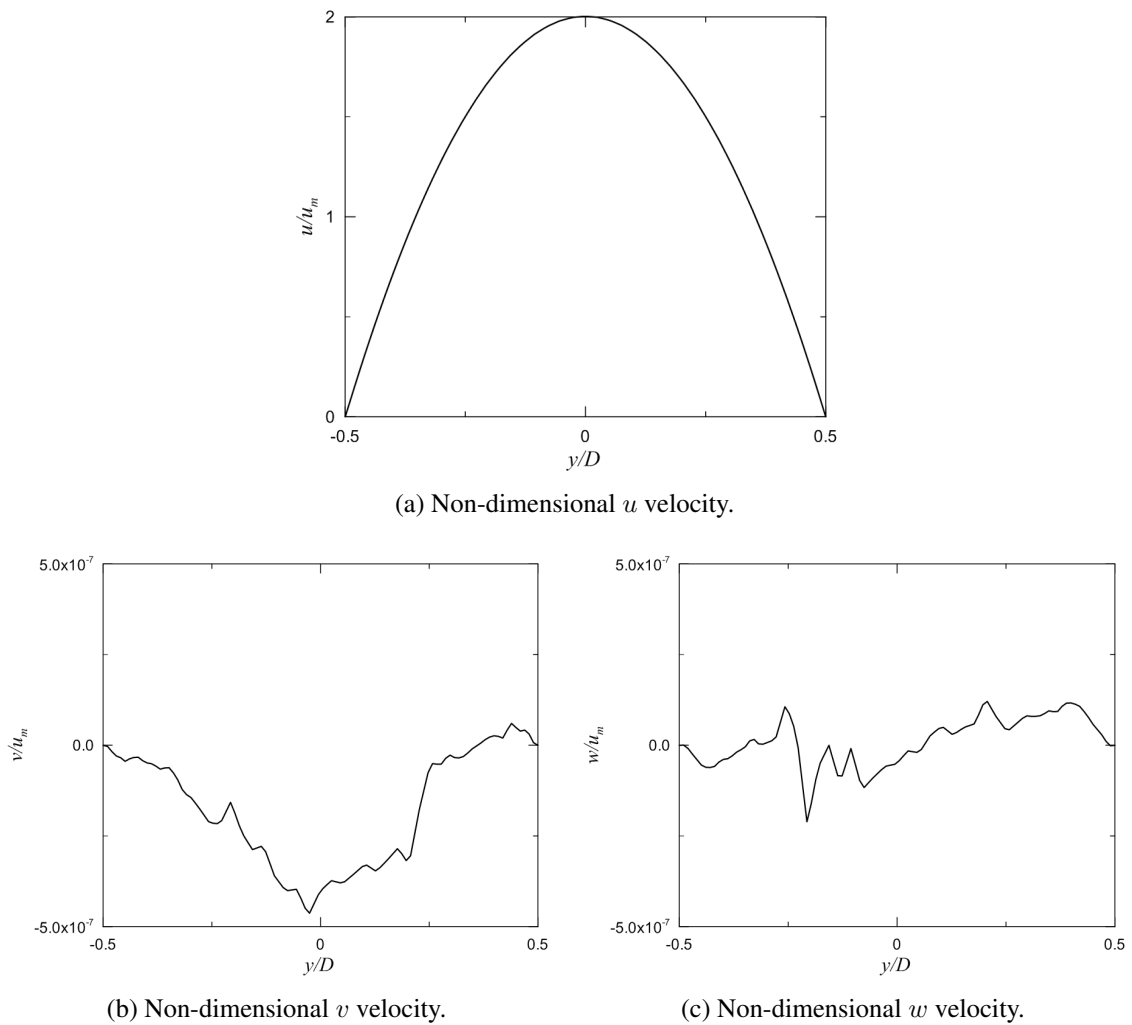
Figure 5.13. Velocity profiles for double bend case. CFX results at 200D for $\theta = 0°$ and $Re = 6 \times 10^2$.

Table 5.2. Deviation on the numerical factor caused by the number of integration points. ($Re = 1 \times 10^4$)

| Integration | k | | Deviation |
Points (N)	Analytical	Numerical	
251	0.919222014	0.920573233	0.15%
501	0.919222014	0.91981984	0.07%
1001	0.919222014	0.919486596	0.03%
2001	0.919222014	0.919339125	0.01%

Table 5.3. Deviation on the numerical factor caused by the number of integration points. ($Re = 2 \times 10^6$)

| Integration | k | | Deviation |
Points (N)	Analytical	Numerical	
251	0.951541057	0.953678324	0.22%
501	0.951541057	0.952535777	0.10%
1001	0.951541057	0.952004286	0.05%
2001	0.951541057	0.951756835	0.02%

Chapter 6

Validation Study

The quality of CFD results depends on well-posed definition of the problem. Numerical inputs, such as domain geometry, boundary conditions and fluid properties may be source of uncertainty. In this sense, validation is a necessary step aiming to indicate the level of confidence in numerical simulations. Typically, the results for different numerical input parameters are tested against experimental or analytical data, so that the best combination is found.

Validation study for the present work is carried out by comparing simulations with experimental data available in the work of Hilgenstock and Ernst [4]. In such work, the authors compare LDA measurements and simulation results for axial and tangential velocity profiles at a plane 5D downstream from a particular double elbow configuration (refer to Sec. 5.1) which is similar to the one proposed here. Hilgenstock and Ernst also evaluate four different mounting angles (0, 45, 90 and 135°). For the present validation, simulations have been compared with both numerical and experimental data of the reference work, and the convention of Fig. 5.1 regarding coordinate system and angles applies.

6.1   Validation Procedure and Results

Hilgenstock and Ernst [4] provide basic geometry and fluid specifications. Reynolds number considered is 2.25×10^5. The domain is presented in Sec. 5.1 and the fluid is ambient air. In the present work, the properties for air at $25° C$ have been considered and they are presented in

Tab. 6.1.

Table 6.1. Properties for air at $25°\ C$.

Density (ρ)	Dynamic Viscosity (μ)
$[kg/m^3]$	$[Pa\ s]$
1.185	1.831×10^{-5}

Despite reasonable definitions for geometry, information with respect to boundary conditions are not well defined in that work. Here, pressure outlet condition of 0 static pressure has been used for all cases as well as no-slip and smooth wall conditions.

Regarding inlet conditions, the authors explain that LDA measurements at 1.2D upstream from the double bend have been performed, indicating that the profile is not yet fully developed. They apply curve fitting for measured points and use the resulting function as inlet velocity condition. However, the authors provide neither the measured data nor the curve fitting function. Also turbulence quantities at boundaries are not commented. Thus, at first, uniform velocity profile has been considered. But a particular figure from [4] (which is better visualized in [40]) suggests that the inlet profile may be closer to the Nikuradse profile for turbulent fully developed flow. In the absence of further information and as an attempt for better results, fully developed flow profile has also been considered for validation. Now, it is important to present the sequence for validation procedure used in the present work.

Initially, CFX have been considered, using the k–ε model, default turbulence boundary conditions and uniform velocity profile. However, results for such parameters combination have not presented expected behaviour when compared to CFD results for k–ε obtained by Hilgenstock and Ernst [4], as displayed in Fig. 6.1.

Next step consisted in trying Nikuradse profile at inlet, also considering k–ε model and default boundary conditions, but results have still presented different trends compared to simulations of the reference paper (Fig. 6.2). Hence, turbulence model have been changed to k–$\varepsilon\ RNG$, since it is also tested by the authors, presenting better agreement with experiments. But results for k–$\varepsilon\ RNG$ and k–ε have not presented significant differences for both uniform and fully developed flow profile (Figs. 6.1 and 6.2). Thus, next possible change would be varying turbulence inlet conditions.

Since simulations performed by Hilgenstock and Ernst [4] use FLUENT, it has been considered important to investigate if FLUENT default turbulence inlet conditions were the same considered by CFX, instead of trying random values. In fact, FLUENT default conditions are unitary values for both k and ε, *i.e.*, $k = 1 m^2/s^2$ and $\varepsilon = 1 m^2/s^3$. Then, such conditions have been set for CFX but solutions have diverged for all attempts varying turbulence model (k–ε and k–ε RNG) and inlet velocity profile (uniform and fully developed), as shown in Tab. 6.2. Hence, FLUENT has been considered for simulations.

Before setting distinct parameters in a different code, some simulations considering the same conditions for CFX have been carried out. Thus, FLUENT results have been firstly obtained for uniform and fully developed velocity profiles, k–ε and k–ε RNG turbulence models, and for the same turbulence inlet conditions used so far, *i.e.*, $I = 5\%$ and $\tilde{\mu} = 10$. Such choice have been motivated by the possibility of comparing the performance of CFX and FLUENT under the same boundary conditions and turbulence models. In fact, the results have shown to be quite similar, as may be seen in Figs. 6.1 and 6.2.

Finally, FLUENT runs have been carried out for k–ε and k–ε RNG, considering $k[m^2/s^2]$ and $\varepsilon[m^2/s^3]$ equal to 1 at entrance (FLUENT default). Both models have shown better agreement under such conditions, as displayed in Figs. 6.1 and 6.2. Table 6.2 summarizes all performed runs for validation.

Table 6.2. Summary of validation cases.

Turbulence Inlet Condition	Inlet Velocity Profile	Turbulence Model	Software	
			CFX	FLUENT
$I = 5\%\, and\, \tilde{\mu} = 10$	Uniform	k–ε	$\checkmark$	$\checkmark$
		k–ε RNG	$\checkmark$	$\checkmark$
	Fully Developed	k–ε	$\checkmark$	$\checkmark$
		k–ε RNG	$\checkmark$	$\checkmark$
$k = 1m^2/s^2\, and\, \varepsilon = 1m^2/s^3$	Uniform	k–ε	X	$\checkmark$
		k–ε RNG	X	$\checkmark$
	Fully Developed	k–ε	X	$\checkmark$
		k–ε RNG	X	$\checkmark$

The first four rows in Tab. 6.2 represent cases using Eqs. (4.22) and (4.23) for turbulence inlet

conditions, and the last four rows make use of Eqs. (4.18) and (4.19). For the first cases turbulence intensity of 5% (medium) and viscosity ratio of 10 have been considered which leads to $k \approx 1.13m^2/s^2$ and $\varepsilon \approx 747.87m^2/s^3$ for $Re = 2.25 \times 10^5$. Nevertheless, $k[m^2/s^2]$ and $\varepsilon[m^2/s^3]$ equal 1 when directly specified.

It is important to emphasize that cases performed with CFX using unitary values for k and ε at the inlet have all diverged, despite the attempts with other interpolation and solution methods.

At this point, it is necessary to remark that the absence of better experimental data for disturbed profiles, containing well defined conditions and uncertainties, leads to restrictions in proceeding with precise validation. It is believed that Hilgenstock and Ernst [4] achieved better results due to the precise knowledge of real inlet conditions. In the present case, despite the uncertainties related to velocity and turbulence inlet conditions, overall results also show reasonable agreement with experiments.

By comparing turbulence inlet conditions, unitary values for k and ε apparently provide better agreements. Such performance is mainly noticed for near-wall and tangential velocities. Thus, regarding the results for such condition, one may still discuss the performance of turbulence models. However, both models present reasonable results, so that k–ε shows to be advantageous for specific locations whereas k–ε RNG provide better agreement for another region. Thus, taking into account such similarity and in the absence of better defined conditions, the choice for turbulence model is based on indications given by the literature and by Hilgenstock and Ernst [4]. Specialized literature [3, 73] comments, and Hilgenstock and Ernst [4] could verify that k–ε RNG usually provide better results for swirl flows. Hence, since the main objective of this dissertation depends on disturbed flows, k–ε RNG model has been chosen.
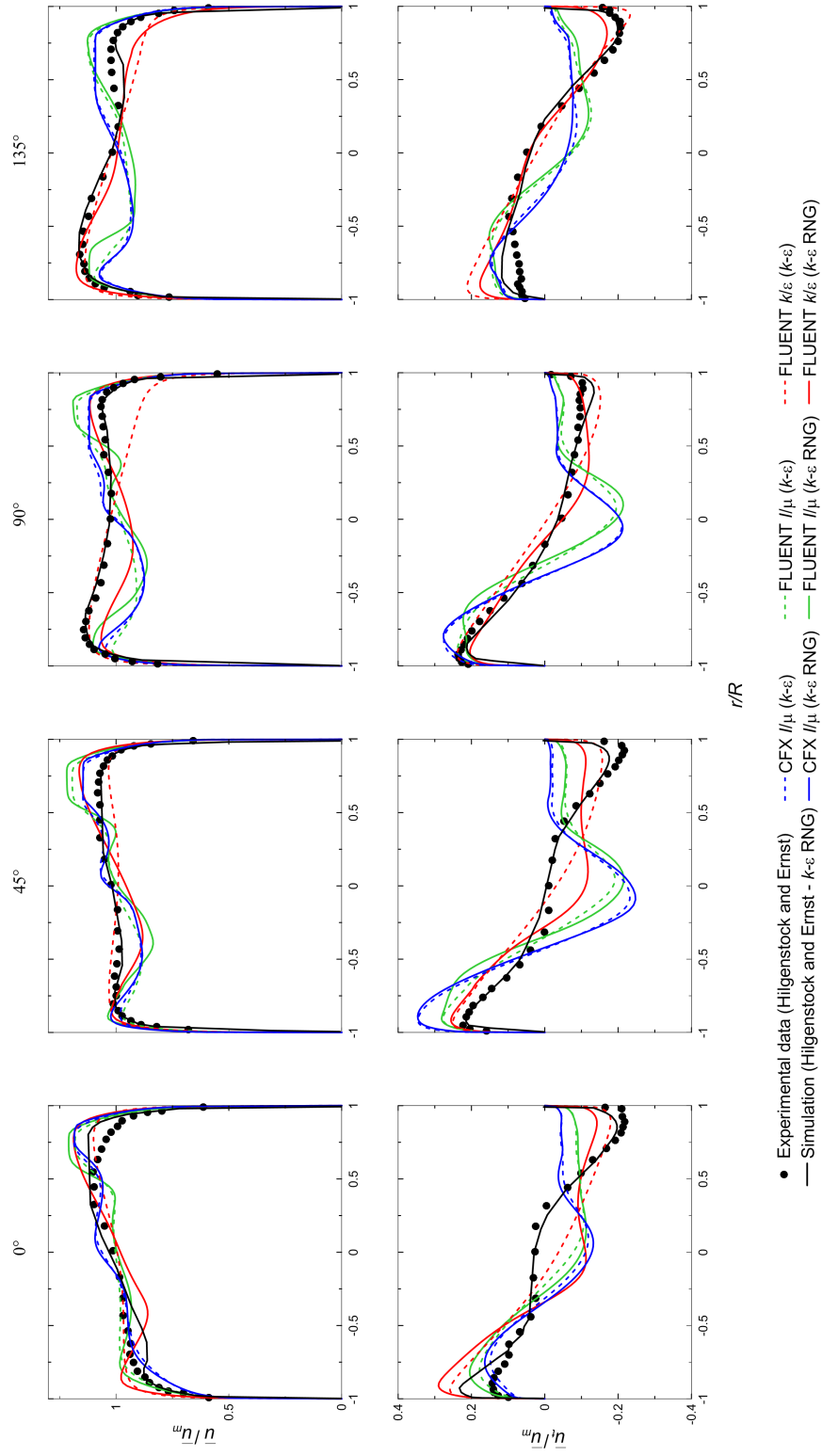
Figure 6.1. Comparison with experimental data of Hilgenstock and Ernst [4] for uniform velocity profile at inlet.
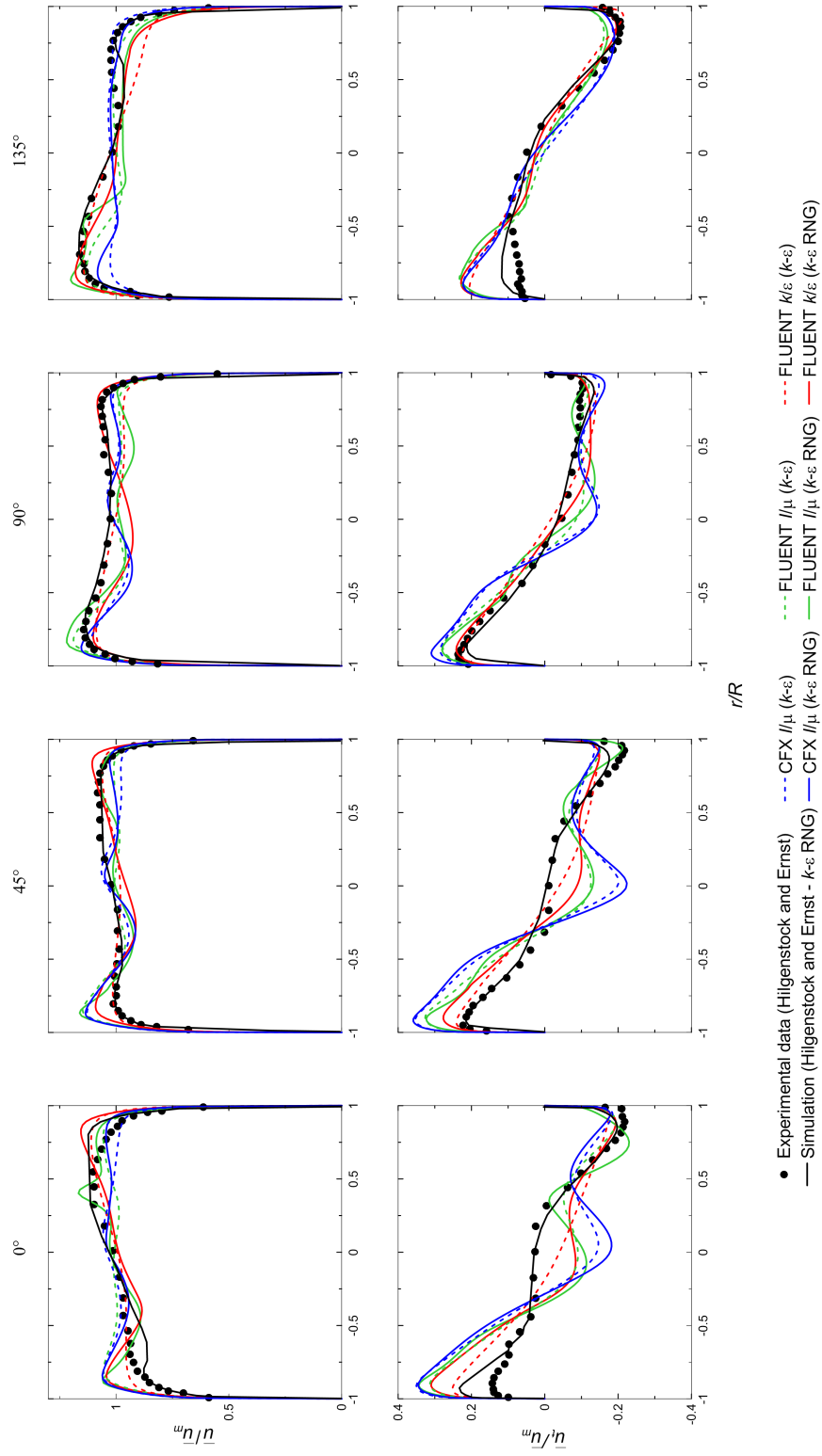
Figure 6.2. Comparison with experimental data of Hilgenstock and Ernst [4] for fully developed velocity profile at inlet.

Part III

Results and Discussions

Chapter 7

Simulated Correction Factors

The main goal of the present work is to evaluate the influence of disturbed profiles on the correction factor of ultrasonic flow meters. Such influence is directly related to deviations on flow rate measurements, as commented in Chapter 2. Furthermore, validation study in Chapter 6 indicates that FLUENT results for unitary k and ε at inlet provide reasonable results for the flow field downstream from a double elbow.

This chapter presents the results for the correction factor downstream of single and double elbow configurations. Several axial and angular positions for the meter installation are tested as well as different Reynolds numbers. Before showing and commenting the main results, boundary conditions and fluid models are presented and justified. Also, the results for the k factor in a straight pipe are shown. Such results represent the reference for fully developed flow condition.

7.1   Boundary Conditions and Fluid Modelling

The three geometries presented in this chapter have been tested for the same conditions. Such conditions are now presented and justified.

First of all, air has been considered for all simulations and the properties for air at $25°\ C$ in Tab. 6.1 have been applied again. On may consider that flare gas (which is a natural gas) real composition may influence the flow field. In fact, Hill *et al.* [52] show that flow measurements

performed for natural gas and atmospheric air are quite similar, specially for high velocities. Moreover, Salgado and Ramos [94] show that perfect gas assumption is reasonable with regard to flare gas thermodynamic properties, although the fluid-dynamical consequences of such assumption have not been tested yet. Since perfect gas involves thermodynamic properties (*i.e.*, includes new equation and boundary conditions for energy), the simplest way is to consider ambient air. Such approach is usual (references [4, 52], for instance) and the influence of fluid properties on the simulation of ultrasonic flow measurement is left as suggestion for future work.

Regarding inlet conditions, uniform velocity profile has been assumed in all following simulations. Equations (4.15) and (4.16) have been used for Reynolds numbers from 1×10^4 to 2×10^6. The k–ε RNG turbulence model has been considered and inlet conditions for turbulence have been kept as default, as consequence of good results in validation study. Walls have been considered to be smooth with no-slip condition. Outlet condition has been specified as 0 atm static pressure (atmospheric total pressure).

Table 7.1 presents simulated cases and the pressure-velocity algorithm (refer to Sec. 4.3) associated to each case.

Table 7.1. Pressure-velocity algorithms for simulated cases.

Re	Cases		
	Straight Pipe	**Single Elbow**	**Double Elbow**
1×10^4	SIMPLE	SIMPLE	SIMPLE
2×10^4	SIMPLE	SIMPLE	SIMPLE
4×10^4	SIMPLE	SIMPLE	SIMPLE
6×10^4	SIMPLE	SIMPLE	SIMPLE
1×10^5	SIMPLE	SIMPLE	Coupled
2×10^5	SIMPLE	SIMPLE	Coupled
6×10^5	SIMPLE	Coupled	Coupled
1×10^6	SIMPLE	Coupled	Coupled
2×10^6	SIMPLE	SIMPLE	Coupled

7.2 Straight Pipe Case

As commented above, straight pipe case plays the role of the numerical reference for fully developed flow. Before applying any calculation for the k factor, the validation procedure is presented, which consists in comparing the velocity profile with fully developed flow profiles available in the literature. Such qualitative preliminary test have been conducted aiming to investigate how close to fully developed condition the straight pipe simulations are. For this specific case, CFX have also been tested using default conditions and k–ε model. Its results are also displayed and commented in the following.

In this preliminary test, simulated velocity profile is plotted against Nikuradse semi-empirical profile (Eq. (2.18), see Chapter 2), which is recommended by AGA 9 [31] and by the Brazilian regulation [17]. Furthermore, such velocity profile is widely used in the literature and is specially known for the particular case for which $n = 7$ in Eq. (2.18), yielding the so called $1/7th$ profile.

The power law proposed by Nikuradse was evaluated by De Chant [95], who proposed that such power law is "not only a curve fit of experimental data, but also the analytical solution of a non-linear boundary value problem based on a large Reynolds number asymptotic closures" [95]. De Chant also makes some comments on better results of Nikuradse profile for high Reynolds numbers. Such behaviour may be checked in Fig. 7.1.

The choice of the axial position at 80D is consequence of the previous analysis consisted in comparing velocity profiles for minimum and maximum Reynolds numbers considered in the present work for 5 axial positions: 20, 40, 60, 80 and 100D. Deviations between the velocities at such positions have been calculated for some radial points (-0.75, -0.5, 0, 0.5 and 0.75R), which also allows checking profile symmetry. Relative velocity deviations for lowest and higher Re are presented in Tabs. 7.2 and 7.3, respectively.

Observation of Tabs. 7.2 and 7.3 suggests that assuming fully developed condition at 80D may be reasonable, since relative deviations of analysed radial points from 80 to 100D are negligible (smaller then 0.005%, at least).

Figure 7.2 below presents correction factors resulting from numerical integration of simulated flow profiles at 80D for straight pipe case. In this case, the correction factor obtained by

(a) Lowest simulated Reynolds.

(b) Highest simulated Reynolds.
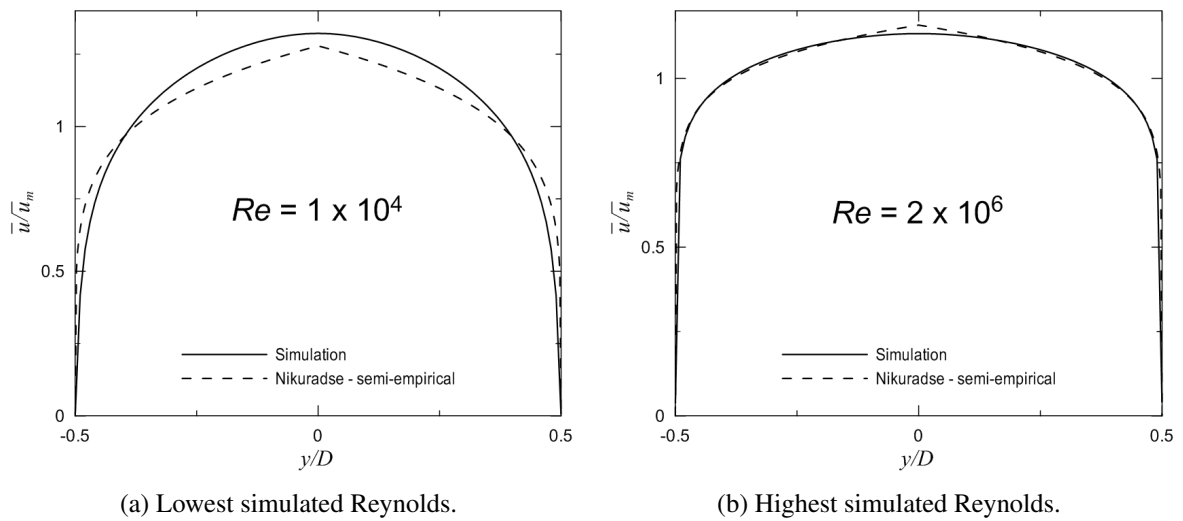
Figure 7.1. Simulated velocity profiles for straight pipe case at 80D against Nikuradse power law.

Eq. (2.19), which is based on the semi-empirical relation of Nikuradse profile, is the reference. Simulated correction factors result from numerical integration of flow field along the acoustic path (refer to Sec. 5.6) for specific Re. Numerical factors k seem to be in good agreement with semi-empirical-based reference.
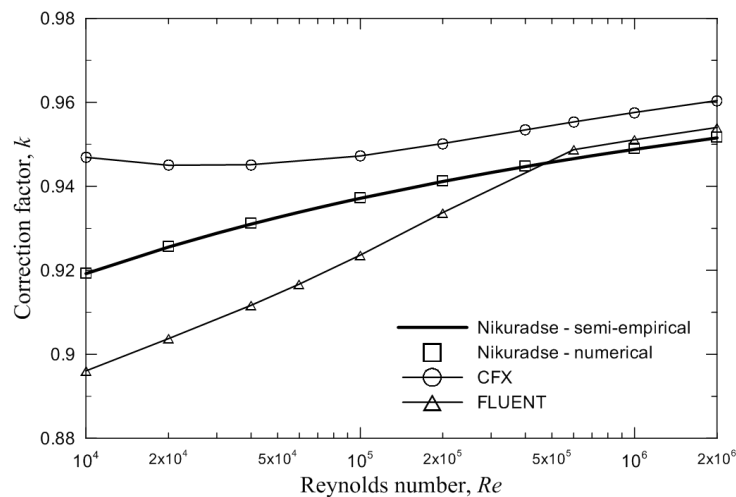
Figure 7.2. Numerical results for the correction factor for a straight pipe.

Simulation results (Fig. 7.2) indicate better agreement with reference as Reynolds increases, as expected by regarding Fig. 7.1. It is remarkable that correction factors for $Re < 1 \times 10^5$ for CFX present divergent behaviour when compared to the reference, increasing whereas the reference decreases. Such behaviour leads to overestimation of Nikuradse-base correction factor, reaching

the maximum deviation of 3.01% for $Re = 1 \times 10^4$. For FLUENT results, maximum deviation of magnitude 2.52% is reached also for the lowest Re, but results are always in agreement with overall increasing tendency for higher Reynolds and deviations are considerably improved for $Re \geq 6 \times 10^5$, achieving the minimum value of 0.23% for $Re = 6 \times 10^5$. All deviations are presented in Tab. 7.4.

It is important to emphasize that CFX using k–ε has been considered only to check how the results behave for other approaches. For all other simulations only FLUENT using k–ε RNG has been considered.

7.3 Curved Cases

Same procedure used for straight pipe has been applied for single and double elbow configurations. Furthermore, since asymmetries (see Chapter 3) appear, several mounting angles (θ) and axial positions along the straight pipe section have been explored in order to investigate favourable installations aiming the quality of ultrasonic flow measurement.

The following figures (Figs. 7.3 and 7.5) present the plots for correction factors calculated downstream from single and double elbow installations, respectively, varying with Re at several axial positions (1, 3, 5, 8, 10, 12, 15, 18, 20, 40, 60 and 80D) along the straight pipe section. Also, several mounting angles (0, 30, 45, 60, 90, 120, 135, 150 and 180°) have been explored and they may be identified by different colours or symbols. Smaller intervals between axial positions up to 20D are motivated by regulations and manufacturers recommendations for installing ultrasonic flow meters at 20D or less, sometimes 10D, downstream from pipe curves [23, 25, 31]. Thus, test sections up to 20D aim mainly to investigate how affected is the correction factor. Distances larger than 20D basically provide the observations of disturbances effects decaying.

Moreover, two references have been considered. Besides the Nikuradse-based correction factor, simulated correction factors at 80D for straight pipe (as shown in Fig. 7.2) have also been considered.

Figure 7.3 contains simulated correction factors with fixed scales, aiming better comparisons.

The first remarkable feature is the decay of disturbances effects on the correction factor as the metering section is placed further away from the curve. Of course, such behaviour is expected and it is worth highlighting that correction factor deviations for intermediate Reynolds number may be higher than 1% even 80D downstream from the single elbow (see Tabs. 7.5 and 7.6).

Furthermore, mounting angle affects the correction factor and its effect seems to present the same pattern along the pipe. As an example, one may take simulated correction factors for $\theta = 180°$ in Fig. 7.3. Generally speaking, such angle provides higher overestimations and such behaviour repeats for almost all tested axial positions. Same tendency is noticed for $\theta = 150°$, for which deviations are a bit lower than for $\theta = 180°$. Decreasing the mounting angle from $\theta = 180°$ down to $\theta = 90°$, the trend is still similar. It is remarkable that $\theta = 90°$ usually provides the lowest deviations. Decreasing θ from $90°$ to $0°$ deviations tend to increase.

All behaviours commented above may also be observed in Fig. 7.4, in which correction factor deviations (refer to Sec. 4.4) are plotted against several axial positions for each Reynolds number and mounting angle. Essentially, Fig. 7.4 shows the same results of Fig. 7.3, but from another point of view, which provides some other observations. In Fig. 7.4, the effect of Reynolds number may be easier checked. Basically, since higher Re flows lead to more momentum, disturbances effects remain for farther axial positions, which tend to increase correction factor deviations.

Tables 7.5 and 7.6 also help the analysis by presenting some quantitative results. For instance, correction factor deviation could reach 27.87% if installed at 1D from a single bend with mounting angle of $180°$ for $Re = 1 \times 10^4$. On the other hand, the same pipe configuration with $\theta = 60°$ could lead to deviation of 1.69% for the same Reynolds number. This result is important for showing how sensitive ultrasonic flow meters can be to installation effects, and mainly for pointing out that deviations due to flow disturbances might lead to significantly values, reaching approximately 30% depending on the flow and measurement conditions.

Figure 7.5 presents simulated correction factors obtained for double elbow configuration. One may notice that the parallelism between simulated and reference correction factors is not clear as for single elbow case. In fact, the complexity of the flow field downstream of a double elbow is reflected in the behaviour of simulated correction factors. Patterns seems less frequent and less obvious as well, and curves present some derivative sign changes, which would lead to increasing computational effort to find the zero of the function (refer to Sec. 2.3) as part of the

measurement process, if simulated factor k were hypothetically implemented for correction.

In a general form, one may observe in Tabs. 7.7 and 7.8 that correction factors tend to reach a maximumm value somewhere between 10 and 20D for mounting angles of less then $90°$, which is contrary to the possible tendency to think that the farther from the curve the better. Thus, special attention is needed to place ultrasonic metering sections, specially downstream from double elbow configurations. On the other hand, for mounting angles greater than $90°$, maximum usually occurs close to the curve and basically decays for farther axial positions. Such behaviours may be also observed in Fig. 7.6.

Similarly to single elbow case, fully developed condition is not achieved yet at 80D and deviations may reach 1.63% for $Re = 1 \times 10^5$ (Tab. 7.7).

A remarkable general result may be observed at 20D downstream of both single and double elbow. Deviations for the lowest Re considered are lower than 1% for every tested mounting angle. On the other hand, deviations are higher than 1% and may reach more than 8% for the maximum Reynolds number.

Table 7.2. Deviations concerned to velocity profiles development for $Re = 1 \times 10^4$.

y/R	$\bar{u}\,[m/s]$		Relative	$\bar{u}\,[m/s]$		Relative	$\bar{u}\,[m/s]$		Relative	$\bar{u}\,[m/s]$		Relative
	20D	**40D**	**Deviation**	**40D**	**60D**	**Deviation**	**60D**	**80D**	**Deviation**	**80D**	**100D**	**Deviation**
-0.75	0.520	0.521	0.25%	0.521	0.521	0.00%	0.521	0.521	0.00%	0.521	0.521	0.00%
-0.50	0.621	0.620	-0.16%	0.620	0.620	0.00%	0.620	0.620	0.00%	0.620	0.620	0.00%
-0.25	0.669	0.665	-0.55%	0.665	0.665	0.01%	0.665	0.665	0.00%	0.665	0.665	0.00%
0.00	0.686	0.681	-0.74%	0.681	0.681	0.01%	0.681	0.681	0.00%	0.681	0.681	0.00%
0.25	0.669	0.665	-0.55%	0.665	0.665	0.01%	0.665	0.665	0.00%	0.665	0.665	0.00%
0.50	0.621	0.620	-0.16%	0.620	0.620	0.00%	0.620	0.620	0.00%	0.620	0.620	0.00%
0.75	0.520	0.521	0.25%	0.521	0.521	0.00%	0.521	0.521	0.00%	0.521	0.522	0.00%

Table 7.3. Deviations concerned to velocity profiles development $Re = 2 \times 10^6$.

y/R	$\bar{u}\,[m/s]$		Relative	$\bar{u}\,[m/s]$		Relative	$\bar{u}\,[m/s]$		Relative	$\bar{u}\,[m/s]$		Relative
	20D	**40D**	**Deviation**	**40D**	**60D**	**Deviation**	**60D**	**80D**	**Deviation**	**80D**	**100D**	**Deviation**
-0.75	103.96	103.08	-0.85%	103.08	103.82	0.71%	103.82	103.82	0.00%	103.82	103.82	0.00%
-0.50	113.72	112.23	-1.33%	112.23	111.69	-0.49%	111.69	111.87	0.16%	111.87	111.87	0.00%
-0.25	114.05	117.76	3.15%	117.76	115.29	-2.15%	115.29	115.44	0.13%	115.44	115.44	0.00%
0.00	114.05	120.95	5.71%	120.95	116.56	-3.76%	116.56	116.67	0.09%	116.67	116.67	0.00%
0.25	114.05	117.76	3.15%	117.76	115.29	-2.15%	115.29	115.44	0.13%	115.44	115.44	0.00%
0.50	113.72	112.23	-1.33%	112.23	111.69	-0.49%	111.69	111.87	0.16%	111.87	111.87	0.00%
0.75	103.96	103.08	-0.85%	103.08	103.82	0.71%	103.82	103.82	0.00%	103.82	103.82	0.00%

Table 7.4. Values for CFX and FLUENT correction factor deviations from Nikuradse-based correction factor for straight pipe at 80D.

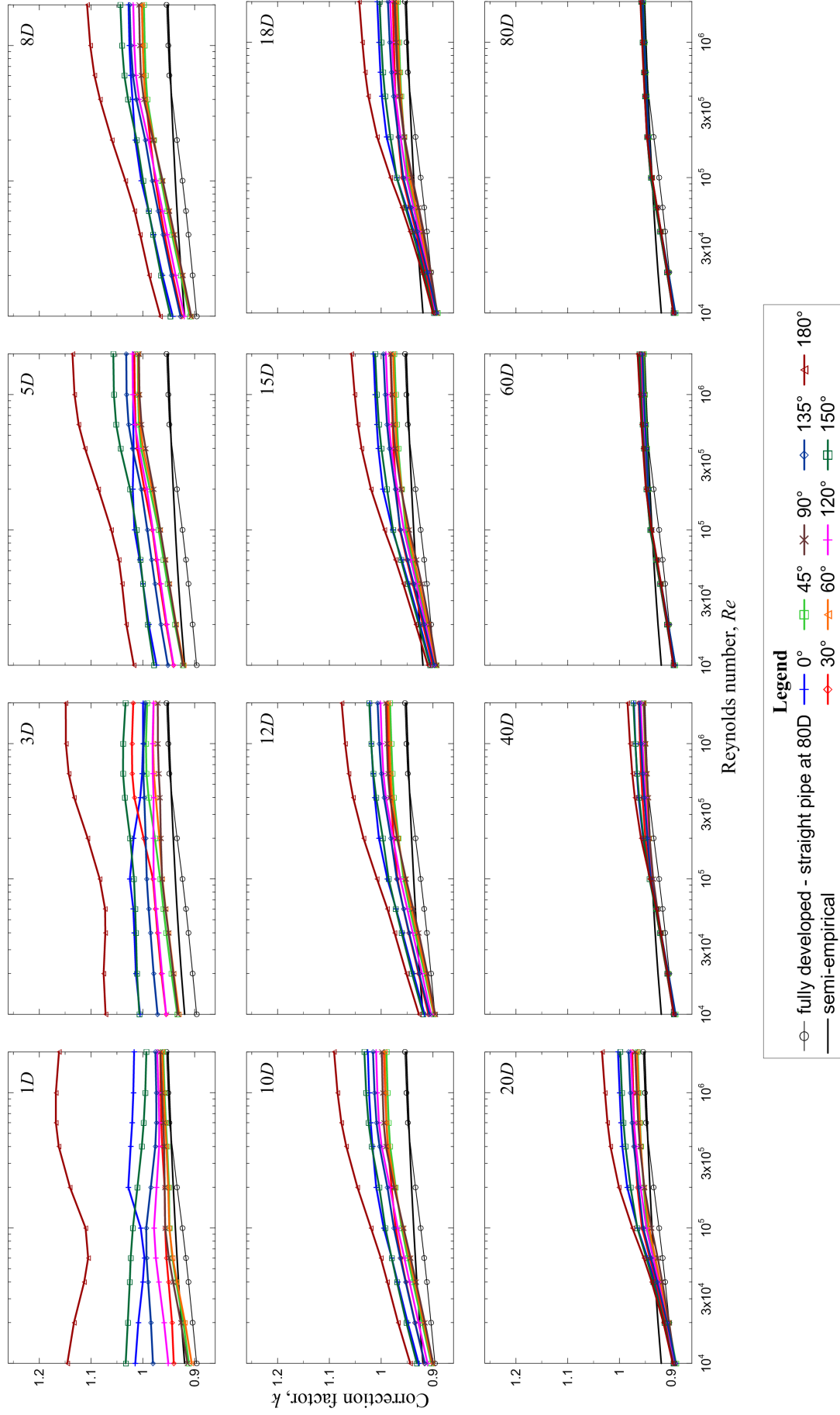| Re	Δk	
	CFX	FLUENT
1×10^4	3.01%	-2.52%
2×10^4	2.10%	-2.36%
4×10^4	1.52%	-2.08%
6×10^4	X	-1.83%
1×10^5	1.08%	-1.44%
2×10^5	0.96%	-0.79%
6×10^5	0.92%	0.23%
1×10^6	0.93%	0.24%
2×10^6	0.93%	0.26%

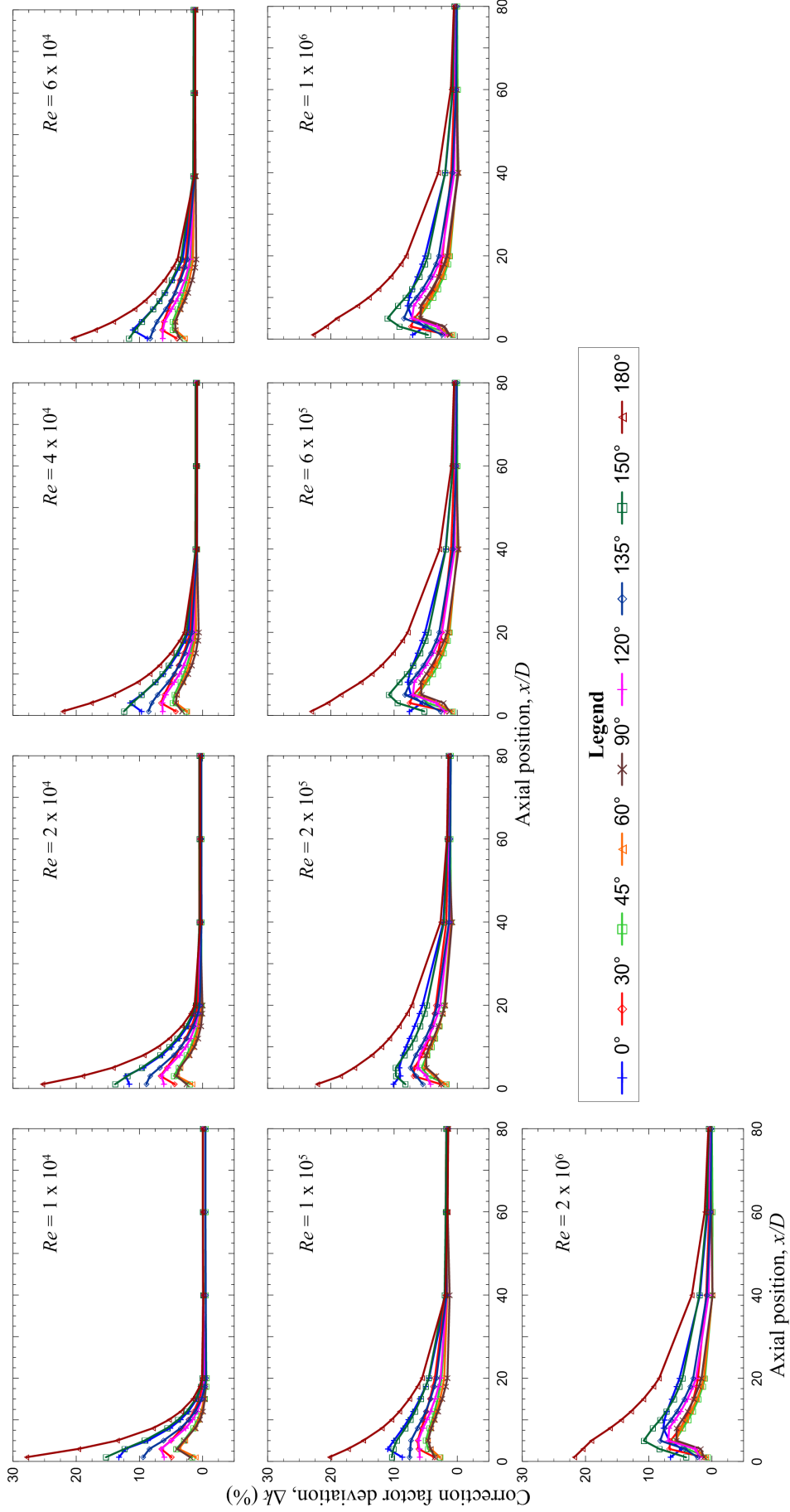Figure 7.3. Simulated correction factors downstream from a single elbow.

Figure 7.4. Correction factor deviations downstream from a single elbow.
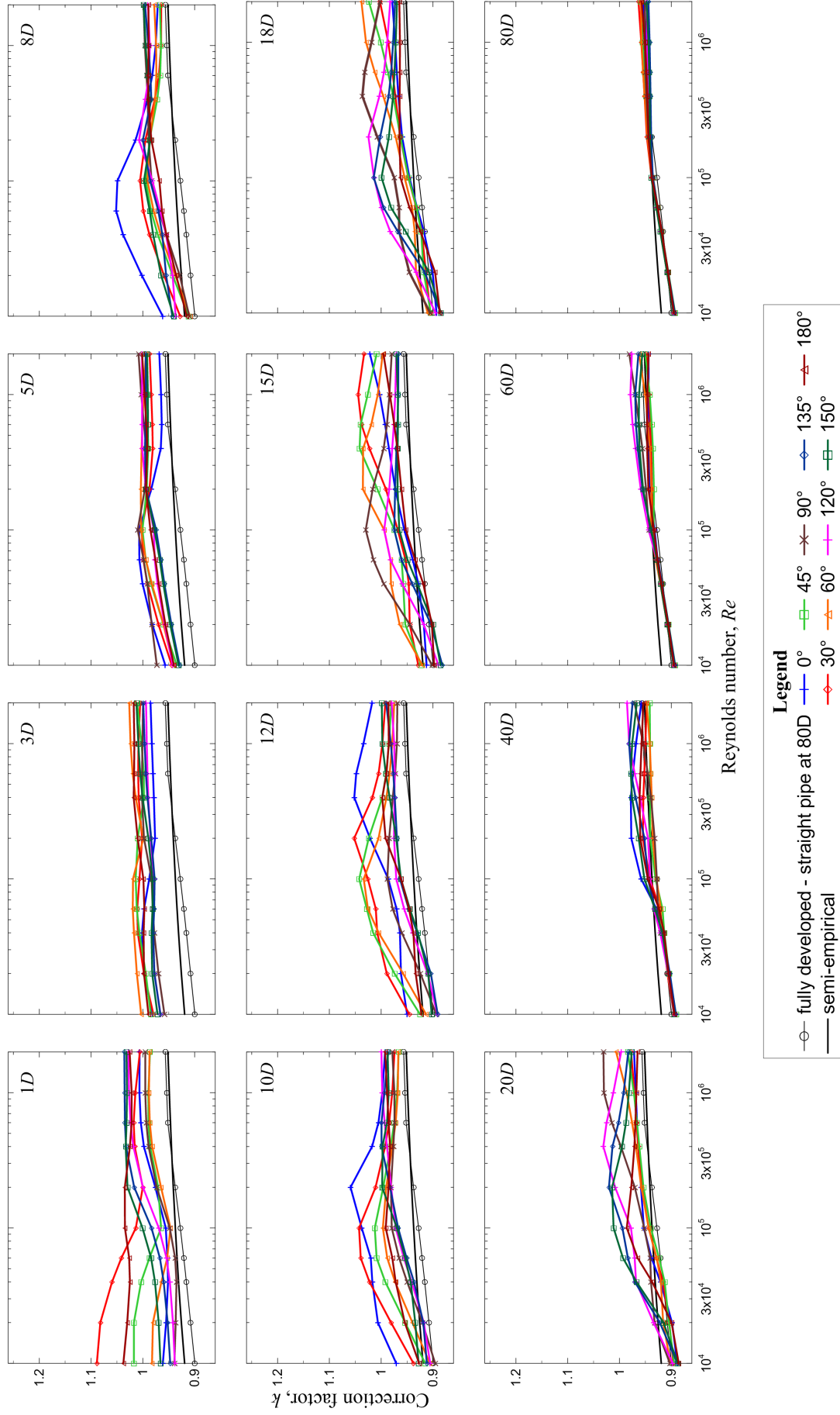
Figure 7.5. Simulated correction factors downstream from a double elbow.
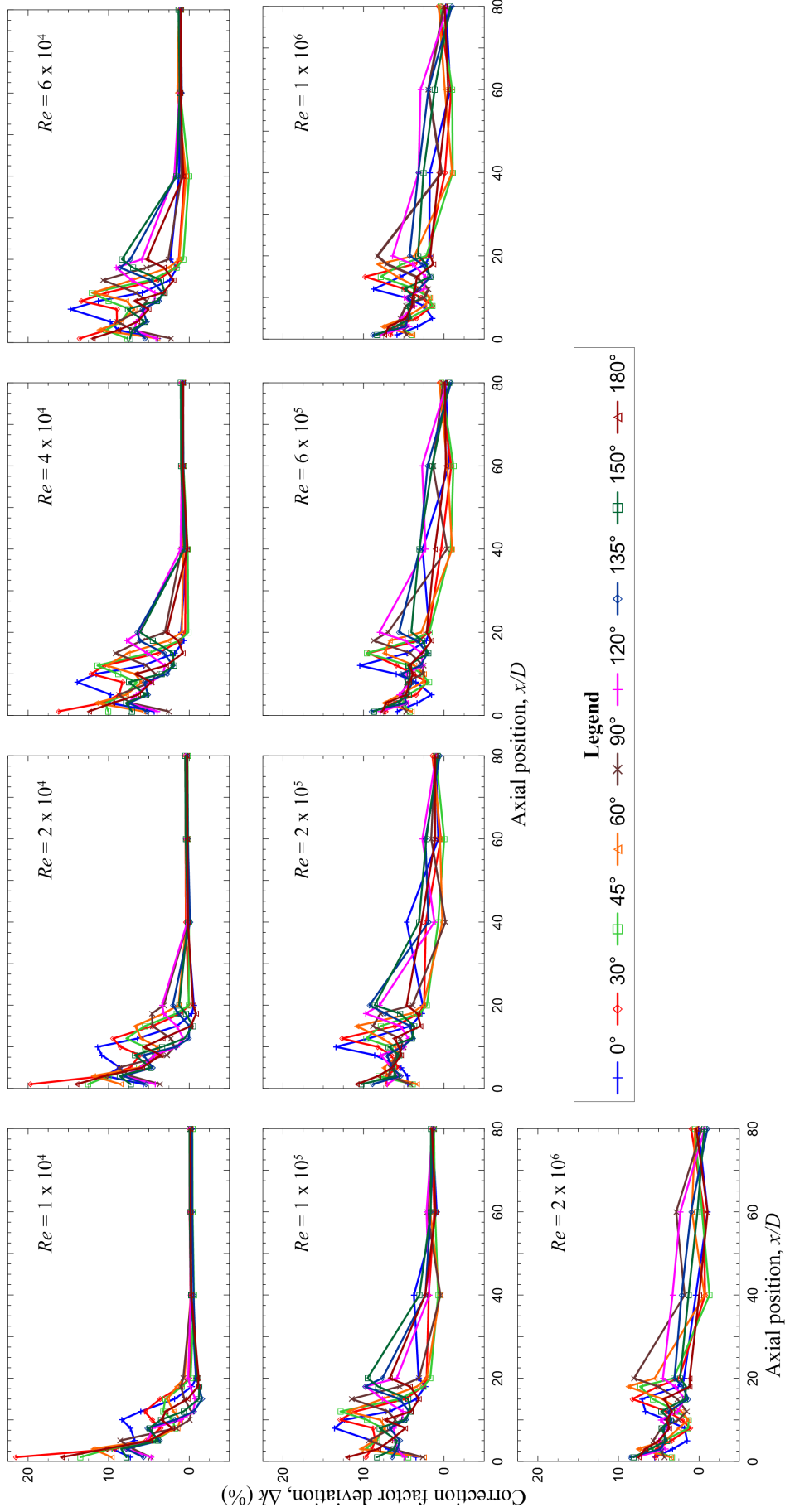
Figure 7.6. Correction factor deviations downstream from a double elbow.

Table 7.5. Summary of correction factor deviations for single elbow case. (Part 1)

x/D	0°	30°	45°	60°	90°	120°	135°	150°	180°
					$Re = 1 \times 10^4$				
1	13.22%	4.93%	1.67%	1.06%	1.97%	6.10%	9.41%	15.30%	27.87%
5	8.65%	5.03%	2.97%	2.76%	2.94%	4.95%	6.19%	9.20%	13.54%
10	3.52%	2.24%	0.80%	0.61%	0.41%	1.61%	2.18%	3.89%	5.33%
15	0.93%	0.51%	-0.30%	-0.19%	-0.35%	0.15%	0.16%	1.07%	1.53%
20	0.03%	-0.07%	-0.59%	-0.29%	-0.36%	-0.24%	-0.53%	0.00%	0.11%
40	-0.08%	-0.06%	-0.46%	-0.07%	-0.08%	-0.09%	-0.49%	-0.10%	-0.12%
60	-0.04%	-0.03%	-0.43%	-0.02%	-0.04%	-0.02%	-0.44%	-0.03%	-0.05%
80	-0.04%	-0.02%	-0.44%	-0.02%	-0.03%	-0.02%	-0.44%	-0.03%	-0.05%
					$Re = 2 \times 10^4$				
1	11.61%	4.41%	2.01%	1.63%	2.53%	6.11%	8.91%	13.86%	25.37%
5	9.39%	5.67%	3.80%	3.51%	3.59%	5.52%	6.80%	9.62%	14.17%
10	4.97%	3.41%	1.90%	1.58%	1.30%	2.67%	3.43%	5.27%	7.03%
15	2.34%	1.74%	0.76%	0.61%	0.26%	1.14%	1.48%	2.59%	3.27%
20	0.93%	0.77%	0.18%	0.27%	0.03%	0.47%	0.45%	1.08%	1.27%
40	0.42%	0.53%	0.22%	0.51%	0.39%	0.48%	0.18%	0.48%	0.36%
60	0.41%	0.52%	0.21%	0.51%	0.39%	0.51%	0.20%	0.51%	0.39%
80	0.40%	0.52%	0.20%	0.52%	0.40%	0.52%	0.20%	0.52%	0.40%
					$Re = 1 \times 10^5$				
1	8.71%	3.60%	2.69%	2.74%	3.59%	5.93%	7.55%	10.35%	20.24%
5	10.03%	6.26%	4.97%	4.64%	4.61%	6.17%	7.33%	9.58%	14.87%
10	7.74%	5.25%	3.98%	3.72%	3.59%	4.80%	5.61%	7.39%	10.40%
15	5.93%	4.35%	3.10%	2.73%	2.38%	3.52%	4.25%	5.79%	7.58%
20	4.48%	3.56%	2.49%	2.07%	1.56%	2.65%	3.30%	4.53%	5.57%
40	1.74%	1.88%	1.59%	1.58%	1.21%	1.67%	1.70%	2.00%	1.88%
60	1.58%	1.85%	1.71%	1.82%	1.52%	1.81%	1.70%	1.83%	1.55%
80	1.47%	1.75%	1.63%	1.74%	1.45%	1.73%	1.61%	1.73%	1.44%

Table 7.6. Summary of correction factor deviations for single elbow case. (Part 2)

x/D	0°	30°	45°	60°	90°	120°	135°	150°	180°
					$Re = 2 \times 10^5$				
1	10.10%	2.59%	1.68%	1.84%	2.57%	4.24%	5.44%	8.21%	22.17%
5	9.18%	6.77%	5.63%	5.18%	4.89%	6.26%	7.41%	9.73%	16.28%
10	8.11%	4.94%	4.08%	4.21%	4.40%	5.28%	5.79%	7.48%	12.00%
15	6.73%	3.99%	2.82%	2.87%	2.98%	3.77%	4.19%	5.87%	9.20%
20	5.49%	3.40%	2.08%	1.98%	1.94%	2.71%	3.16%	4.80%	7.20%
40	2.21%	1.73%	0.99%	1.00%	0.84%	1.23%	1.31%	2.11%	2.64%
60	1.58%	1.48%	1.09%	1.36%	1.36%	1.39%	1.13%	1.53%	1.63%
80	1.41%	1.38%	1.04%	1.37%	1.41%	1.36%	1.03%	1.37%	1.40%
					$Re = 1 \times 10^6$				
1	7.07%	1.50%	0.72%	0.90%	1.25%	1.95%	2.41%	4.64%	22.80%
5	7.12%	6.78%	6.11%	5.97%	5.83%	7.16%	8.43%	11.02%	19.02%
10	7.59%	4.34%	3.84%	4.23%	4.83%	5.91%	6.48%	8.18%	14.00%
15	6.35%	3.02%	2.16%	2.44%	2.92%	3.86%	4.31%	5.98%	10.51%
20	5.10%	2.34%	1.17%	1.29%	1.63%	2.49%	2.93%	4.65%	8.08%
40	1.89%	0.97%	-0.01%	-0.06%	-0.15%	0.47%	0.76%	1.92%	3.00%
60	0.70%	0.46%	-0.05%	0.15%	0.15%	0.32%	0.19%	0.75%	1.02%
80	0.47%	0.40%	0.04%	0.34%	0.40%	0.38%	0.08%	0.45%	0.53%
					$Re = 2 \times 10^6$				
1	6.58%	1.28%	0.69%	0.90%	1.27%	1.91%	2.27%	4.10%	21.79%
5	6.75%	6.53%	5.83%	5.70%	5.61%	6.91%	8.18%	10.79%	19.06%
10	7.51%	4.26%	3.74%	4.10%	4.69%	5.83%	6.47%	8.22%	14.34%
15	6.37%	2.94%	2.13%	2.40%	2.86%	3.86%	4.37%	6.03%	10.86%
20	5.12%	2.22%	1.12%	1.28%	1.65%	2.52%	2.97%	4.67%	8.35%
40	1.90%	0.91%	-0.06%	-0.08%	-0.10%	0.53%	0.81%	1.99%	3.18%
60	0.70%	0.44%	-0.09%	0.10%	0.12%	0.32%	0.22%	0.81%	1.14%
80	0.46%	0.37%	0.01%	0.31%	0.36%	0.36%	0.09%	0.47%	0.57%

Table 7.7. Summary of correction factor deviations for double elbow case. (Part 1)

x/D	0°	30°	45°	60°	90°	120°	135°	150°	180°
					$Re = 1 \times 10^4$				
1	7.28%	21.51%	13.51%	9.62%	4.81%	4.70%	5.69%	7.79%	15.79%
5	6.76%	5.35%	4.29%	5.04%	8.59%	5.15%	3.67%	3.89%	4.90%
10	8.34%	4.63%	2.10%	1.11%	-0.04%	1.02%	1.74%	3.53%	3.42%
15	1.80%	3.59%	2.96%	2.71%	0.60%	-0.75%	-1.59%	-1.20%	0.17%
20	-0.85%	-0.02%	-0.18%	0.59%	0.73%	0.11%	-0.89%	-0.96%	-1.17%
40	-0.24%	-0.17%	-0.59%	-0.21%	-0.28%	-0.19%	-0.55%	-0.21%	-0.26%
60	-0.18%	-0.06%	-0.43%	-0.07%	-0.17%	-0.07%	-0.38%	-0.07%	-0.19%
80	-0.17%	-0.04%	-0.40%	-0.04%	-0.16%	-0.04%	-0.35%	-0.04%	-0.17%
					$Re = 2 \times 10^4$				
1	5.67%	19.73%	12.56%	8.49%	3.63%	4.21%	5.35%	7.26%	13.98%
5	8.62%	7.30%	6.25%	6.24%	8.74%	5.99%	4.54%	4.79%	5.83%
10	11.35%	8.54%	5.52%	3.96%	1.84%	1.54%	1.65%	3.36%	5.60%
15	1.53%	4.54%	5.50%	6.69%	4.54%	1.54%	-0.02%	-0.45%	-0.19%
20	-0.58%	0.01%	0.07%	1.31%	3.14%	3.36%	2.03%	1.24%	-0.48%
40	0.21%	0.42%	0.02%	0.36%	0.17%	0.24%	-0.12%	0.18%	0.15%
60	0.26%	0.44%	0.13%	0.44%	0.24%	0.42%	0.17%	0.43%	0.23%
80	0.27%	0.49%	0.20%	0.48%	0.26%	0.47%	0.25%	0.49%	0.27%
					$Re = 1 \times 10^5$				
1	3.47%	9.73%	4.45%	2.48%	2.63%	4.92%	6.46%	8.33%	12.01%
5	9.05%	8.53%	8.35%	8.64%	9.35%	5.97%	5.49%	5.85%	6.68%
10	12.33%	12.89%	9.60%	7.91%	6.05%	5.23%	4.71%	4.96%	7.31%
15	3.44%	4.80%	5.51%	7.64%	11.49%	7.63%	5.52%	4.47%	3.11%
20	3.16%	2.16%	1.72%	2.15%	3.10%	5.86%	7.65%	9.50%	6.74%
40	3.74%	1.90%	0.74%	0.52%	0.45%	1.83%	2.31%	3.06%	2.34%
60	0.92%	1.22%	1.12%	1.73%	2.08%	2.17%	1.67%	1.65%	1.06%
80	1.44%	1.56%	1.26%	1.53%	1.26%	1.45%	1.30%	1.63%	1.50%

Table 7.8. Summary of correction factor deviations for double elbow case. (Part 2)

x/D	0°	30°	45°	60°	90°	120°	135°	150°	180°
					$Re = 2 \times 10^5$				
1	4.51%	7.10%	3.92%	3.33%	4.23%	7.06%	8.87%	10.26%	10.82%
5	5.34%	5.71%	6.29%	7.50%	6.67%	6.46%	6.45%	6.44%	6.45%
10	13.42%	8.25%	6.66%	6.04%	5.07%	5.02%	5.25%	6.88%	5.56%
15	4.17%	6.11%	7.87%	10.87%	8.84%	5.42%	4.20%	3.70%	2.91%
20	2.65%	2.48%	2.13%	2.58%	3.92%	7.99%	9.27%	8.62%	4.65%
40	4.65%	2.26%	0.73%	0.21%	-0.18%	1.20%	1.93%	3.11%	2.79%
60	0.71%	0.40%	-0.02%	0.50%	1.59%	2.69%	2.31%	2.21%	1.11%
80	1.03%	1.43%	1.03%	1.31%	1.11%	0.98%	0.54%	0.79%	1.11%
					$Re = 1 \times 10^6$				
1	5.83%	6.66%	4.02%	3.91%	4.65%	7.94%	8.84%	8.36%	7.40%
5	1.44%	3.43%	4.32%	4.96%	5.46%	5.28%	4.52%	4.11%	4.78%
10	4.90%	2.88%	1.90%	1.75%	2.45%	4.92%	4.48%	3.60%	3.94%
15	5.43%	9.82%	7.87%	5.82%	3.46%	2.27%	1.66%	1.75%	3.37%
20	1.83%	2.08%	2.21%	3.67%	8.29%	6.38%	4.29%	3.23%	1.70%
40	1.78%	-0.11%	-1.08%	-1.01%	0.30%	3.17%	3.19%	2.57%	0.66%
60	-0.79%	-0.89%	-1.01%	-0.09%	1.95%	2.92%	1.94%	1.17%	-0.52%
80	-0.23%	0.71%	0.46%	0.66%	0.02%	-0.49%	-0.98%	-0.75%	-0.07%
					$Re = 2 \times 10^6$				
1	5.48%	5.41%	3.37%	3.45%	4.32%	7.77%	8.56%	8.11%	7.49%
5	1.47%	3.44%	4.26%	4.21%	5.69%	4.97%	4.24%	3.96%	4.97%
10	4.03%	2.12%	1.27%	1.34%	2.55%	4.76%	3.39%	3.52%	4.01%
15	7.08%	8.27%	5.73%	4.49%	2.68%	1.75%	1.34%	1.74%	4.35%
20	1.86%	2.47%	3.14%	5.50%	8.06%	4.48%	3.04%	2.34%	1.16%
40	0.40%	-0.74%	-1.30%	-0.69%	1.78%	3.29%	2.17%	1.30%	-0.03%
60	-1.07%	-0.62%	-0.37%	0.88%	2.84%	2.32%	0.98%	0.19%	-1.07%
80	0.08%	0.97%	0.52%	0.48%	-0.35%	-0.71%	-1.05%	-0.65%	0.34%

Chapter 8

Final Remarks

The main objective of this dissertation may be summarized as representing the turbulent disturbed flow downstream from pipe elbow installations by means of CFD in order to evaluate the effects of such disturbances on the correction factor of single-path ultrasonic flow meters. Such goal has been met and the analysis of results may lead to further discussion. In the following section, main results are reviewed and commented, the main difficulties faced in performing the present work are exposed and some proposals for future work are suggested.

8.1 Remarkable Results

A commercial CFD code has been used to calculate the flow field downstream from two typical pipe installations: single elbow and double elbow out-of-plane. Numerical integration has allowed the calculation of numerical correction factors for simulating ultrasonic flow meters.

The main contribution of this dissertation is to bring together installation effects considering several Reynolds number, axial positions and transducers mounting angle. The results for each case have been compared with fully developed references.

The main conclusion may be verified by returning to the motivation: flare gas installations. Item 7.1.10 in Portaria Conjunta ANP/INMETRO No. 1 [16] indicates that flow measurement systems for gas custody transfer must provide uncertainties lower than 1.5%. Other gas mea-

surement systems (not custody) must be under 3% and flare gas installations are usually in this second case. Assuming that 2% of these 3% is only due to installation effects, and regarding the values in Tabs. 7.5 to 7.8, present results indicate that such values can be mostly achieved 40D or more downstream from the curve. Furthermore, the magnitude of deviations at axial positions up to 20D are mostly considerably higher than 3%. By making such analysis, the relevance of the present study is highlighted and the necessity of further research is reinforced.

Among all tests and results, some of them are worth to be mentioned.

- *CFD codes* – Two CFD codes have been used: CFX and FLUENT. In fact, present the best code is out of scope of the present work. They have been considered both useful tools for estimating the behaviour of ultrasonic flow measurements under disturbed condition. However, during the validation study, FLUENT default turbulence inlet condition has provided better agreement with experiments and CFX solution has diverged under the same conditions.

- *Turbulence models* – Two turbulence models have been considered: k–ε and k–ε RNG. Overall results for them have presented similar behaviour as commented in Chapter 6. It is remarkable that a test carried out with k–ε in a straight pipe has resulted in opposite behaviour for the correction factor for lower Reynolds numbers, as commented in Chapter 7.

- *Nikuradse-based correction factor* – Despite the necessity of further investigation on numerical methods, correction factors calculated from simulated flow field for straight pipe have provided significant magnitude of deviations of up to 2.52% when compared to the correction factor obtained using Nikuradse [34] profile. Such result indicates at least the necessity of reviewing the suggestion of AGA 9 [31] as well as of ABNT [17] to use Nikuradse profile for calculating the correction factor. Of course, deviations are even higher in the presence of curves, reaching deviations of up to approximately 30%. It is believed that more modern approach can be carried out with respect to defining a fully developed flow profile, which plays an important role on factor k calculation.

  It is also important to remark that apparently there is a misunderstanding with respect to the mathematical formalism in the derivation of the factor k in AGA 9 [31]. It is believed that in both editions of AGA 9 [15, 31] as well as in the Brazilian regulation [17] the same

symbol is used to refer to both $\bar{V}_{AP}$ and $\bar{V}_{UFM}$, leading to some confusion. Since such mistake has been repeated over time, the revision of such issue is left as a suggestion.

- *Pipe configuration (single and double elbow)* – Single elbow results present smoother behaviour than double elbow, with curves approximately parallel to each other, tending to fully developed flow reference as the axial distance increases. Moreover, single elbow deviations are generally higher than double elbow deviations right after the curve ($\approx 1D$), but the decay is relatively faster. Such behaviour is also observed by Sanderson and Young [13]. The results for 80D (even 60D for low Reynolds) in Tabs. 7.5 and 7.6 show that fully developed flow condition is almost recovered (less than 0.5% deviation), except for intermediary Re, for which deviations are from 1.03% to 1.75%. Also, profile symmetry may be already observed by approximately symmetric deviations for supplementary angles.

  On the other hand, double elbow results are much more complex. Also, swirl effects make ultrasonic flow meter more sensitive to mounting angle and axial position. When these two characteristics are put together, the result is correction factor curves with derivative sign changes crossing each other, which may increase computational effort for calculating the flow rate, as commented in Chapters 2 and 7. It is remarkable that, unlike single elbow case, symmetry proximity is only observed for low Reynolds, indicating that the flow is not close to fully developed as in single elbow case.

- *Reynolds number* – It is known that flow inertia is higher for greater Re. In such conditions, disturbances take longer distances to vanish, allowing higher deviations to reach longer distances, specially after 20D. Such behaviour may be observed for both single and double elbow configuration (Figs. 7.4 and 7.6).

- *Axial position* – The results of the present work suggest that ultrasonic flow meters are not only sensitive to the mounting angle, but to the distance from the obstacle they are installed as well. Axial position apparently plays an important role on the magnitude of installation effects. Commentaries for its influence are strongly dependent on the upstream obstacle and on the mounting angle. Generally speaking, axial positions shorter than 8D might not be desired for single elbow configurations, since results indicate higher deviations at such conditions. For measurements after 10D, results suggest that the farther the meter is placed the better. Regarding double bend case, flow field complexity reflects on

ultrasonic flow measurements. It is remarkable that deviations around 20D present strong sensitivity to the mounting angle. Using manufacturer's and regulations' recommendation of installing ultrasonic flow meters up to 20D downstream from obstacles apparently requires special attention, since the calculations carried out in this dissertation present deviations mostly high, reaching approximately 30% in some cases. Such results suggest at least the necessity of revision of such recommended conditions.

- *Transducers mounting angle* – As already observed in the literature [4, 12, 21, 29, 51, 63], mounting angle plays an important role since results are reasonably sensitive to it. Results of this dissertation indicate that deviations can vary more than 30% just by changing the mounting angle. In a general form, the present results suggest that mounting angle of 90° provide lower deviations for single elbow installation, while 180° show significantly worse predictions. Double elbow results, on the other hand, do not allow mentioning any favourable angle. Nevertheless, it is important to reinforce that it is possible to obtain relatively lower deviations in shorter distances just by combining favourable angle and Reynolds number. Testing such behaviour in practical situation is necessary and if similar performance is confirmed, variation of mounting angle could be applied for improving accuracy of bad-located ultrasonic flow meters. However, they are specific conditions and, statistically speaking, lower deviations are only possible after approximately 60D or more.

8.2   Main Difficulties

>"One of the beautiful things about science is that it allows us to bumble along, getting it wrong time after time, and feel perfectly fine as long as we learn something each time."
>Martin A. Schwartz [96]

During the production of the dissertation some difficulties have been faced and they are now exposed aiming an attempt to avoid repeating such facts in future works.

- *Pioneering work.* – Flow Measurement Team of Ufes, headed by Prof. Rogério Ramos, is recent and being the pioneer in numerical simulations applied to installation effects

have not been a simple job. CFD works require experience, sensibility and sensitivity. Otherwise results do not make much sense. In fact, it took some time to understand such issues, face some new questions and start to answer them. Nevertheless, limitations are now mostly known and they are part of the proposals for future work in the following section.

- *Absence of experimental facilities.* – Adequate experimental facilities could provide better-posed boundary conditions and data for validation procedure applied to disturbed flows, since they are not commonly found in the literature. Elbow installations are now available at *Laboratório de Máquinas de Fluxo* (LabMaqFlu) of Ufes and adequate instrumentation may provide input and output data for CFD modelling and validation. Besides the support for simulations, experiments could also provide better knowledge about disturbed flows and ultrasonic flow meters.

8.3 Proposals for Future Work

A literature review and the results presented in this dissertation provide some proposals to further investigation.

- *Detailed investigation on the influence of modelling parameters.* – Several chapters in this dissertation show the possibility of influence quantities. Although they have been preliminarily tested, it is suggested further investigation on those parameters. One may highlight the influence of:

  - *advection schemes*, for which the preliminary test has suggested significant sensitivity (see Fig. 5.10);

  - *turbulence models*, since it is known that there are more appropriate turbulence models to capture swirl effects as well as merely more robust models. Recent work [97] shows that k–ε RNG model provide good agreement with experimental velocity profile for low-swirl flows, whereas Reynolds Stress Model (RSM) become more appropriate as swirl increases. Moreover, both models show unrealistic decay of turbulence quantities. Nevertheless, RSM model is suggested as a first approach

for future work and, since LES might lead to more realistic results, it should be considered for further investigation as well;

– *boundary conditions*, specially turbulent boundary conditions.;

– *fluid models*, because flare gas is a natural gas whose composition is not the same of air. Ideal gas modelling may be considered as a first attempt, as indicated by Salgado and Ramos [94].

- *Account of wave equations for calculation of acoustic path deviation.* – Gathering acoustics and fluid dynamic equations, it is possible to find the acoustic path and its deviations due to different flow profiles [29, 30]. In this sense, it seems reasonable to apply the simulation of ultrasonic flow meters (as considered in the present work) for calculated acoustic path, instead of assuming linear chords.

- *Investigation on the influence of transient analysis on the correction factor.* – It is know that turbulence fluctuations may cause deviations on ultrasonic flow rate measurements [33], despite the very small time scales associated to them. Hence, numerical simulations taking into account transient processes are also proposed for further investigation.

- *Support of experimental facilities.* – CFD modelling supplied by experimental data usually provides more accurate results. The possibility of measuring inlet and outlet quantities, and using measured data to validate the numerical model is always desired.

- *Dynamic correction factor.* – The results of the present work verify the sensitivity of ultrasonic flow meters to upstream installation. The proposal of a dynamic correction factor consists in developing an ultrasonic flow meter with self-adjustment aiming lower deviations due to installation effects. That might be possible with the aid of high-reliability CFD (well-posed boundary conditions, well modelled and precisely verified) in order to provide correction factor under several conditions (as calculated in the present work). Such correction factors functions would be programmed in the meter's computer and installation arrangement would provide the best function. Moreover, a modified ultrasonic flow meter capable to rotate over the pipe axis in order to find the best mounting angle might be considered. Moreover, angular corrections for acoustic path deviation could also be considered as a function of Reynolds number.

References

[1] P. I. Moore, G. J. Brown, and B. P. Stimpson, "Ultrasonic transit-time flowmeters modelled with theoretical velocity profiles: methodology," *Measurement Science and Technology*, vol. 11, no. 12, p. 1802, 2000.

[2] P. Lunde, K.-E. Frøysa, and M. Verstrheim, "Multipath ultrasonic transit time gas flow meters," in *GERG Project on Ultrasonic Gas Flow Meters, Phase II* (P. Lunde, K.-E. Frøysa, and M. Verstrheim, eds.), ch. 3, pp. 13 – 30, Groupe Européen de Recherches Gazières, 2000.

[3] H. Versteeg and W. Malalasekera, *An Introduction to Computational Fluid Dynamics - The Finite Volume Method*. Essex, England: Pearson Education Limited, 2nd ed., 2007.

[4] A. Hilgenstock and R. Ernst, "Analysis of installation effects by means of computational fluid dynamics – CFD vs experiments?," *Flow Measurement and Instrumentation*, vol. 7, no. 3-4, pp. 161 – 171, 1996.

[5] K. Mylvaganam, "High-Rangeability Ultrasonic Gas Flowmeter for Monitoring Flare Gas," *IEEE Transactions on Ultrasonics Ferroelectric and Frequecy Control*, vol. 36, no. 2, pp. 144 – 149, 1989.

[6] GAO, "GAO-04-809 – NATURAL GAS FLARING AND VENTING – Opportunities to Improve Data and Reduce Emissions," tech. rep., United States Government Accountability Office, July 2004.

[7] Clearstone Engineering Ltd., "Guidelines on Flare and Vent Measurement," Tech. Rep., Clearstone Engineering Ltd., Alberta, Canada, September 2008.

[8] ERCB, "ERCB Directive 060: Upstream Petroleum Industry Flaring, Incinerating, and Venting." ERCB - Energy Resources Conservation Board, Alberta, Canada, November 2011.

[9] L. Sui, T. H. Nguyen, J. E. Matson, P. Espina, and I. Tew, "Ultrasonic Flowmeter for Accurately Measuring Flare Gas over a Wide Velocity Range," in *Proceedings of the 15th Flow Measurement Conference (FLOMEKO)*, (Taipei, Taiwan), October 13-15 2010.

[10] G. Buonanno, "On field characterisation of static domestic gas flowmeters," *Measurement*, vol. 27, no. 4, pp. 277 – 285, 2000.

[11] J. C. Jung and P. H. Seong, "Estimation of the Flow Profile Correction Factor of a Transit–Time Ultrasonic Flow Meter for the Feedwater Flow Measurement in a Nuclear Power Plant," *IEEE Transactions on Nuclear Science*, vol. 52, no. 3, pp. 714 – 718, 2005.

[12] H. Hu, C. Wang, and T. Meng, "Numerical approach to estimate the accuracy of ultrasonic flowmeter under disturbed flow condition," in *Proceedings of the 15th Flow Measurement Conference (FLOMEKO)*, (Taipei, Taiwan), October 13-15 2010.

[13] M. Sanderson and H. Yeung, "Guidelines for the use of ultrasonic non–invasive metering techniques," *Flow Measurement and Instrumentation*, vol. 13, pp. 125 – 142, 2002.

[14] L. Lynnworth and Y. Liu, "Ultrasonic flowmeters: Half-century progress report, 1955-2005," *Ultrasonics*, vol. 44, no. Supplement 1, pp. e1371 – e1378, 2006. Proceedings of Ultrasonics International (UI'05) and World Congress on Ultrasonics (WCU).

[15] AGA, "Measurement of Gas by Multipath Ultrasonic Meters," Report No. 9, American Gas Association, Arlington, Virginia, 1998.

[16] ANP/INMETRO, "Portaria Conjunta ANP/INMETRO N° 1." 20.06.2011 - DOU - Diário Oficial da União, 2000.

[17] ABNT, "ABNT NBR 15855:2010 - Medição de gás por medidores do tipo ultra-sônicos multitrajetórias," Norma Brasileira, Associação Brasileira de Normas Técnicas, Rio de Janeiro, Brazil, July 2010.

[18] G. J. Delmée, *Manual de Medição de Vazão*. São Paulo, Brazil: Edgard Blücher Ltda,

3rd ed., 2003.

[19] J. Berrebi, *Self-Diagnosis Techniques and Their Applications to Error Reduction for Ultrasonic Flow Measurement*. PhD thesis, Luleå University of Technology, 2004.

[20] R. W. Miller, *Flow Measurement Engineering Handbook*. McGraw–Hill, 3rd ed., 1996.

[21] D. Zheng, T. Zhang, L. Sun, T. Meng, H. Hu, and C. Wang, "Installation Effects of Ultrasonic Flowmeter in Single Bend Pipe," in *Proceedings of the 15th Flow Measurement Conference (FLOMEKO)*, (Taipei, Taiwan), October 13-15 2010.

[22] Honeywell International, Inc., "NATURAL GAS ULTRASONIC FLOW METER USZ-08," 2012. Accessed on March 30th, 2012. Available on http://www.mercuryinstruments. com/products_flowmeter_USM_USZ-08.php.

[23] General Electric Company, "DigitalFlow™ GC868 Medidor de vazão ultrassônico não-intrusivo de gás da Panametrics," 2012. Accessed on March 30th, 2012. Available on <http://www.ge-mcs.com/download/co2-flow/920_012b_PO.pdf>.

[24] Sick - Sensor Intelligence, "FLOWSIC100 Flare Ultrasonic Mass Flow Meter - Gas Mass Flow Measurement for Flare Gas Applications," 2012. Accessed on March 30th, 2012. Available on <http://www.baytec-inc.com/pdf/sick-maihak-flare-gas-monitoring.pdf>.

[25] Fluenta, "FGM-160 FLOWMETER," 2012. Accessed on March 30th, 2012. Available on <http://www.fluenta.com/bilder/filer/Fluenta_Datasheet_FGM160_february012.pdf>.

[26] R. Raišutis, "Investigation of the flow velocity profile in a metering section of an invasive ultrasonic flowmeter," *Flow Measurement and Instrumentation*, vol. 17, pp. 201 – 206, 2006.

[27] C. Carlander and J. Delsing, "Installation effects on an ultrasonic flow meter with implications for self diagnostics," *Flow Measurement and Instrumentation*, vol. 11, no. 2, pp. 109 – 122, 2000.

[28] R. Ramos, "Desenvolvimento de um medidor de vazão de gás por ultra-som: modelagem, protótipo e testes," MSc Dissertation, Programa de Pós-Graduação em Engenharia Mecânica, Universidade Federal do Espírito Santo, Vitória, 2006.

[29] T. Yeh and G. Mattingly, "Computer simulations of ultrasonic flow meter performance in ideal and non-ideal pipeflows," in *ASME Fluids Engineering Division Summer Meeting - FEDSM'97*, ASME, 1997.

[30] R. B. Mathias, "Influência do perfil de velocidade do escoamento sobre a medição ultra-sônica de vazão por tempo de trânsito," MSc Dissertation, Programa de Pós-Graduação em Engenharia Mecânica, Universidade Federal do Espírito Santo, Vitória, 2010.

[31] AGA, "Measurement of Gas by Multipath Ultrasonic Meters," Report No. 9, American Gas Association, Washington, DC, USA, 2nd ed., April, 2007.

[32] H. Köchner, A. Melling, and M. Baumgärtner, "Optical flow field investigations for design improvements of an ultrasonic gas meter," *Flow Measurement and Instrumentation*, vol. 7, no. 3-4, pp. 133 – 140, 1996.

[33] B. Iooss, C. Lhuillier, and H. Jeanneau, "Numerical simulation of transit–time ultrasonic flowmeters: uncertainties due to flow profile and fluid turbulence," *Ultrasonics*, vol. 40, pp. 1009 – 1015, 2002.

[34] J. Nikuradse, "Laws of Turbulent Flow in Smooth Pipes," NASA TT F-10, 359, National Aeronautics and Space Administration, Washington, USA, 1966. Translated from 'Gesetzmässigkeiten der turbulenten Strömung in glatten Rohern' Forsch. Arb. Ing.-Wes. No. 356 (1932).

[35] H. Schlichting, *Boundary-Layer Theory*. McGraw-Hill series in Mechanical Engineering, New York, USA: McGraw-Hill, 6th ed., 1968.

[36] S. Gol'tsov, "Refined mathematical model of an ultrasonic flowmeter," *Measurement Techniques*, vol. 41, no. 6, pp. 529 – 532, 1998. Translated from 'Izmeritel'naya Tekhnika', No. 6, pp. 25-27, June, 1998.

[37] T. Cousins and B. Griffith, "THE PRODUCTION OF SWIRL IN OILAND METHOD OF COMPENSATION IN MULTI-PATH ULTRASONIC FLOWMETERS," in *Proceedings of the 15th Flow Measurement Conference (FLOMEKO)*, (Taipei, Taiwan), October 13-15 2010.

[38] J. G. Drenthen, M. Kurth, J. van Klooster, and M. Vermeulen, "Reducing installation

effects on ultrasonic flow meters," in *Proceedings of the* 27th *North Sea Flow Measurement Conference*, (Tonsberg), 2009.

[39] A. Hilgenstock, T. Hüwener, and B. Nath, "Kalibra® – A Fast Numerical Method for Determining Installations Effects in Ultrasonic Flowmeters," in *Proceedings of the* 8th *Flow Measurement Conference (FLOMEKO)*, (Lund, Sweden), June 15-17 1998.

[40] A. Hilgenstock, T. Hüwener, and B. Nath, "Prediction of measurement errors of ultrasonic flowmeters in disturbed flow conditions," in *GERG Project on Ultrasonic Gas Flow Meters, Phase II* (P. Lunde, K.-E. Frøysa, and M. Verstrheim, eds.), ch. 4, pp. 31 – 40, Groupe Européen de Recherches Gazières, 2000.

[41] E. Mandard, D. Kouamé, R. Battault, J.-P. Remenieras, and F. Patat, "Methodology for Developing a High-Precision Ultrasound Flow Meter and Fluid Velocity Profile Reconstruction," *IEEE Transactions on Ultrasonics, Ferroelectrics, and Frequency Control*, vol. 55, no. 1, pp. 161 – 172, 2008.

[42] V. Herrmann, M. Wehmeier, T. Dietz, A. Ehrlich, and M. Dietzen, "THE PRODUCTION OF SWIRL IN OILAND METHOD OF COMPENSATION IN MULTI-PATH ULTRA-SONIC FLOWMETERS," in *Proceedings of the* 5th *International South East Asia Hydrocarbon Flow Measurement Workshop*, March 8-10 2006.

[43] H. Obayashi, Y. Tasaka, S. Kon, and Y. Takeda, "Velocity vector profile measurement using multiple ultrasonic transducers," *Flow Measurement and Instrumentation*, vol. 19, no. 3-4, pp. 189 – 195, 2008.

[44] E. Håkansson and J. Delsing, "Effects of pulsating flow on an ultrasonic gas flowmeter," *Flow Measurement and Instrumentation*, vol. 5, no. 2, pp. 93 – 101, 1994.

[45] J. Berrebi, P.-E. Martinsson, M. Willatzen, and J. Delsing, "Ultrasonic flow metering errors due to pulsating flow," *Flow Measurement and Instrumentation*, vol. 15, no. 3, pp. 179 – 185, 2004.

[46] J. Berrebi, J. van Deventer, and J. Delsing, "Reducing the flow measurement error caused by pulsations in flows," *Flow Measurement and Instrumentation*, vol. 15, no. 5-6, pp. 311 – 315, 2004.

[47] J. Battye, "Acoustic considerations effecting the design of demodulators for the ultrasonic correlation flow meter," *Sensors and Actuators A*, vol. 88, pp. 29 – 40, 2001.

[48] N. Roosnek, "Novel digital signal processing techniques for ultrasonic gas flow measurements," *Flow Measurement and Instrumentation*, vol. 11, pp. 89 – 99, 2000.

[49] N. Roosnek, "Corrigendum to "Novel digital signal processing techniques for ultrasonic gas flow measurements" [Flow Measurement and Instrumentation 11 (2000) 89-99]," *Flow Measurement and Instrumentation*, vol. 12, p. 231, 2001.

[50] M. Dell'Isola, M. Cannizzo, and M. Diritti, "Measurement of high-pressure natural gas flow using ultrasonic flowmeters," *Measurement*, vol. 20, no. 2, pp. 75 – 89, 1997.

[51] T. Yeh, P. Espina, and S. Osella, "An Intelligent Ultrasonic Flow Meter for Improved Flow Measurement and Flow Calibration Facility," in *Instrumentation and Measurement Technology Conference, 2001. IMTC 2001. Proceedings of the 18th IEEE*, vol. 3, pp. 1741 – 1746, 2001.

[52] J. Hill, A. Weber, and J. Weber, "Quality of Ultrasonic Flow Meters for Custody Transfer of Natural Gas Using Atmospheric Air Calibration Facilities," in *Proceedings of the North Sea Flow Measurement Workshop*, October 22-25 2002.

[53] A. Calogirou, J. Boekhoven, and R. Henkes, "Effect of wall roughness changes on ultrasonic gas flowmeters," *Flow Measurement and Instrumentation*, vol. 12, pp. 219 – 229, 2001.

[54] J. G. Drenthen and G. de Boer, "The manufacturing of ultrasonic gas flow meters," *Flow Measurement and Instrumentation*, vol. 12, no. 2, pp. 89 – 99, 2001.

[55] D. Zheng, P. Zhang, and T. Xu, "Study of acoustic transducer protrusion and recess effects on ultrasonic flowmeter measurement by numerical simulation," *Flow Measurement and Instrumentation*, vol. 22, no. 5, pp. 488 – 493, 2011.

[56] Y. Inoue, H. Kikura, H. Murakawa, M. Aritomi, and M. Mori, "A study of ultrasonic propagation for ultrasonic flow rate measurement," *Flow Measurement and Instrumentation*, vol. 19, no. 3-4, pp. 223 – 232, 2008.

[57] I. Fyrippi, I. Owen, and M. Escudier, "Flowmetering of non-newtonian liquids," *Flow Measurement and Instrumentation*, vol. 15, no. 3, pp. 131 – 138, 2004.

[58] R. Kotzé, J. Wiklund, R. Haldenwang, and V. Fester, "Measurement and analysis of flow behaviour in complex geometries using the Ultrasonic Velocity Profiling (UVP) technique," *Flow Measurement and Instrumentation*, vol. 22, no. 2, pp. 110 – 119, 2011.

[59] M. Holm, J. Stang, and J. Delsing, "Simulation of flow meter calibration factors for various installation effects," *Measurement*, vol. 15, no. 4, pp. 235 – 244, 1995.

[60] G. Wendt, B. Mickan, R. Kramer, and D. Dopheide, "Systematic investigation of pipe flows and installation effects using laser Doppler anemometry–Part I. Profile measurements downstream of several pipe configurations and flow conditioners," *Flow Measurement and Instrumentation*, vol. 7, no. 3-4, pp. 141 – 149, 1996.

[61] B. Mickan, G. Wendt, R. Kramer, and D. Dopheide, "Systematic investigation of pipe flows and installation effects using laser Doppler anemometry – Part II. The effect of disturbed flow profiles on turbine gas meters - a describing empirical model," *Flow Measurement and Instrumentation*, vol. 7, no. 3-4, pp. 151 – 160, 1996.

[62] B. Mickan, G. Wendt, R. Kramer, and D. Dopheide, "Systematic investigation of flow profiles in pipes and their effects on gas meter behaviour," *Measurement*, vol. 22, no. 1-2, pp. 1 – 14, 1997.

[63] C. Ruppel and F. Peters, "Effects of upstream installations on the reading of an ultrasonic flowmeter," *Flow Measurement and Instrumentation*, vol. 15, no. 3, pp. 167 – 177, 2004.

[64] F. Kreith and O. K. Sonju, "The decay of a turbulent swirl in a pipe," *Journal of Fluid Mechanics*, vol. 22, no. 02, pp. 257 – 271, 1965.

[65] W. R. Dean, "Fluid Motion in a Curved Channel," *Proc. R. Soc. Lond. A*, vol. 121, pp. 402 – 420, 1928.

[66] W. R. Dean and J. M. Hurst, "NOTE ON THE MOTION OF FLUID IN A CURVED PIPE," *Mathematika*, vol. 6, pp. 77 – 85, 1959.

[67] G. E. Mattingly and T. T. Yeh, "NBS' Industry-Government Consortium Research Pro-

gram on Flowmeter Installation Effects: Summary Report with Emphasis on Research Period July–December 1987," U.S. Departament of Commerce, National Institute of Standards and Technology - NIST, 1988.

[68] Th. Schlüter and W. Merzkirch, "PIV measurements of the time-averaged flow velocity downstream of flow conditioners in a pipeline," *Flow Measurement and Instrumentation*, vol. 7, no. 3-4, pp. 173 – 179, 1996.

[69] W. Xiong and K. Kalk "Velocity and turbulence measurements downstream of flow conditioners," *Flow Measurement and Instrumentation*, vol. 14, no. 6, pp. 249 – 260, 2003.

[70] B. J. Geurts, *Elements of direct and large-eddy simulation*. Edwards, 2004.

[71] P. Sagaut, *Large Eddy Simulation for Incompressible Flows: An Introduction*. Springer, 2006.

[72] O. Reynolds, "ON THE DYNAMICAL THEORY OF INCOMPRESSIBLE VISCOUS FLUIDS AND THE DETERMINATION OF THE CRITERION - [From the "Philosophical Transactions of the Royal Society", 1895]," in *PAPERS ON MECHANICAL AND PHYSICAL SUBJECTS - VOLUME II: 1881 - 1900*, ch. 62, Cambridge, UK: Cambridge University Press, 1901.

[73] S. B. Pope, *Turbulent Flows*. Cambridge, UK: Cambridge University Press, 2000.

[74] H. Tennekes and J. L. Lumley, *A First Course in Turbulence*. Cambridge, Massachusetts, USA: The MIT Press, 1972.

[75] Ansys, Inc., "ANSYS CFX™ Version 13.0," 2010.

[76] Ansys, Inc., "ANSYS FLUENT™ Version 13.0," 2010.

[77] J. Boussinesq, "Essai sur la théorie des eaux courantes," *Mémoires présentés par divers savants à l'Académie des Sciences de l'Institut de France XXIII*, vol. 1, pp. 1 – 680, 1877.

[78] Ansys, Inc., "ANSYS CFX-Solver Theory Guide," Canonsburg, PA, USA, 2010.

[79] Ansys, Inc., "ANSYS FLUENT Theory Guide," Canonsburg, PA, USA, 2010.

[80] B. Launder and D. Spalding, "The numerical computation of turbulent flows," *Computer Methods in Applied Mechanics and Engineering*, vol. 3, no. 2, pp. 269 – 289, 1974.

[81] W. Jones and B. Launder, "The prediciton of laminarization with a two-equation model of turbulence," *Int. J. Heat Mass Transfer*, vol. 15, pp. 301 – 314, 1972.

[82] W. Jones and B. Launder, "The calculation of low-Reynolds-number phenomena with a two-equation model of turbulence," *Int. J. Heat Mass Transfer*, vol. 16, pp. 1119 – 1130, 1973.

[83] V. Yakhot and S. A. Orszag, "Renormalization-group analysis of turbulence," *Phys. Rev. Lett.*, vol. 57, pp. 1722–1724, 1986.

[84] V. Yakhot, S. A. Orszag, S. Thangam, T. B. Gatski, and C. G. Speziale, "Development of turbulence models for shear flows by a double expansion technique," *Phys. Fluids A*, vol. 4, pp. 1510–1520, 1992.

[85] E. W. Swokowski, *Cálculo com Gemotetria Analítica*. São Paulo: McGraw-Hill do Brasil, 1983.

[86] C. R. Maliska, *Transferência de Calor e Mecânica dos Fluidos Computacional*. Rio de Janeiro, Brazil: LTC, 2nd ed., 2004.

[87] Ansys, Inc., "ANSYS FLUENT User's Guide," Canonsburg, PA, USA, 2010.

[88] S. Patankar and D. Spalding, "A calculation procedure for heat, mass and momentum transfer in three-dimensional parabolic flows," *International Journal of Heat and Mass Transfer*, vol. 15, no. 10, pp. 1787 – 1806, 1972.

[89] S. V. Patankar, *Numerical Heat Transfer and Fluid Flow*. Series in computational methods in mechanics and thermal sciences, USA: Taylor & Francis, 1980.

[90] F. C. Filho, *Algoritmos Numéricos*. LTC, 2nd ed., 2007.

[91] Ansys, Inc., "ANSYS CFX-Solver Modeling Guide," Canonsburg, PA, USA, 2010.

[92] A. L. A. S. Ferreira, *Tecnologia ultrassônica na medição de vazão em escoamentos incompressíveis*. PhD thesis, Pontifícia Universidade Católica do Rio de Janeiro, 2010.

[93] Ansys, Inc., "ANSYS ICEM CFD Version 13.0," 2010.

[94] A. L. Salgado and R. Ramos, "Validação do Modelo de Gás Perfeito para Avaliação das Propriedades Termofísicas do Gás de Flare Utilizando Dados Operacionais ," in *Anais do 5º CONGRESSO BRASILEIRO DE PESQUISA E DESENVOLVIMENTO EM PETRÓLEO E GÁS (PDPETRO)*, (Fortaleza, Brazil), October 15-22 2009.

[95] L. J. De Chant, "The venerable 1/7th power law turbulent velocity profile: a classical nonlinear boundary value problem solution and its relationship to stochastic processes," *Applied Mathematics and Computation*, vol. 161, no. 2, pp. 463 – 474, 2005.

[96] M. A. Schwartz, "The importance of stupidity in scientific research," *Journal of Cell Science*, vol. 121, p. 1771, 2008.

[97] A. Escue and J. Cui, "Comparison of turbulence models in simulating swirling pipe flows," *Applied Mathematical Modelling*, vol. 34, pp. 2840 – 2849, 2010.

Appendix A

Mesh Sensitivity Study Results

This appendix complements mesh sensitivity study exemplified in Chapter 5. It contains information about mesh parameters and figures used to evaluate validation, straight pipe and double elbow cases.

The same doubling nodes number procedure described in Chapter 5 has been considered for mesh generation and Tabs. A.1 to A.3 present mesh parameters for validation, straight pipe and double elbow cases, respectively.

Table A.1. Mesh parameters for validation case.

Mesh	Nodes	Maximum Size [mm]	Height [mm]
1	1.3×10^5	15	4
2	3.0×10^5	11	2.8
3	6.0×10^5	8.6	1.6
4	1.23×10^6	6.8	0.9
5	2.35×10^6	5.5	0.44
6	4.89×10^6	4.3	0.19

It is important to remark that the height of the first element in all chosen meshes (*i.e.* those considered to be in satisfactory agreement to the ones with double nodes number) is approximately 0.25% of diameter. The number of nodes varies with domain size and problem complexity, so that validation and straight pipe cases present less (approximately half) nodes when compared

Table A.2. Mesh parameters for straight pipe case.

Mesh	Nodes	Maximum Size [mm]	Height [mm]
1	3.0×10^5	28	9
2	6.2×10^5	22	5
3	1.24×10^6	18.7	2
4	2.54×10^6	15.7	0.8
5	5.24×10^6	12.3	0.3

Table A.3. Mesh parameters for double elbow case.

Mesh	Nodes	Maximum Size [mm]	Height [mm]
1	9×10^4	60	20
2	1.8×10^5	43	16
3	3.6×10^5	31	12
4	7.1×10^5	22.6	9
5	1.47×10^6	18	5
6	2.92×10^6	14.9	2
7	5.79×10^6	12.3	0.8
8	10.63×10^6	10	0.4

to single and double elbow cases.

Next, figures containing velocity profiles for all meshes at a non-fully developed section are presented, as in Chapter 5.

Figure A.1 depicts velocity profiles at the analysed plan (5D from the double elbow) for validation case. Axial velocity component ($\bar{u}$) obtained with meshes 5 and 6 seems to be in very good agreement (Fig. A.1a). Such agreement is also clearly observed for the $\bar{w}$-velocity component (Fig. A.1c). For $\bar{v}$-velocity (Fig. A.1b), agreement is not as good as for other velocity components, but is considered satisfactory as well, mainly because, in this case, such velocity component present magnitudes less than ten times smaller compared to $\bar{w}$-velocity. Generally speaking, mesh 5 and 6 seem to be in good agreement for the velocity profiles tested. Thus, mesh 5 has been used for all validation runs.
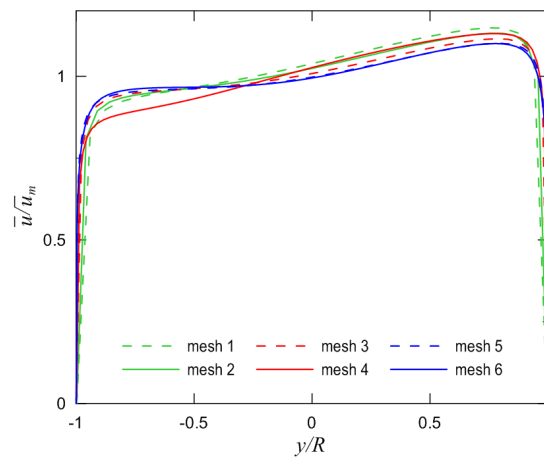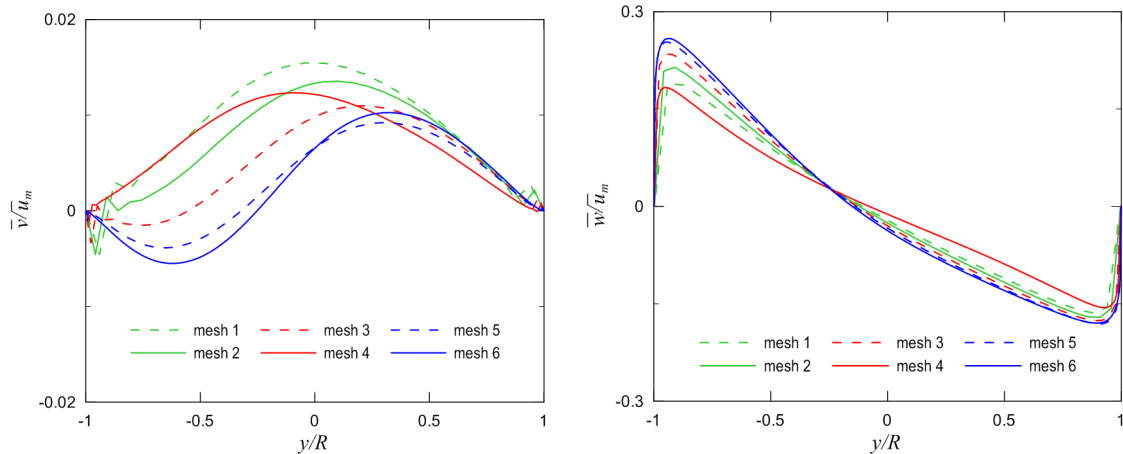
(a) Non-dimensional $\bar{u}$ velocity at $5D$ for $\theta = 0°$.

(b) Non-dimensional $\bar{v}$ velocity at $5D$ for $\theta = 0°$.

(c) Non-dimensional $\bar{w}$ velocity at $5D$ for $\theta = 0°$.

Figure A.1. Mesh test results for validation case.

Figure A.2 presents mesh test results for straight pipe case. In a general form, one may notice that results are less influenced by the mesh than in complex flow fields such as downstream of single and double elbow. The magnitude of velocities in Fig. A.2d are close to convergence criteria order and tend to zero. In Fig. A.2c, velocities are approximately a hundred times higher, and greater differences are evident only for meshes 1 and 2. Velocities along pipe center present very close results for all meshes (Fig. A.2a). Despite mesh 3 seems to be satisfactory, analysis of Fig. A.2b leads to some influence, particularly for near-wall velocities. Thus, mesh 4 has been considered for straight pipe simulations.

Figure A.3 displays mesh test results for double elbow case. Similarly to Fig. 5.8 in Chapter 5, Fig. A.3 presents an asymptotic behaviour and velocity profiles for the main component ($\bar{u}$) obtained with meshes 7 and 8 seem to be in good agreement (Fig. A.3b). Despite small differences
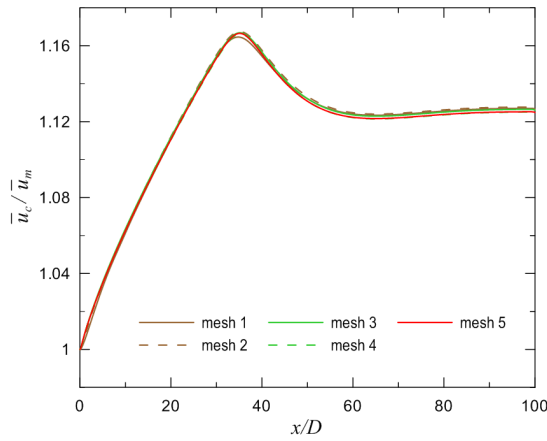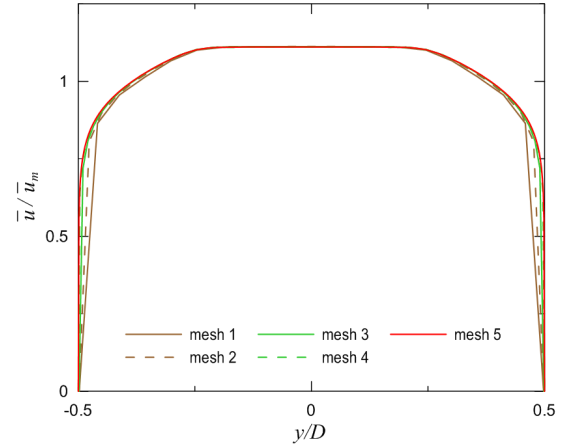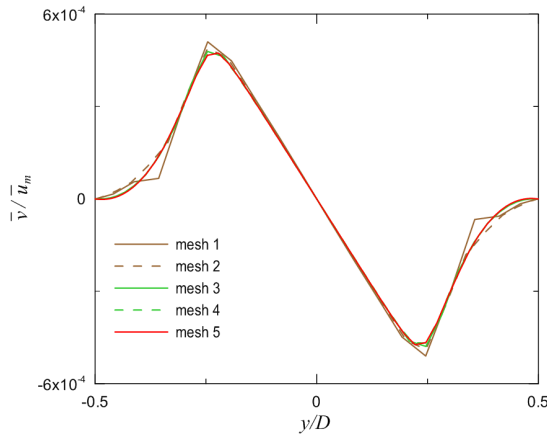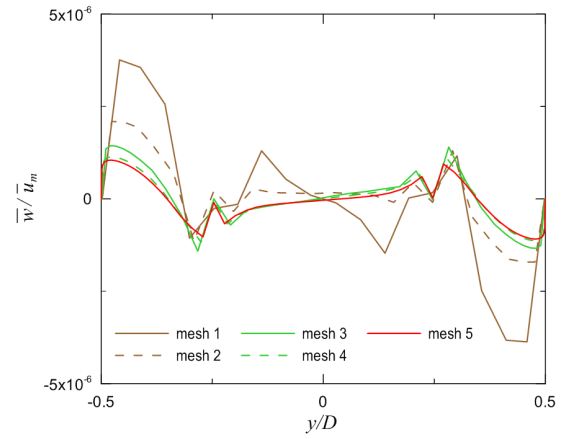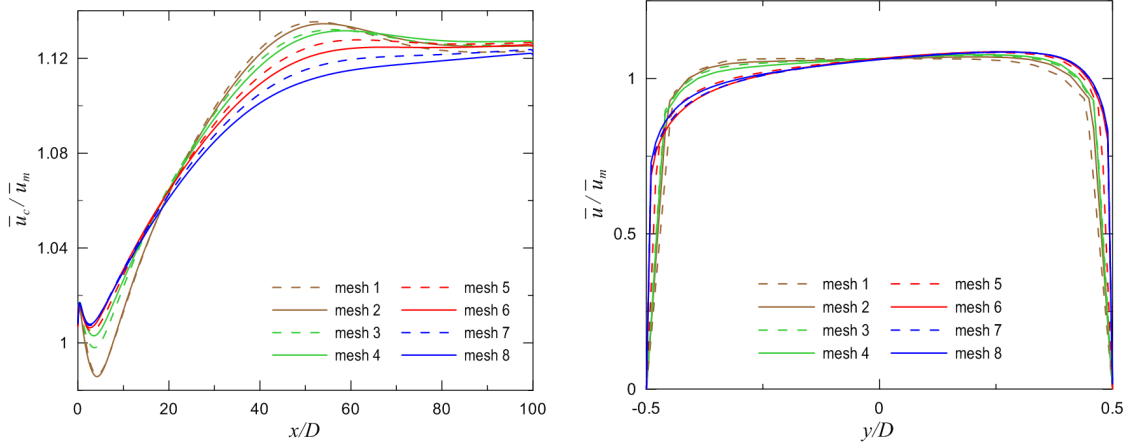
(a) Non-dimensional $\bar{u}$ velocity along pipe center

(b) Non-dimensional $\bar{u}$ velocity at $20D$ for $\theta = 0°$.

(c) Non-dimensional $\bar{v}$ velocity at $20D$ for $\theta = 0°$.

(d) Non-dimensional $\bar{w}$ velocity at $20D$ for $\theta = 0°$.

Figure A.2. Mesh test results for straight pipe.

in Figs. A.3a, A.3c and A.3d, overall results are also in good agreement comparing meshes 7 and 8. In fact, further tests would be recommended, however, testing a finer mesh have not shown to be possible due to computer's memory limitation. It is believed that such differences vanish as lower Reynolds are considered and thus mesh 7 has been considered for double elbow simulations.

(a) Non-dimensional $\bar{u}$ velocity along pipe center

(b) Non-dimensional $\bar{u}$ velocity at $20D$ for $\theta = 0°$.
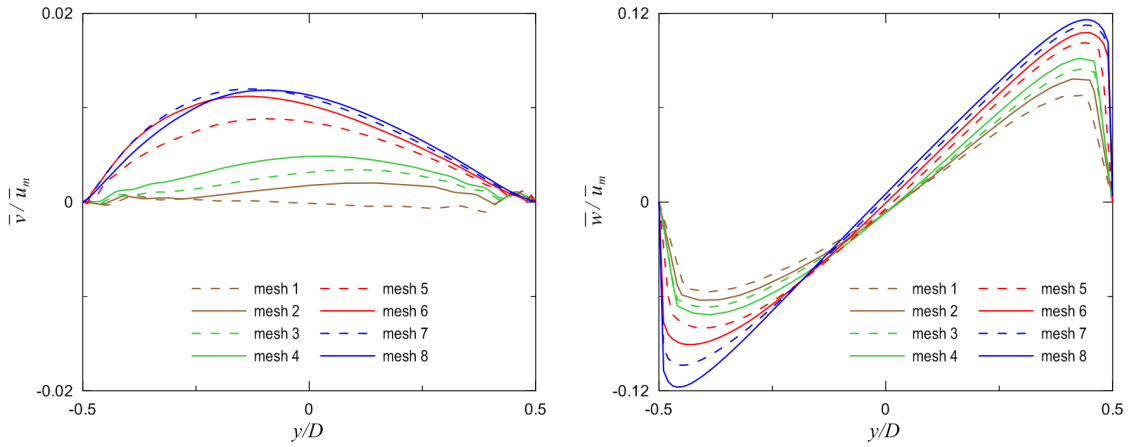
(c) Non-dimensional $\bar{v}$ velocity at $20D$ for $\theta = 0°$.

(d) Non-dimensional $\bar{w}$ velocity at $20D$ for $\theta = 0°$.

Figure A.3. Mesh test results for double elbow.